THE UNIVERSITY OF
WARWICK

University of Warwick institutional repository: http://go.warwick.ac.uk/wrap

A Thesis Submitted for the Degree of PhD at the University of Warwick

http://go.warwick.ac.uk/wrap/2228

This thesis is made available online and is protected by original copyright.

Please scroll down to view the document itself.

Please refer to the repository record for this item for information to help you to cite it. Our policy information is available from the repository home page.

THE UNIVERSITY OF
WARWICK

AUTHOR: **Paul Harvey Jefferson** DEGREE: **Ph.D.**

TITLE: **Optoelectronic properties of highly mismatched semiconductor materials**

DATE OF DEPOSIT: ....

I agree that this thesis shall be available in accordance with the regulations governing the University of Warwick theses.

I agree that the summary of this thesis may be submitted for publication.

I agree that the thesis may be photocopied (single copies for study purposes only).

Theses with no restriction on photocopying will also be made available to the British Library for microfilming. The British Library may supply copies to individuals or libraries. subject to a statement from them that the copy is supplied for non-publishing purposes. All copies supplied by the British Library will carry the following statement:

> "Attention is drawn to the fact that the copyright of this thesis rests with its author. This copy of the thesis has been supplied on the condition that anyone who consults it is understood to recognise that its copyright rests with its author and that no quotation from the thesis and no information derived from it may be published without the author's written consent."

AUTHOR'S SIGNATURE: ....

USER'S DECLARATION

1. I undertake not to quote or make use of any information from this thesis without making acknowledgement to the author.
2. I further undertake to allow no-one else to use this thesis while it is in my care.

DATE SIGNATURE ADDRESS

....

....

....

....

....

www.warwick.ac.uk

Optoelectronic properties of highly mismatched semiconductor materials

by

Paul Harvey Jefferson

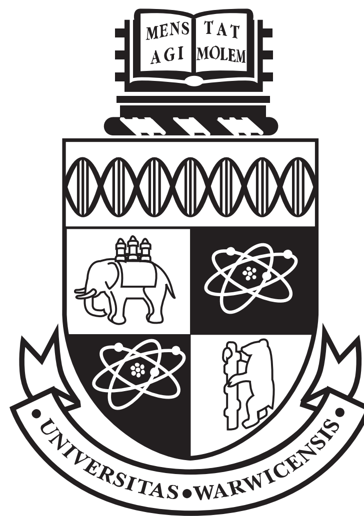

Thesis

Submitted to the University of Warwick

for the degree of

Doctor of Philosophy

Department of Physics

May 2009

THE UNIVERSITY OF
WARWICK

Contents

Acknowledgements **v**

Declarations **vi**

Abstract **x**

Abbreviations **xi**

Chapter 1 Introduction **1**

1.1 Historical background 1

1.1.1 Dilute nitrides of III–V materials 1

1.1.2 Transparent conducting oxides 2

1.2 Organisation of the thesis 2

1.3 Semiconductor crystal structure 3

1.4 Energy band structure 4

1.5 Bandstructure approximations 5

1.5.1 Parabolic approximation 5

1.5.2 8-band $\mathbf{k} \cdot \mathbf{p}$ (neglecting the effect of higher bands) 6

1.5.3 2-band $\mathbf{k} \cdot \mathbf{p}$: the α-approximation 7

1.5.4 Pidgeon and Brown 8-band $\mathbf{k} \cdot \mathbf{p}$ Hamiltonian 8

1.6 Dilute nitride bandstructure 9

1.6.1 Deviation from the virtual crystal approximation 11

1.6.2 The band anticrossing model 13

1.6.3 Tight-binding calculations 15

1.6.4 Empirical pseudopotential method 17

Chapter 2 Experimental techniques **18**

2.1 Optical absorption spectroscopy 18

2.2 Infrared reflectance spectroscopy 20

2.3 X-ray diffraction 22

2.4 Hall effect measurements 22

I Dilute nitrides of III–Sb materials **24**

Introduction 25

Chapter 3 GaNSb optical characterisation **30**

3.1 Introduction 31

3.2 Experimental details 31

3.3 Absorption simulation 32

3.4 Results and discussion 34

3.5 Conclusions 39

Chapter 4 InNSb optical characterisation **40**

4.1 Introduction 41

4.2 Experimental details 42

4.3 Theoretical background 42

4.3.1 Moss-Burstein band filling 42

4.3.2 Bandgap renormalisation 45

4.4 Results and discussion 46

4.5 Conclusion 47

Chapter 5 GaInNSb lattice matching **48**

5.1 Introduction 49

5.2 Experimental details 50

5.3 Lattice matching 51

5.4 Results and discussion 51
5.5 Conclusions 56

Conclusions and further work: Dilute nitrides **56**

II Cadmium oxide **59**

Introduction 60

Chapter 6 CdO bandgap and effective mass determination **64**

6.1 Introduction 65
6.2 Experimental details 66
6.3 Results and discussion 66
6.4 Conclusion 74

Chapter 7 Fermi-level stabilisation of cadmium oxide **75**

7.1 Introduction 76
7.2 Experimental details 77
7.3 Results and discussion 78
7.4 Conclusions 84

Conclusions and further work: Cadmium oxide **84**

References **86**

Acknowledgements


```python
#!/usr/bin/python

""" During my Ph.D. I have had the fortune to meet and work with a
number of people without whom the quality and enjoyment of my work
would have been greatly diminished.  I’d like to take this opportunity
to thank these people now in the form of a python program (I find this
to be more effective than interpretive dance, which would have been my
first choice, when used in a written context). """

people = []

""" I’d like to begin by thanking my supervisor Chris "big mac"
McConville for giving me the opportunity to study at Warwick. In
addition, I’d like to commend Chris on his tolerance during our
"monthly" meetings and thank him for his help and support during my
medically induced sabbatical. """

people.append("Chris")

""" Next I’d like to thank Tim Veal for being a constant source of
academic and comic inspiration. I could never have done it without you
dude. Honk! """

people.append("Tim")

""" I’d like to thank Phil "Not a violent man" King for many an
enjoyable trip to campus for lunch/"undergrad bashing". Matt "Rambo"
Humphries is thanked for being the best housemate, friend and gym
partner anyone could ask for. Rob Johnston is thanked for supplying me
with those sticks with cotton wool on the end. Also, Louis Piper, Gavin
Bell, Stu Hatfield, and Lolly... I don’t think Lolly has a surname, are
thanked for their part in numerous legendary coffee room moments. """

people.append("Phil, Rambo, Rob, Louis, Gavin, Stuee and Lolly")

""" Finally, and most importantly of all, I’d like to thank my Mum and
Dad. This work represents 25 years of encouragement, love and support
from you in all my educational exploits, I can never thank you enough
for that, so you’ll have to make do with a copy of this thesis. """

people.append("Mum and Dad")

for p in people:
    print "Thanks very much %s!" % p
```

Declarations

I declare that this thesis contains an account of my research carried out in the Department of Physics at the University of Warwick between October 2004 and December 2007 under the supervision of Prof. C. F. McConville. The research reported here has not been submitted, either wholly or in part, in this or any other academic institution for admission to a higher degree.

The high-resolution x-ray diffraction measurements and simulations were performed by S. Jollands and D. Walker, and the atomic force microscopy measurements by N. R. Wilson (all of the University of Warwick). The helium ion implantation was performed at the Surrey Ion Beam Centre by N. H. Peng (University of Surrey). All remaining collection, simulation, analysis and interpretation of data was performed by the author.

Published articles based on this work

P. H. Jefferson, S. A. Hatfield, T. D. Veal, P. D. C. King, J. Zúñiga-Pérez, V. Muñoz-Sanjosé, and C. F. McConville, *Bandgap and effective mass of epitaxial Cadmium Oxide*, App. Phys. Lett., **92** (2008) 022101.

P. H. Jefferson, L. Buckle, B. R. Bennett, T. D. Veal, D. Walker, N. R. Wilson, L. F. J. Piper, P. A. Thomas, T. Ashley, and C. F. McConville, *Growth of dilute nitride alloys of GaInSb lattice-matched to GaSb*, J. Cryst. Growth, **304** (2007) 338.

P. H. Jefferson, L. Buckle, D. Walker, T. D. Veal, S. Coomber, P. A. Thomas, T. Ashley, and C. F. McConville, *Growth and characterisation of high quality MBE grown* InN_xSb_{1-x}, phys. stat. sol. (RRL), **1** (2007) 104.

P. H. Jefferson, T. D. Veal, L. F. J. Piper, B. R. Bennett, C. F. McConville, B. N. Murdin, L. Buckle, G. W. Smith, and T. Ashley, *Band anticrossing in* GaN_xSb_{1-x}, App. Phys. Lett., **89** (2006) 111921.

T. D. Veal, L. F. J. Piper, S. Jollands, B. R. Bennett, **P. H. Jefferson**, P. A. Thomas, C. F. McConville, B. N. Murdin, L. Buckle, G. W. Smith, and T. Ashley, *Band gap reduction in GaNSb alloys due to the anion-mismatch*, Appl. Phys. Lett., **87** (2005) 132101.

Selected articles to which the author has contributed

P. D. C. King, T. D. Veal, **P. H. Jefferson**, S. A. Hatfield, L. F. J. Piper, C. F. McConville, F. Fuchs, J. Furthmüller, F. Bechstedt, Hai Lu and W. J. Schaff, *Determination of the branch-point energy of InN: Chemical trends in common-cation and common-anion semiconductors*, Phys. Rev. B **77** (2008) 045316.

P. D. C. King, T. D. Veal, **P. H. Jefferson**, C. F. McConville, Hai Lu, and W. J. Schaff, *Variation of band bending at the surface of Mg-doped InGaN: Evidence of p-type conductivity across the composition range*, Phys. Rev. B **75** (2007) 115312.

L. Colakerol, T. D. Veal, H.-K. Jeong, L. Plucinski, A. DeMasi, T. Learmonth, P.-A. Glans, S. Wang, Y. Zhang, L. F. J. Piper, **P. H. Jefferson**, A. Fedorov, T.-C. Chen, T. D. Moustakas, C. F. McConville, and K. E. Smith, *Quantized electron accumulation states in indium nitride studied by angle-resolved photoemission spectroscopy*, Phys. Rev. Lett. **97** (2006) 237601.

T. D. Veal, **P. H. Jefferson**, L. F. J. Piper, C. F. McConville, T. B. Joyce, P. R. Chalker, L. Considine, Hai Lu, and W. J. Schaff, *Transition from electron accumulation to depletion at InGaN surfaces*, Appl. Phys. Lett. **89** (2006) 202110.

L. F. J. Piper, T. D. Veal, **P. H. Jefferson**, C. F. McConville, F. Fuchs, J. Furthmüller, F. Bechstedt, Hai Lu, and W. J. Schaff, *Valence-band structure of InN from x-ray photoemission spectroscopy*, Phys. Rev. B **72** (2005) 245319.

T. D. Veal, L. F. J. Piper, **P. H. Jefferson**, I. Mahboob, C. F. McConville, M. Merrick, T. J. C. Hosea, B. N. Murdin, and M. Hopkinson, *Photoluminescence spectroscopy of bandgap reduction in dilute InNAs alloys*, Appl. Phys. Lett. **87** (2005) 182114.

Conference presentations based on this work

P. H. Jefferson, S. Coomber, L. Buckle, T. D. Veal, B. R. Bennett, C. F. McConville, and T. Ashley. *Dilute nitride antimonide alloys: Growth and characterisation for long wavelength applications.* Oral presentation at the Thirteenth International Conference on Narrow Gap Semiconductors, University of Surrey, Guildford, UK - July 2007.

P. H. Jefferson, L. Buckle, T. D. Veal, B. R. Bennett, T. Ashley and C. F. McConville. *Dilute nitride antimonide alloys.* Oral presentation (winner of graduate prize) at the European Materials Research Society Spring Meeting 2007, Palais de la musique et des congres, Strasbourg, France - May/June 2007.

P. H. Jefferson, T. D. Veal, L. F. J. Piper, D. Walker, C. F. McConville, L. Buckle, T. Ashley and B. R. Bennett. *Bandgap reduction and lattice matching in dilute nitride antimonide alloys.* Oral presentation at the 48th Electronic Materials Conference of the Minerals, Metals and Materials Society, Pennsylvania, USA - June 2006.

P. H. Jefferson, T. D. Veal, L. F. J. Piper, C. F. McConville, M. Merrick, T. J. C. Hosea, B. N. Murdin, L. Buckle, T. Ashley, B. R. Bennett and M. Hopkinson. *Mid-infrared dilute nitrides: optical properties of InNAs and GaNSb.* Poster presentation at Condensed Matter and Materials Physics conference 2006, University of Exeter, UK - April 2006.

P. H. Jefferson, T. D. Veal, L. F. J. Piper, C. F. McConville, L. Buckle, B. R. Bennett and T. Ashley. *GaNSb: a new material for mid-infrared optoelectronic devices.* Oral presentation at the 2005 Mid-infrared Optoelectronics: Materials and Devices conference, University of Lancaster, UK - September 2005.

P. H. Jefferson, T. D. Veal, L. F. J. Piper, S. Jollands, P. A. Thomas, C. F. McConville, L. Buckle, G. W. Smith, B. R. Bennett and T. Ashley. *Growth and optical characterisation of GaNSb.* Poster presentation at the 2005 Mid-infrared Optoelectronics: Materials and Devices conference, University of Lancaster, UK - September 2005.

Abstract

Dilute nitride alloys of III–V semiconductors, and transparent conducting group-II oxides may both be categorised as highly mismatched compounds. The small size and high values of electronegativity of nitrogen and oxygen (see figure), compared to the substituted anion, in dilute nitrides, and the cation, in transparent conducting oxides, give rise to striking properties in these materials.

VIIIB

F – Fluorine
3.98

VIIA	VIIIA	VIIIA	VIIIA	IB	IIB	IIIB	IVB	VB	VIB
						5 B 2.04	6 C 2.55	7 N 3.04	8 O 3.44
						13 Al 1.61	14 Si 1.90	15 P 2.19	16 S 2.58
					30 Zn 1.65	31 Ga 1.81	32 Ge 2.01	33 As 2.18	34 Se 2.55
					48 Cd 1.69	49 In 1.78	50 Sn 1.96	51 Sb 2.05	52 Te 2.10

The dilute nitride alloys GaNSb, InNSb, and GaInNSb, grown by molecular beam epitaxy, have been studied. Infrared absorption measurements of GaNSb are presented, showing the divergence of transitions from the valence band to E_- and E_+ conduction bands with increasing nitrogen incorporation. The fitting of the positions of the valence band to E_+ transitions gives a value of 2.6 eV for the coupling parameter in this material. A reduction in the bandgap of InNSb from that of InSb is shown by modelling the competing effects of Moss-Burstein band filling and bandgap renormalisation. Finally, bandstructure calculations of the quaternary material GaInNSb, with dilute incorporations of nitrogen and indium, show that the material is suitable for the exploitation of the 8–14 μm atmospheric transmission window. Structural characterisation of GaInNSb shows that this material can be grown lattice matched to GaSb with nitrogen and indium incorporations of 1.8 and 8.4 per cent, respectively.

The conducting oxide CdO, grown by metal-organic vapour-phase epitaxy, has also been studied. Analysis and simulation of infrared reflectance data, including conduction band non-parabolicity and Moss-Burstein band filling, reveal bandgap and band-edge effective mass values of 2.16 eV and 0.21 m_0, respectively. In addition, high energy $^4He^+$ ion irradiation was used to stabilise the Fermi level in CdO. Carrier statistics calculations were performed and the charge neutrality level was found to be 2.52 eV with respect to the Γ-point valence band maximum, corresponding to 0.36 eV above the conduction band minimum. The location of the charge neutrality level within the conduction band explains the propensity for high unintentional n-type doping, and the high conductivity observed in CdO.

Abbreviations

AFM	Atomic force microscope
ADM	Amphoteric defect model
BAC	Band anticrossing
CBM	Conduction band minimum
CNL	Charge neutrality level
DFT	Density functional theory
FTIR	Fourier-transform infrared
FWHM	Full width at half maximum
MBE	Molecular beam epitaxy
MOVPE	Metal-organic vapour-phase epitaxy
NIEL	Non-ionising energy loss
RF	Radio frequency
RSM	Reciprocal space map
RT	Room temperature
SRIM	Stopping and range of ions in matter
TCO	Transparent conducting oxide
VBM	Valence band maximum
VCA	Virtual crystal approximations
XRD	X-ray diffraction

α	Non-parabolicity parameter ($1/E_g$); absorption coefficient; Lindsay/O'Reilly parameter
β	Lindsay/O'Reilly parameter
c	Speed of light (2.998×10^8 ms^{-1})

C_{MN}	BAC coupling parameter cf. Lindsay/O'Reilly β parameter
Δ_{so}	Spin-orbit split-off energy
e	Electronic charge (1.6022×10^{-19} C)
$\tilde{\epsilon}$	Complex permittivity
ϵ_0	Permittivity of free space (8.854×10^{-12} N^{-1} m^{-2} C^2)
$\epsilon(0)$	Static dielectric constant
$\epsilon(\infty)$	High frequency dielectric constant
E_{bgr}	Bandgap renormalisation energy
E_F	Fermi energy
E_g	Zone-centre bandgap
E_M	Host conduction band energy
E_{mb}	Moss-Burstein band-filling
E_N	Nitrogen energy level
γ	Lindsay/O'Reilly parameter; phonon damping
γ^L	Luttinger parameter
g_{ba}	Joint density of states between band a and band b
h	Planck's constant
$\hbar$	$h/2\pi$
$\mathbf{k}$	Wavevector
$m^*_{e/h}$	Electron/hole effective mass
n	Carrier concentration; refractive index
R	Reflectance
r	Coefficient of reflection
τ	Free-carrier scattering time
t	Coefficient of transmission
V_{MN}	BAC interaction matrix element
ω_P	Plasma frequency
ω_{TO}	TO-phonon frequency

Chapter 1

Introduction

1.1 Historical background

1.1.1 Dilute nitrides of III–V materials

Initial interest in the growth of dilute nitride alloys of III–V semiconductors was to utilise the bandgap range between the III–nitrides and the III–arsenides. It was thought that the growth of GaNAs across the entire composition range from GaAs, with a room temperature (RT) bandgap of 1.42 eV (near-infrared) [1], to GaN, with a RT bandgap of 3.4 eV (ultraviolet) [2], would facilitate the fabrication of optoelectronic devices spanning the entire visible spectrum. Despite the expected miscibility gap between GaAs and GaN [3,4], samples of GaN_xAs_{1-x} with $x \simeq 0.016$ were fabricated [5]. Rather than an increase in energy of the alloy's bandgap from that of GaAs, as would be expected from the virtual crystal approximation, it was found to decrease rapidly with increasing nitrogen incorporation. In addition, it was observed that the incorporation of nitrogen caused a decrease in the material's lattice constant, as is predicted from Vegard's empirical law [6]. This allowed the lattice matching of GaNAs to Si [7], and of GaInNAs to GaAs with a bandgap in the technologically important 1.3–1.55 μm range [8]. Due to their potential for use in devices for data- and tele-communications [9] and as active layers in multi-junction solar cells [10], dilute nitride alloys of Ga(In)As and Ga(In)P [11,12] have received a great deal of attention.

Prior to the work of Buckle *et al.* [13] and subsequently Veal *et al.* [14], research into dilute

nitrides of group-III antimonide materials was very limited [15], despite their potential for the exploitation of the atmospheric transmission window of 8–14 μm. The use of antimony had been limited to low [16] and moderate [17] inclusions in the alloy Ga(In)NAs (with Sb replacing As), to further reduce the bandgap from that of GaAs, in order to produce devices operating at 1.55 μm for telecommunications applications.

1.1.2 Transparent conducting oxides

Transparent conducting oxides (TCOs) represent an exceptional class of materials. It would be expected that the pre-requisites for optical transparency, an electronic bandgap in excess of $\sim$3 eV, and conductivity, the presence of conduction band electrons, would be mutually exclusive. However, the wide bandgap materials In_2O_3, SnO_2, and ZnO exhibit these properties due to their strong propensity for unintentional n-type doping. Both conductivity and transparency in these materials can be increased by additional extrinsic doping, as is seen in the commonly used Sn doped In_2O_3 [18–20].

TCOs are used in a wide variety of applications including transparent contacts for thin film transistor liquid crystal displays and photovoltaics [21, 22], and in light emitting diodes [23, 24]. Recent interest in ZnO, with a RT bandgap of $\sim$3.4 eV and large exciton binding energy of $\sim$60 meV, has mainly been focussed on its use in optoelectronic applications operating at blue and ultraviolet wavelengths with a high quantum efficiency [24, 25]. A reduction in the bandgap of ZnO by alloying with CdO, a conducting oxide with a bandgap smaller than that of ZnO, has been demonstrated in optoelectronic applications operating at blue-green wavelengths [26, 27].

1.2 Organisation of the thesis

The remainder of this chapter provides a general background to semiconductors and bandstructure approximations, along with descriptions of the unusual bandstructure of dilute nitride alloys of III–V semiconductors. Chapter 2 outlines the theoretical principles of the experimental techniques employed during this research.

The experimental section of the thesis is separated into two parts. The first part (chapters

3 to 5) details experimental results, with discussion and conclusions, of the optoelectronic properties and basic characterisation of the highly anion-mismatched alloy semiconductors gallium nitride antimonide, indium nitride antimonide and the related quaternary alloy gallium indium nitride antimonide. The second part (chapters 6 and 7) details experimental results, with discussion and conclusions, of the basic band parameters and the Fermi-level stabilisation energy of the significantly cation-anion mismatched semiconductor cadmium oxide.

1.3 Semiconductor crystal structure

The most common semiconductors are the elemental crystals of group IV, e.g. silicon and germanium, and binary compounds containing elements of group III and V, e.g. gallium arsenide and indium antimonide. With the exception of III–N compounds, these materials crystallise into the zinc blende structure (known as the diamond structure for elemental crystals). This structure, illustrated for a compound material in figure 1.1, consists of two interpenetrating face-centred cubic lattices offset along the body diagonal by one quarter of the length of the diagonal. For binary compounds, atoms A and B represent different elements (zinc blende structure) and for elemental semiconductors atoms A and B represent the same element (diamond structure).

The crystal structure adopted by the group-III nitrides and a number of the II–VI semiconductor compounds (e.g. zinc oxide and cadmium sulphide) is the wurtzite structure and is indicative of the increased ionicity found in the bonding of these materials. In the wurtzite structure each atom of one element is surrounded tetrahedrally by four atoms of a second element, as in the zinc blende structure, however, the locations of the atoms are such that they make up two interpenetrating close-packed hexagonal lattices.

The final structure of interest is the rocksalt structure. Normally associated with ionic insulators, the rocksalt structure is adopted at ambient temperature and pressure by the semiconductor cadmium oxide. Structurally it consists of two interpenetrating face-centred cubic lattice of different elements offset along the body diagonal by one half of the length of the diagonal.

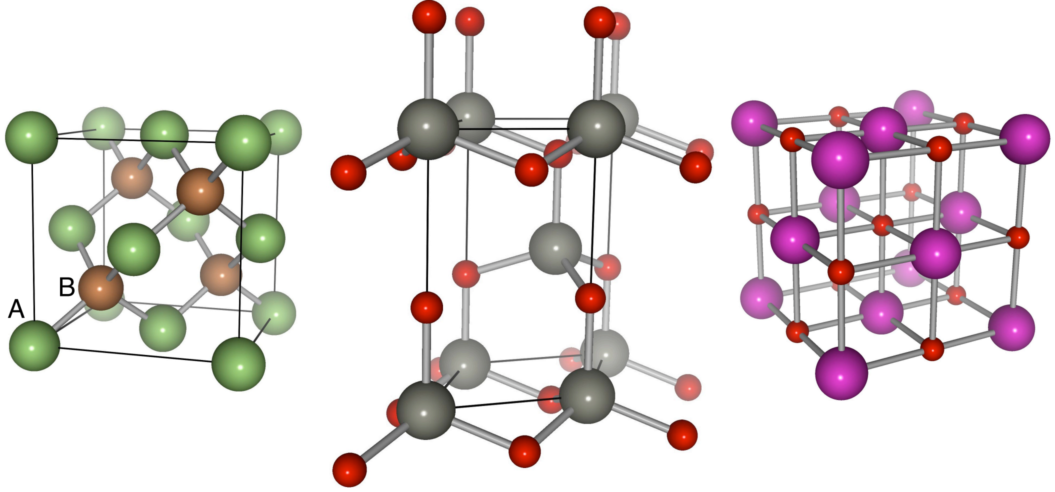

Figure 1.1: The crystal structures (left to right) zinc blende (GaSb), wurtzite (ZnO) and rocksalt (CdO).

1.4 Energy band structure

The periodic potential resulting from the atomic nuclei in the crystal structures described in the previous section gives rise to a series of energy bands in such solids describing the allowed energies as a function of wavevector (or quasi-momentum). This can be simply considered for an ideal lattice by an effective one-electron potential $U(\mathbf{r})$ which, for a given electron, contains the combined potential of the atomic nuclei and of other electrons. Bloch's theorem [28] states that the eigenstates of the one-electron Hamiltonian:

$$H = -\frac{\hbar^2 \nabla^2}{2m} + U(\mathbf{r}) \tag{1.1}$$

where $U(\mathbf{r} + \mathbf{R}) = U(\mathbf{r})$ for all $\mathbf{R}$ in a Bravais lattice, can be chosen to have the form of a plane wave times a function with the periodicity of the Bravais lattice,

$$\psi_{n\mathbf{k}}(\mathbf{r}) = e^{i\mathbf{k}\cdot\mathbf{r}} u_{n\mathbf{k}}(\mathbf{r}) \tag{1.2}$$

The index n in the Bloch theorem is given because for any $\mathbf{k}$ there are many solutions to the Schrödinger equation. The solutions are given by the eigenvalue problem:

$$\begin{aligned} H_{\mathbf{k}} u_{\mathbf{k}}(\mathbf{r}) &= \left(\frac{\hbar^2}{2m} \left(\frac{1}{i}\nabla + \mathbf{k} \right)^2 + U(\mathbf{r}) \right) u_{\mathbf{k}}(\mathbf{r}) \\ &= \epsilon_{\mathbf{k}} u_{\mathbf{k}}(\mathbf{r}) \end{aligned} \tag{1.3}$$

As the wavevector only appears as a parameter in the Hamiltonian, the energy levels for a given index, n, will vary continuously with $\mathbf{k}$. In this way, the allowed energy values for a

given index, or band, are described by the function $\epsilon_n(\mathbf{k})$. An example of the bandstructure of a semiconductor calculated by a pseudopotential method is given in figure 1.2, where the starting point for the calculation was equation 1.1.

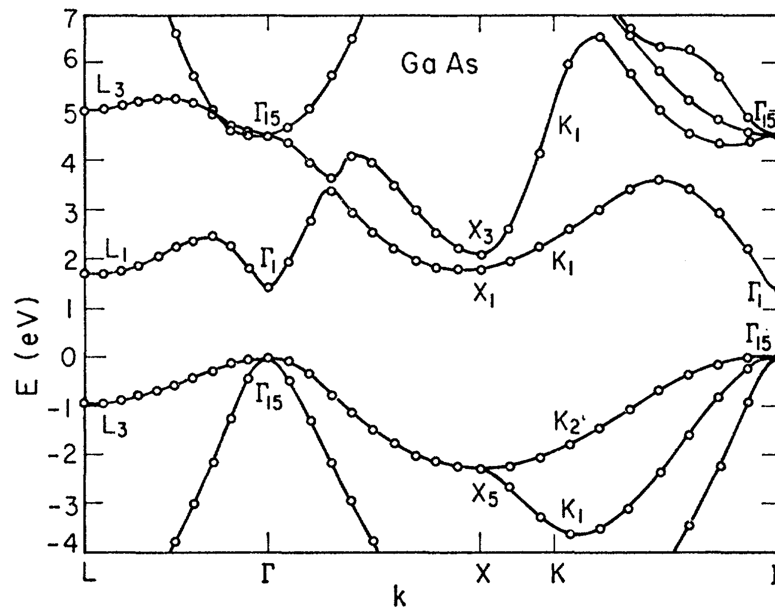

Figure 1.2: The bandstructure of zinc blende gallium arsenide calculated by a pseudopotential method between a number of high symmetry points [29]

1.5 Bandstructure approximations

1.5.1 Parabolic approximation

For electronic transport problems, the properties of a given semiconductor are determined by the small proportion of electrons close to the lowest conduction band minimum (CBM) and holes near the highest valence band maximum (VBM). These carriers are either produced by doping with donors (electrons) or acceptors (holes) or by excitation (thermal or optical) across the bandgap. For a direct-gap semiconductor, where the VBM and the CBM are coincident in $\mathbf{k}$-space, the energy-band dispersions can be approximated by means of a Taylor expansion about $\mathbf{k} - \mathbf{k}_0$, where $\mathbf{k}_0$ is the value of $\mathbf{k}$ where the extrema occur.

$$E(\mathbf{k} - \mathbf{k}_0) = E(0) + A|\mathbf{k} - \mathbf{k}_0|^2 + B|\mathbf{k} - \mathbf{k}_0|^4 + \dots \tag{1.4}$$

Due to symmetry considerations in direct-gap III–V semiconductors, the extrema occur at the Brillouin zone centre (the Γ-point) where $\mathbf{k} = \mathbf{k}_0 = 0$. In addition, the effect of the higher power terms of $\mathbf{k}$ are negligible, therefore, equation 1.4 can be written:

$$E(\mathbf{k}) \approx E(0) + Ak^2 \tag{1.5}$$

By analogy with the free electron energy dispersion, it is convenient to define A to be $\hbar^2/2m_e^*$ where m_e^* is the effective mass of the conduction band electrons, or $-\hbar/2m_h^*$ for valence band holes. The effective mass is, in the general case, a tensor quantity. However, for direct-gap semiconductors which crystallise into the zinc blende structure, the electron and hole dispersions are isotropic close to the Γ-point, and the effective mass can be reduced to a scalar quantity.

This results in the so called parabolic approximation of energy dispersion, shown in equation 1.6 where E_g is the energy bandgap of the material, and the zero of energy is defined as midgap.

$$E_{e,h}(\mathbf{k}) \approx \pm\frac{E_g}{2} \pm \frac{\hbar^2 k^2}{2m_{e,h}^*} \tag{1.6}$$

This approximation is good for wide gap semiconductors (e.g. GaAs whose room temperature bandgap is ∼1.4 eV) however, as E_g decreases, the higher order terms neglected in equation 1.4 become increasingly important causing the conduction band dispersion to deviate from the parabolic approximation such that equation 1.6 ceases to well describe the bandgap for narrow gap semiconductors (e.g. InSb, whose room temperature bandgap is ∼0.17 eV).

1.5.2 8-band $\mathbf{k} \cdot \mathbf{p}$ (neglecting the effect of higher bands)

Rather than attempt to calculate the higher order terms in equation 1.4, a simpler, accurate method to calculate the bandstructure of narrow gap semiconductors is given by Kane [30,31]. The $\mathbf{k} \cdot \mathbf{p}$ perturbation method employed by Kane exploits the fact that the cell periodic functions for any $\mathbf{k}$ (belonging to different bands) form a complete set. It is therefore possible to express the wavefunctions of the electrons for any $\mathbf{k}$ in terms of a point of known parameters, in this case the Brillouin zone centre (Γ) where the required parameters are assumed known (or can be fitted to experiment). The starting point is the

independent electron Hamiltonian,

$$H = \frac{p^2}{2m_0} + V_0(\mathbf{r}) + V_{so} \tag{1.7}$$

where $\mathbf{p} = -i\hbar\nabla$, $V_0(\mathbf{r})$ is the periodic potential due to the crystal lattice and V_{so} is the spin-orbit interaction. The eigenfunctions of H are Bloch functions giving the time-independent Schrödinger equation (after eliminating the factor $e^{i\mathbf{k}\cdot\mathbf{r}}$):

$$\left(\frac{p^2}{2m_0} + \frac{\hbar}{m_0}\mathbf{k}\cdot\mathbf{p} + \frac{\hbar^2 k^2}{2m_0} + V_0(\mathbf{r}) + V_{so}\right) u_{n\mathbf{k}}(\mathbf{r}) = E_{n\mathbf{k}} u_{n\mathbf{k}}(\mathbf{r}) \tag{1.8}$$

In this model, the $\mathbf{k}\cdot\mathbf{p}$ interaction is treated as a perturbation from the zone centre by expanding the unknown function $u_{n\mathbf{k}}(\mathbf{r})$ in terms of the zone centre functions $u_{n\mathbf{0}}(\mathbf{r})$.

Following Kane, equation 1.9 shows a formulation of the 8-band Hamiltonian describing the interaction between the electrons of three valence bands and one conduction band at the zone centre each with spin degeneracy. This neglects the effect of higher (and lower) bands which will only have a small contribution provided $\mathbf{k}$ is not too large.

$$\begin{aligned} H &= \begin{bmatrix} \tilde{H} & 0 \\ 0 & \tilde{H} \end{bmatrix} \\ \tilde{H} &= \begin{bmatrix} E_s & \frac{1}{\sqrt{2}}\hbar kc & -\hbar kc & 0 \\ \frac{1}{\sqrt{2}}\hbar kc & E_p - \frac{2}{3}\Delta & 0 & 0 \\ -\hbar kc & 0 & E_p + \frac{1}{3}\Delta & 0 \\ 0 & 0 & 0 & E_p + \frac{1}{3}\Delta \end{bmatrix} \end{aligned} \tag{1.9}$$

Here, E_s and E_p are the eigenvalues of $\{(p^2/2m_0) + V_0 + V_{so}\}u_{i\mathbf{0}} = E_{i\mathbf{0}}u_{i\mathbf{0}}$, where $u_{i\mathbf{0}}$ are the zone centre functions of the bands considered, Δ is the spin-orbit split-off energy and c is related to Kane's matrix element (P) by $c = (2/3)^{1/2}P/\hbar$. c has the dimensions of velocity and is $\sim 1/300$ the velocity of light for all III–V semiconductors. As the off-diagonal block elements of H are zero, the 8×8 Hamiltonian collapses to a 4×4 matrix without loss of information. Further simplification of the Hamiltonian can be performed in the case where $\Delta \gg E_g$.

1.5.3 2-band $\mathbf{k}\cdot\mathbf{p}$: the α-approximation

In the case where the spin-orbit split-off energy is significantly greater than that of the material bandgap the Hamiltonian can be reduced to the 2×2 matrix shown below, where

$\hbar\mathbf{k}$ is written as p.

$$H = \begin{bmatrix} E_s & -pc \\ -pc & E_p + \frac{1}{3}\Delta \end{bmatrix} \tag{1.10}$$

Selecting the zero of energy to be the centre of the bandgap ($E_s = E_g/2$ and $E_p + \Delta/3 = -E_g/2$) and solving the Schrödinger equation, $H_{ij}\psi = E_j\psi$ for equation 1.10 yields an analytical expression for the 2-band $\mathbf{k}\cdot\mathbf{p}$ approximation:

$$E^2 = (pc)^2 + \left(\frac{E_g}{2}\right)^2 = p^2c^2 + (m^*)^2c^4 \tag{1.11}$$

where m^* is defined as $E_g/2c^2$, it should be noted that this is the equation of a relativistic particle with rest mass m^* and maximum velocity $c \approxeq c_{\text{light}}/300$. Re-arranging equation 1.11, such that the zero of energy is located at the conduction band minimum, the α-approximation representation of the 2-band model can be obtained.

$$E(1 + \alpha E) = \frac{p^2}{2m^*} \tag{1.12}$$

where $\alpha = 1/E_g$, justifying the above definition of m^*. The α-approximation provides an intuitive method of calculating the non-parabolicity of a bandstructure due to its direct link to the bandgap of the material. It can be seen that as E_g is increased $\alpha \to 0$ and the parabolic approximation is recovered.

1.5.4 Pidgeon and Brown 8-band $\mathbf{k}\cdot\mathbf{p}$ Hamiltonian

The Pidgeon and Brown 8-band $\mathbf{k}\cdot\mathbf{p}$ Hamiltonian [32] in the zero field limit is shown in equation 1.13. As before, the 8×8 Hamiltonian can be expressed without loss of information by the 4×4 matrix shown below due to spin degeneracy.

$$H = \begin{bmatrix} E_g + E_{par}F & 0 & \sqrt{\frac{2}{3}E_P E_{par}} & -\sqrt{\frac{1}{3}E_P E_{par}} \\ 0 & -\frac{1}{2}(\Gamma_1 - 2\Gamma_2)E_{par} & 0 & 0 \\ \sqrt{\frac{2}{3}E_P E_{par}} & 0 & -\frac{1}{2}(\Gamma_1 + 2\Gamma_2)E_{par} & \sqrt{2}\Gamma_2 E_{par} \\ -\sqrt{\frac{1}{3}E_P E_{par}} & 0 & \sqrt{2}\Gamma_2 E_{par} & -\Delta_{so} - \frac{1}{2}\Gamma_1 E_{par} \end{bmatrix} \tag{1.13}$$

In this formulation, the effect of the interactions between the four bands is included in the E_p term which is related to the Kane parameter P by $E_p = 2m_0P^2/\hbar^2$. The interactions

between remote bands and the conduction band are taken into account through second-order perturbation theory and are described by the Kane parameter F which may be expressed in terms of the bandgap, spin-orbit split-off energy and the effective mass,

$$\frac{1}{m_e^*} = (1 + 2F) + \frac{E_p(E_g + 2\Delta_{so}/3)}{E_g(E_g + \Delta_{so})} \tag{1.14}$$

Similarly, the effect of higher-order bands on the valence bands are incorporated in the $\Gamma_{1,2}$ terms which are defined in terms of the Luttinger parameters, $\gamma^L_{1,2}$,

$$\Gamma_1 = \frac{\gamma_1^L - E_p}{3E_g} \quad \text{and} \quad \Gamma_2 = \frac{\gamma_2^L - E_p}{6E_g} \tag{1.15}$$

Finally, $E_{par} = \hbar^2 k^2/2m_0$ is the free-electron energy, E_g the electronic bandgap and Δ_{so} the spin-orbit split-off energy.

A comparison between the three models of the semiconductor bandstructure described is shown graphically in figure 1.3. The Pidgeon and Brown 8-band $\mathbf{k} \cdot \mathbf{p}$ model gives three valence bands (heavy, light and spin-orbit split-off hole bands) and one conduction band. A single conduction band and valence band (light hole) are shown for the α-approximation, and finally, the parabolic approximation is shown for the conduction band only. For each case, the parameters for InSb were taken from a review of III–V semiconductors [1].

For the narrow gap semiconductor InSb, it is expected that the 8-band Pidgeon and Brown model will give the most accurate description of the bandstructure, as it takes into consideration the effect of higher bands, in addition to the 8-bands explicitly considered. In addition, unlike the 2-band model, it makes no assumption with respect to the spin-orbit split-off energy, Δ_{so}. With increasing $\mathbf{k}$, the parabolic expression will give the most inaccurate description as it merely gives the exact solution to a given band at the zone centre.

1.6 Dilute nitride bandstructure

The incorporation of dilute quantities of nitrogen into III–V semiconductor compounds is known to result in a decrease in both the bandgap and lattice parameter of the material from that of the host compound [33]. This effect has been observed in many materials including GaNP [34], GaNAs [5] and InNAs [35], and is a result of the small size and large electronegativity of the nitrogen atom compared to that of the anion it replaces.

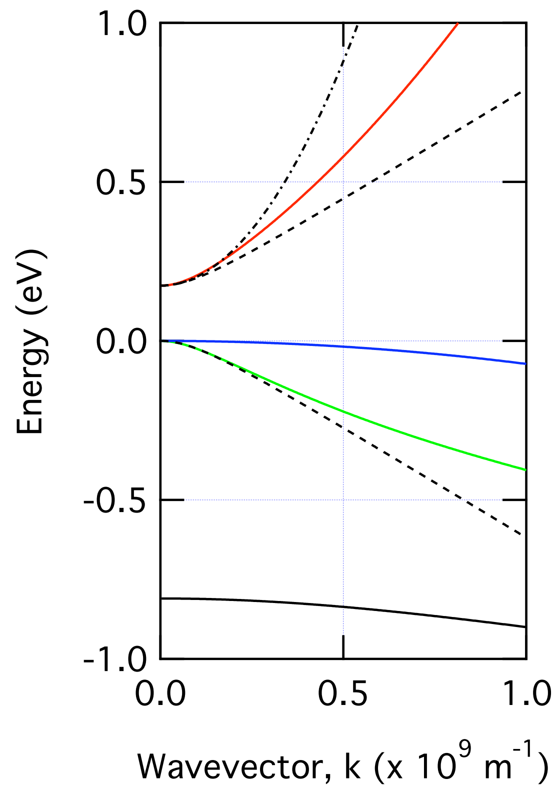

Figure 1.3: Bandstructure calculations for InSb. The solid lines show the Pidgeon and Brown 8-band $\mathbf{k} \cdot \mathbf{p}$ model with three valence bands, heavy hole (blue), light hole (green) and spin-orbit split-off (black) and one conduction band (red). The dashed line shows the α-approximation (showing conduction and light hole bands) and dot-dashed line the parabolic conduction band.

The usual result of reducing the bandgap of a binary III–V semiconductor, by introducing a third element of group III or V, is to increase the lattice constant. This can be seen in figure 1.4 where the bandgap as a function of lattice constant is shown for a number of mixed cation/anion compounds together with some dilute nitride alloys.

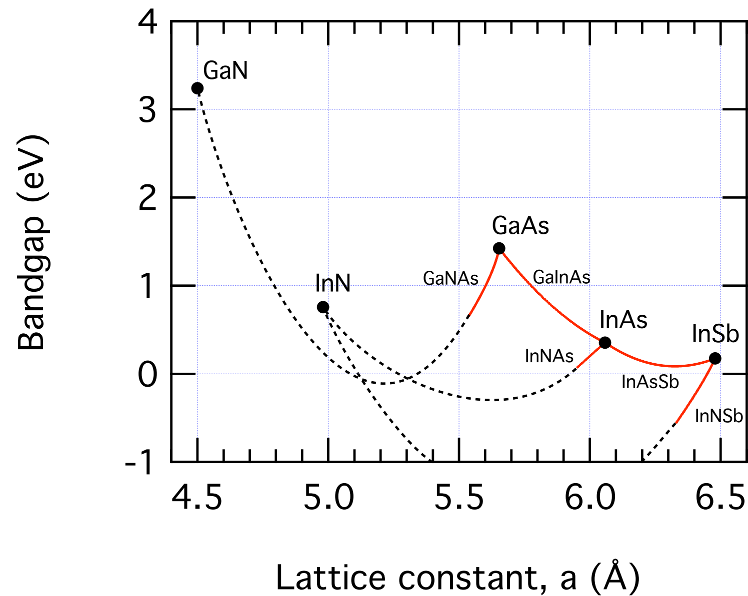

Figure 1.4: The bandgap as a function of lattice constant for various mixed cation/anion compounds, including some dilute nitride alloys.

1.6.1 Deviation from the virtual crystal approximation

As a first approximation, the properties of a ternary semiconductor compound, e.g. III–V–V′, can be determined by a linear interpolation between the properties of the endpoint binary compounds, in our example: III–V and III–V′. This method is known as the virtual crystal approximation (VCA) as it describes an ideal crystal with an averaged or *virtual* potential with the effects of lattice disorder neglected. A successful application of the VCA is Vegard's empirical law [6], which can be used to determine the lattice constant of ternary semiconductor compounds.

The dependence of other properties of ternary semiconductor compounds are generally not linear. An example of this is the bandgap where a bowing term quadratic in composition

is used to describe the observed deviation from the VCA.

$$E_g^{A_{1-x}B_x} = (1-x)E_g^A + xE_g^B - bx(1-x) \tag{1.16}$$

Here, E_g^μ is the bandgap of material μ, x is the fraction of the binary compound B, and b is a constant for a given alloy and is referred to as the bowing parameter. The magnitude of b is dependent on the constituent binary compounds A and B, but is typically a fraction of an electron-volt and not dependent on the composition of the material. The bandgaps of the non-nitrogen containing compounds in figure 1.4 were calculated using equation 1.16 together with values for the required material-dependent parameters from a review of the band parameters of III–V compound semiconductors and their alloys by Vurgaftman *et al.* [1].

A much greater deviation from the VCA is observed in the bandgap of dilute nitride alloys of III–V compounds than in non-nitrogen containing mixed cation or anion III–V alloys. The inclusion of just 1 per cent nitrogen into GaAs results in a reduction in bandgap from that of the host material of ∼0.12 eV [5]. Describing this in terms of equation 1.16 gives a bowing parameter which, for $x = 0.01$, is ∼14 eV, a value much greater than that observed in non-nitrogen containing ternary alloys. More importantly, however, the bowing parameter for dilute nitride alloys is *composition dependent*. Therefore the functional form of an equation capable of describing such materials is different from that of equation 1.16.

The significant deviation from the VCA observed in III–N–V compounds is due to the isoelectronic nature of the substitutional nitrogen within the III–V host. Though the nitrogen atom has the same electron valence as the atom it is replacing, its other properties (size, electronegativity, bond length etc.) are significantly different, as shown in table 1.1. This results in a considerable, and highly localised, perturbation to the electronic potential surrounding the substitutional atom. Therefore, a nitrogen atom within a III–V host is seen as electronically neutral other than in the immediate vicinity of the atom, leading to a highly spatially localised defect potential [36].

Tight-binding calculations have shown this isolated nitrogen defect level to be resonant with the host conduction band in a number of III–V semiconductor compounds including GaAs, InAs, GaSb, and InSb [37, 38]. The interaction between this resonant defect level

Table 1.1: The atomic radii and Pauling electronegativities of the common group V elements.

Element	Atomic radius (Å)	Pauling electronegativity
Nitrogen	0.65	3.04
Phosphorus	1.00	2.19
Arsenic	1.15	2.18
Antimony	1.45	2.05

and the host conduction band is the basic premise behind the most popular description of III–N–V semiconductors, the band anticrossing model.

1.6.2 The band anticrossing model

The band anticrossing (BAC) model describes the interaction between the host III–V conduction band, E_M, and the resonant nitrogen level, E_N, by means of a simple two-level interaction, parameterised by the matrix element V_{MN}. This method was first used to describe the rapid decrease in bandgap with nitrogen incorporation of the quaternary alloy $\mathrm{Ga}_{1-y}\mathrm{In}_y\mathrm{N}_x\mathrm{As}_{1-x}$ [39]. The 2×2 BAC Hamiltonian matrix for a given $\mathbf{k}$ is

$$H_{\mathrm{BAC}} = \begin{bmatrix} E_M(\mathbf{k}) & V_{MN} \\ V_{MN} & E_N \end{bmatrix} \tag{1.17}$$

The (energy) eigenvalues of this matrix are shown in equation 1.18 and define two non-parabolic bands, conventionally denoted E_- and E_+ for the lower and higher energy bands respectively. The result for $\mathrm{GaN}_x\mathrm{Sb}_{1-x}$, for $x = 0.005$ is shown graphically in figure 1.5 (solid lines) together with the non-interacting result i.e $V_{MN} = 0$ (dotted lines).

$$E_\pm(\mathbf{k}) = \frac{1}{2}\left((E_M(\mathbf{k}) + E_N) \pm \sqrt{(E_M(\mathbf{k}) - E_N)^2 + 4V_{MN}^2}\right) \tag{1.18}$$

The BAC model is the most widely employed description of the bandstructure of dilute nitride semiconductors due to its simplicity and ease of application. However, when the model was first introduced, it was not without its shortcomings. First, the functional form of the interaction matrix element, V_{NM}, with nitrogen incorporation was not known. Second, the model describes only a single nitrogen state (arising from an isolated anion substituted nitrogen atom) interacting with the host conduction band. With increasing

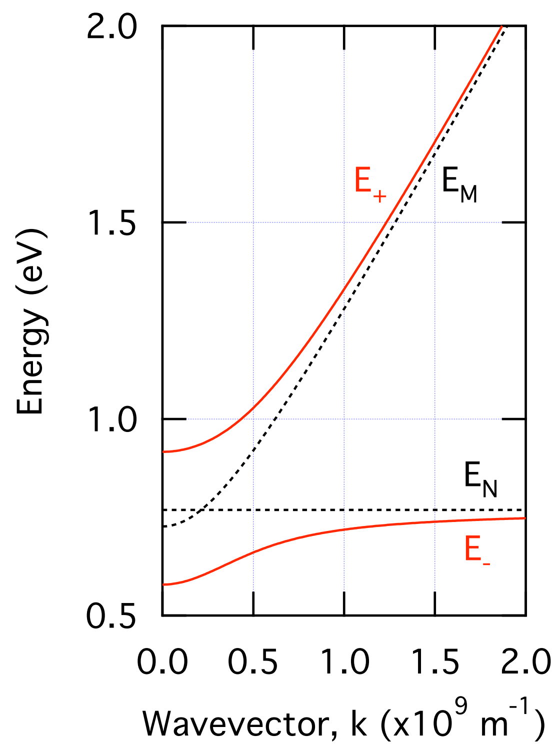

Figure 1.5: The band anticrossing interaction between the host conduction band, $E_M(\mathbf{k})$, and the localised nitrogen level, E_N, coupled by the matrix element V_{MN} for GaN_xSb_{1-x} with $x = 0.005$. The resultant bands E_- and E_+ are shown in red, while the host conduction band and nitrogen levels are shown as dashed lines.

nitrogen incorporation the likelihood of finding N–N pairs and larger complexes increases, and the energy of the states resulting from these complexes would be different from that of the isolated case.

1.6.3 Tight-binding calculations

Theoretical validation of the semi-empirical BAC model was given by the work of Lindsay and O'Reilly, where an sp^3s^* tight-binding Hamiltonian was used to describe the bandstructure of GaNAs [40]. In this work, the electronic structure of GaNAs was determined from the comparison of the conduction band states ψ_{c1} and ψ_{c0} in two supercells, made up of $Ga_{864}N_1As_{863}$ and $Ga_{864}As_{864}$, respectively. The resonant state associated with the isolated nitrogen atom, ψ_{N0}, was derived and was found to be highly localised with in excess of 50 per cent of its probability distribution being found on the nitrogen site or on the sites of the nearest-neighbour gallium atoms. Due to the highly localised nature of the nitrogen state it was found that, for increasing nitrogen concentrations, a linear combination of isolated nitrogen resonant states could be used to accurately describe the nitrogen in the system for nitrogen incorporations to ∼25 per cent.

From this work a 10-band $\mathbf{k}\cdot\mathbf{p}$ Hamiltonian was developed to describe the bandstructure of dilute nitride alloys. The Hamiltonian, based on that of Pidgeon and Brown discussed in the previous section, is shown below.

$$H = \begin{bmatrix} H_{11}^{\mathrm{PB}} - \alpha x & H_{12}^{\mathrm{PB}} & H_{13}^{\mathrm{PB}} & H_{14}^{\mathrm{PB}} & \beta\sqrt{x} \\ H_{21}^{\mathrm{PB}} & H_{22}^{\mathrm{PB}} & H_{23}^{\mathrm{PB}} & H_{24}^{\mathrm{PB}} & 0 \\ H_{31}^{\mathrm{PB}} & H_{32}^{\mathrm{PB}} & H_{33}^{\mathrm{PB}} & H_{34}^{\mathrm{PB}} & 0 \\ H_{41}^{\mathrm{PB}} & H_{42}^{\mathrm{PB}} & H_{43}^{\mathrm{PB}} & H_{44}^{\mathrm{PB}} & 0 \\ \beta\sqrt{x} & 0 & 0 & 0 & E_N - (\alpha+\gamma)x \end{bmatrix} \tag{1.19}$$

The majority of the elements are the same as in the Pidgeon and Brown Hamiltonian (equation 1.13) and are denoted H_{nm}^{PB}. It can be seen that the nitrogen level only directly affects the host conduction band of the system and that the interaction has the functional form $\beta\sqrt{x}$, where β is a material dependent constant and x is the fractional nitrogen incorporation. In addition, the effect of nitrogen pair states and larger complexes is incorporated through the constant γ, which decreases the energy of the nitrogen level

with increasing nitrogen incorporation. The bandstructure of InNSb, with 0.5 per cent nitrogen, calculated using the Lindsay and O'Reilly $\mathbf{k} \cdot \mathbf{p}$ Hamiltonian is shown in figure 1.6.

A comparison between the modified $\mathbf{k} \cdot \mathbf{p}$ Hamiltonian of Lindsay and O'Reilly, and the BAC Hamiltonian of Shan *et al.* reveals that the functional form of the interaction matrix element of the BAC Hamiltonian is $V_{MN} \propto \sqrt{x}$, with the constant of proportionality being β although, in the context of the BAC model, this paramemter is often denoted C_{MN} [41].

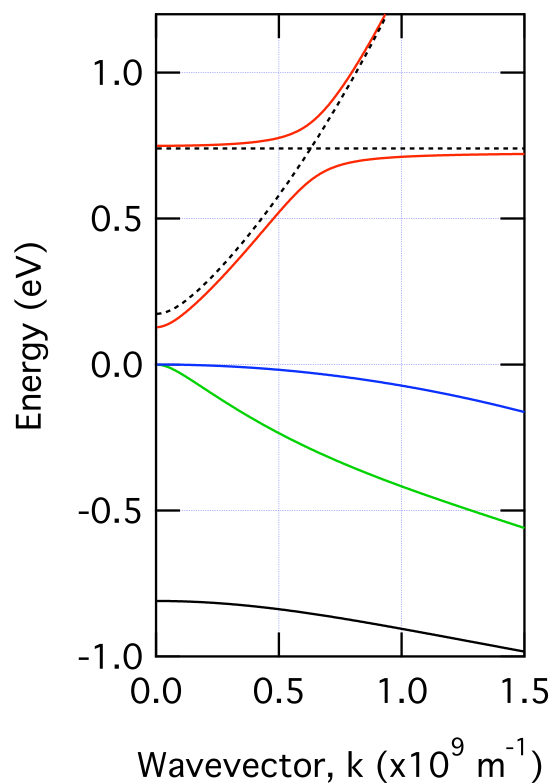

Figure 1.6: The bandstructure of InN_xSb_{1-x} for $x = 0.005$ calculated from Lindsay and O'Reilly's 10-band $\mathbf{k} \cdot \mathbf{p}$ Hamiltonian, and parameters from tight-binding calculations [38]. The valence bands are shown in blue (heavy-hole), green (light-hole) and black (spin-orbit split-off), while the conduction bands are shown in red ($E_{\pm}$). In addition, the resonant nitrogen level and the host conduction band are shown as dashed black lines.

1.6.4 Empirical pseudopotential method

In addition to the simple description of dilute nitride alloys by the BAC model, and the more involved calculations of Lindsay and O'Reilly, another explanation of the effect of nitrogen in III–V semiconductor alloys has been proposed. Similar to that of Lindsay and O'Reilly, this method is based on large supercell calculations, however, the electronic and optical properties are determined from empirical pseudopotential calculations within the local density approximation [42]. Though this description will not be considered further in this work, it is outlined here to give a more balanced overview, and indicate the contentious nature of the research in this field.

In this method, a large supercell is used to describe the system and the constituent components, e.g. Ga, As, N atoms, are placed on lattice sites in any desired configuration (random, clustered, etc.). The use of large supercells has the advantage of allowing many different local environments to be described in the calculation. After the initial setup of the supercell, the relaxed atomic positions are determined from the valence-force-field method where a simple "balls on springs" Hamiltonian is used, allowing the stretching and bending of atomic bonds in the relaxation. The crystal potential $V(\mathbf{r})$ is then described as a superposition of screened atomic pseudopotentials, which can be used to determine the single-particle eigensolutions of the system for very large supercells [43].

The main conclusion of this method is that a breaking of the crystal symmetry of the host III–V lattice, resulting from the incorporation of nitrogen, leads to the splitting of the degenerate L and X conduction band minima. It is proposed that the mixing, or interaction, between the split L and Γ conduction band states leads to the formation of the E_- state, while the E_+ state arises from the mixing of the nitrogen level and the split L conduction band states.

Both the Γ-L-X mixing model and the BAC model provide good qualitative agreement with all available experimental data, however, due to its simple analytical formulation, the BAC model has been most widely applied in the field of dilute nitride alloys of III–V semiconductors.

Chapter 2

Experimental techniques

2.1 Optical absorption spectroscopy

Optical absorption spectroscopy provides a direct and simple method for obtaining information about the bandstructure of a semiconducting material. Photons of a known energy are used to excite electrons in a material to higher lying energy states and, in doing so, information of the optically allowed electronic transitions within the material can be determined.

Fundamental absorption refers to excitations from one electronic band to another. In the case of an ideal, undoped, direct bandgap semiconductor the fundamental absorption transition will take place from the highest occupied valence band to the lowest unoccupied conduction band with the absorption onset occurring within a few meV of the energy of the material bandgap, this process is illustrated in figure 2.1. Using a parabolic description of the bands, the absorption may be defined as $\alpha(h\nu) \propto (h\nu - E_g)^{1/2}$ where α is the absorption coefficient, $h\nu$ is the energy of the incident radiation, and E_g the bandgap of the material [44].

Therefore, the bandgap of a material can be determined by plotting the square of the absorption coefficient as a function of the energy of the incident radiation and taking a linear extrapolation of the fundamental absorption edge to $\alpha^2 = 0$.

Although the bandstructures of the materials considered in this work are not well described by the parabolic band approximation, for small $\mathbf{k}$ the band dispersion will still be parabolic. This can be seen by considering equation 1.12, where the zero of energy is chosen to be at

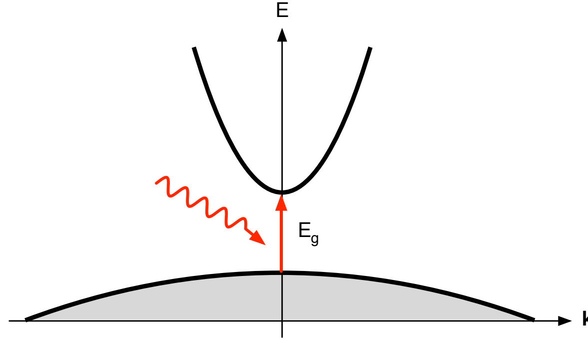

Figure 2.1: The fundamental absorption process illustrating the excitation of an electron from the occupied valence band to the unoccupied conduction band by the absorption of a photon of energy E_g.

$\mathbf{k} = 0$. For small $\mathbf{k}$, E will be small compared to E_g, therefore the αE (of equation 1.12) may be neglected, resulting in a parabolic dispersion. Whereas for large $\mathbf{k}$, the αE term will dominate and the band dispersion will be linear.

It has also been shown experimentally that for materials with non-parabolic bands the fundamental absorption edge of an $\alpha^2(h\nu)$ plot initially increases linearly before deviating at higher values of $h\nu$ (corresponding to higher values of $\mathbf{k}$) [45]. This can also be seen for GaSb in figure 3.1.

In this work, transmission geometry infrared absorption measurements were performed over an energy range of 0.1 to 1.2 eV using a Perkin Elmer Spectrum GX Fourier-transform infrared spectrometer with a narrow gap cadmium mercury telluride detector, and potassium bromide and quartz beamsplitters. Ultaviolet/visible measurements were performed using a Perkin Elmer Lambda 25 spectrometer with a working range of 1.24 to 4.00 eV. All absorption measurements were performed at room temperature. The background absorption by air molecules and the varying intensity of the light source as a function of energy was accounted for by performing a background absorption scan for each set of measurements. The absorption coefficient is determined from the fractional transmission using the relation:

$$T(h\nu) = \frac{(1-R)^2 \exp(-\alpha(h\nu)d)}{1 - R^2 \exp(-2\alpha(h\nu)d)} \tag{2.1}$$

where α is the absorption coefficient, d is the sample thickness, and R is the reflection coefficient at the air/semiconductor interface, which is approximately equal to $\{(n-1)/(n+1)\}^2$, where n is the refractive index of the sample. In the case of the dilute nitrides the

refractive index of the sample was assumed to be approximately equal to that of the host binary.

2.2 Infrared reflectance spectroscopy

Infrared reflectance spectroscopy allows the determination of the plasma frequency of a material. The plasma frequency, ω_p, is dependent on the charge concentration, n, the charge effective mass, m^*, and the high-frequency dielectric constant, $\epsilon(\infty)$, of the material and is given by the relation:

$$\omega_p^2 = \frac{ne^2}{m^*\epsilon(\infty)\epsilon_0} \tag{2.2}$$

where e, is the electronic charge and ϵ_0, the permittivity of free space. A diagram showing a single reflection from the epilayer/substrate interface in a stratified medium is shown in figure 2.2. The angles of incidence and transmittance are denoted θ_i and θ_t, respectively. The refractive indices of the epilayer and substrate are n_2 and n_3, and the epilayer thickness is d.

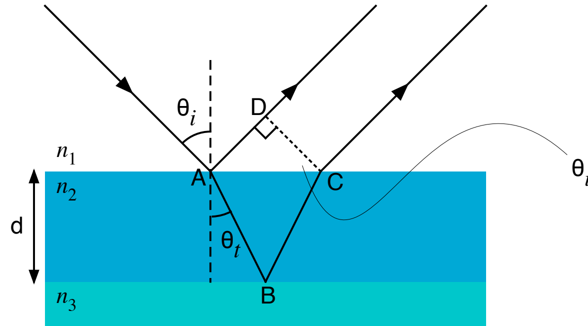

Figure 2.2: A single epilayer/substrate reflection for a material with epilayer thickness d, and a semi-infinite substrate. The radiation strikes the epilayer at angle of incidence θ_i, and is transmitted at an angle θ_t

The Fresnel equations giving the amplitude coefficients of reflection and transmission for light at an angle θ to the surface normal are given below. The refractive indices of the material either side of the interface are n_1 and n_2 (as in figure 2.2) and the polarisation is defined in terms of the electric field with respect to the plane of incidence.

$$\begin{aligned} r_{\parallel} &= \frac{n_2\cos\theta_i - n_1\cos\theta_t}{n_2\cos\theta_i + n_1\cos\theta_t} \quad \text{and} \quad r_{\perp} = \frac{n_1\cos\theta_i - n_2\cos\theta_t}{n_1\cos\theta_i + n_2\cos\theta_t} \\ t_{\parallel} &= \frac{2n_1\cos\theta_i}{n_2\cos\theta_i + n_1\cos\theta_t} \quad \text{and} \quad t_{\perp} = \frac{2n_1\cos\theta_i}{n_1\cos\theta_i + n_2\cos\theta_t} \end{aligned} \tag{2.3}$$

The total reflectance from a sample is determined by summing the contributions from each reflection. Only the first two reflections are shown in figure 2.2. The reflectance from multiple reflections is determined from the geometric sum:

$$\begin{aligned} r &= r_{12} + t_{12} r_{23} t_{21} e^{i\delta} + t_{12} r_{23} r_{21} r_{23} t_{21} e^{i\delta} + \dots \\ &= r_{12} + t_{12} t_{21} r_{23} e^{i\delta} \sum_{n=0}^{\infty} (r_{23} r_{21} e^{i\delta})^n \\ &= r_{12} + \frac{t_{12} t_{21} r_{23} e^{i\delta}}{1 - r_{23} r_{21} e^{i\delta}} \end{aligned} \tag{2.4}$$

where $\delta = \Gamma\omega/c$, accounts for the change in phase of the light travelling through the epilayer. Here, Γ is the path difference between subsequent reflections which, from figure 2.2, is defined:

$$\begin{aligned} \Gamma &= n_2(AB + BC) - AD \\ &= 2dn_2 \left[\frac{1}{\cos\theta_t} - \tan\theta_t \sin\theta_t \right] \\ &= 2dn_2 \cos\theta_t \end{aligned} \tag{2.5}$$

In our case, the incident radiation is unpolarised, therefore, the reflectance is calculated from the average value of the sum of the squared polarised reflectivities:

$$R = \frac{1}{2}(|r_{\parallel}|^2 + |r_{\perp}|^2) \tag{2.6}$$

Simulation of the infrared reflectance spectrum of a material using a suitable model, e.g. the two-oscillator dielectric model, shown in equation 6.1, allows the determination of the plasma frequency of the material and, provided the carrier concentration is known, the effective mass may be calculated.

The reflectance measurements were also performed with a Perkin Elmer spectrum GX spectrometer, working in the energy range 0.1 to 1.2 eV. A Perkin Elmer variable angle specular reflectance stage was used, though all measurements were performed at 35°. The reflectance was determined from the ratio of the reflectance from the sample surface and that from a high reflectivity optical mirror.

2.3 X-ray diffraction

X-rays incident on a crystalline sample are scattered coherently by the periodic array of atoms in the material, giving rise to constructive interference at certain angles of reflection. Diffraction occurs as the wavelength of the incident x-rays is of a similar magnitude to the lattice spacings within the material. The interference of the diffracted x-rays is described by Bragg's Law, which states that constructive interference will occur at an angle θ to the crystal surface when the condition $\lambda = 2d_{hkl} \sin\theta$ is satisfied, where d_{hkl} is the distance between consecutive hkl Miller planes and λ is the incident x-ray wavelength.

For fully relaxed epitaxial layers x-ray diffraction enables the determination of the lattice constant(s) of the layer from solutions of the Bragg equation. For commensurately grown epilayers the degree of strain can be determined by comparison of the asymmetric (parallel to the growth direction) and symmetric (perpendicular to the growth direction) Bragg reflections. In addition, the crystalline quality of an epilayer is often quantified by measuring the full-width at half-maximum of the diffraction peak as any deviation from an ideal lattice acts to broaden the diffraction peak.

Finally, interference fringes, known as Pendellösung or Kato fringes [46], may be used to determine the thickness of films of sufficiently high crystalline quality. The fringes result from multiple scattering and extinction effects within the material [47] and dynamical simulations which account for these effects are used to determine the film thickness.

High resolution x-ray diffraction (XRD) scans around the 004 Bragg reflection, and reciprocal space maps around the 224 asymmetric and 004 symmetric reflections were collected using a Philips PANalytical X'Pert PRO Materials Research Diffractometer with Cu K_α radiation ($\lambda = 0.15406$ nm).

2.4 Hall effect measurements

The physical principle on which Hall measurements is based is the Lorentz force. Electrons moving perpendicular to a magnetic field experience a force normal to the direction of motion and the applied field. When a current is passed through a material (from contact 1 to 3 in part (a) of figure 2.3) with an applied magnetic field perpendicular to the plane

of the sample, a potential difference is induced across the sample (measured across contact 2 and 4 in the figure). From this voltage, known as the Hall voltage, the carrier sheet density can be determined from the relation $V_H = IB/en_s$, where I and B are the applied current and magnetic fields respectively, e the electron charge, and n_s the carrier sheet density.

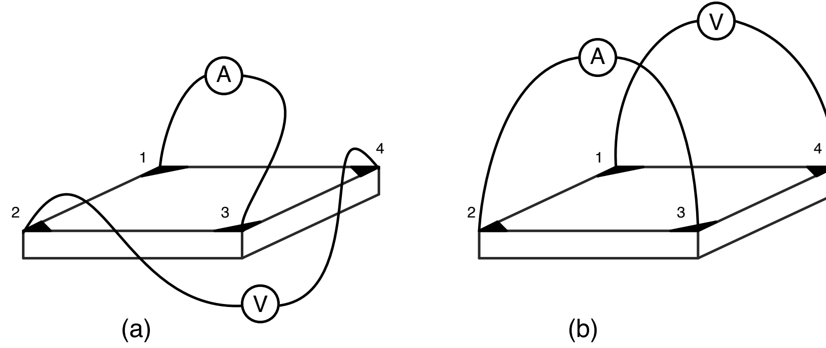

Figure 2.3: Hall effect (a) and resistivity (b) measurements for determining the carrier sheet density, n_s, and the carrier mobility, μ, of a sample.

The mobility of the carriers, μ, can be determined from the relation:

$$\mu = \frac{|V_H|}{R_s I B} \tag{2.7}$$

where R_s is the sheet resistivity of the sample. The sheet resistivity can be determined from the van der Pauw equation:

$$e^{-\pi R_A/R_s} + e^{-\pi R_B/R_s} = 1 \tag{2.8}$$

where R_A and R_B are characteristic resistances of the sample given by $R_A = V_{43}/I_{12}$ and $R_B = V_{14}/I_{23}$ (as shown in part (b) of figure 2.3). From these equations the carrier sheet density and mobility can be determined for any arbitrarily shaped, simply connected sample with four small Ohmic contacts placed on its periphery [48, 49].

Single field Hall effect measurements were performed at room temperature and at 77 K using an Ecopia HMS-3000 Hall Measurement System, using the standard van der Pauw method described above.

Part I

Dilute nitrides of III–Sb materials

Introduction

The growth of high-quality dilute nitride alloys of III–V compounds is inhibited by the small atomic radius and bond-length, and large electronegativity of nitrogen compared to other group-V elements, as can be seen in the periodic table figure shown in the abstract. The anion substitution of nitrogen in place of larger, more electropositive elements results in a high degree of localised strain, limiting the solubility of nitrogen in such materials [50]. The incorporation of nitrogen is achieved by growth at a temperature much lower than the that typically used in growth of the binary. As a result, many point defects are produced degrading the optical and transport properties of the material [51, 52]. Post growth annealing however, has been used to reduce the high unintentional defect density in many dilute nitrides [53–55].

The large bandgap reduction observed when adding small quantities of nitrogen into III–V semiconductor compounds and alloys (discussed in section 1.6) has been most extensively studied in dilute nitride arsenides, while little work on dilute nitride alloys of III–Sb compounds has been reported [15]. Antimony has been mostly used in low [16] and moderate [17] quantities in the alloy Ga(In)NAs to further reduce the bandgap from that of GaAs and to improve the optical quality of the material.

In this introductory chapter the growth and structural characterisation of the dilute nitride GaN_xSb_{1-x} for small inclusions of nitrogen is discussed. High-resolution x-ray diffraction rocking curves around the symmetric 004 Bragg reflection were collected using a Philips X'Pert PRO Materials Research Diffractometer with Cu K_α radiation ($\lambda = 0.15406$ nm). Optical absorption measurements were performed using a Perkin Elmer Spectrum GX FTIR spectrometer in the range 0.1–1.2 eV. Single field Hall measurements were conducted at both room temperature and 77 K using the standard van der Pauw configuration with In-Sn and Pt wire contacts.

Dilute nitride alloys of GaSb were grown at QinetiQ Ltd., Malvern, by plasma-assisted molecular beam epitaxy (MBE). The elements of the host binary (Ga and Sb_4) were supplied using standard effusion cells while the nitrogen was incorporated using an Oxford Applied Research HD25 radio frequency (RF) plasma source. The temperature of the substrate during growth was monitored using a thermocouple calibrated using the known

(1×5) to (1×3) surface reconstruction temperature for GaSb under an Sb flux [56]. The GaNSb samples consistently exhibited a clear, streaky (1×3) reconstruction pattern, indicating the desired two-dimensional growth.

The output of the plasma source was investigated by optical emission spectroscopy as a function of chamber pressure (proportional to nitrogen flow rate) and RF plasma power, to maximise the atomic to molecular/ionic nitrogen ratio. The optimum chamber pressure was found to be $\sim 2.5 \times 10^{-6}$ mbar, while the effect of plasma power had little effect on the ratio.

Thin films of GaNSb (nominally 250 nm) were grown on GaSb(001) substrates for structural characterisation while thicker samples (nominally 2 μm) were grown on semi-insulating GaAs(001) for electrical and optical characterisation. The use of an insulating substrate with a bandgap much larger than that of the epilayer allowed the electrical and optical properties to be investigated without being affected by substrate conduction or absorption.

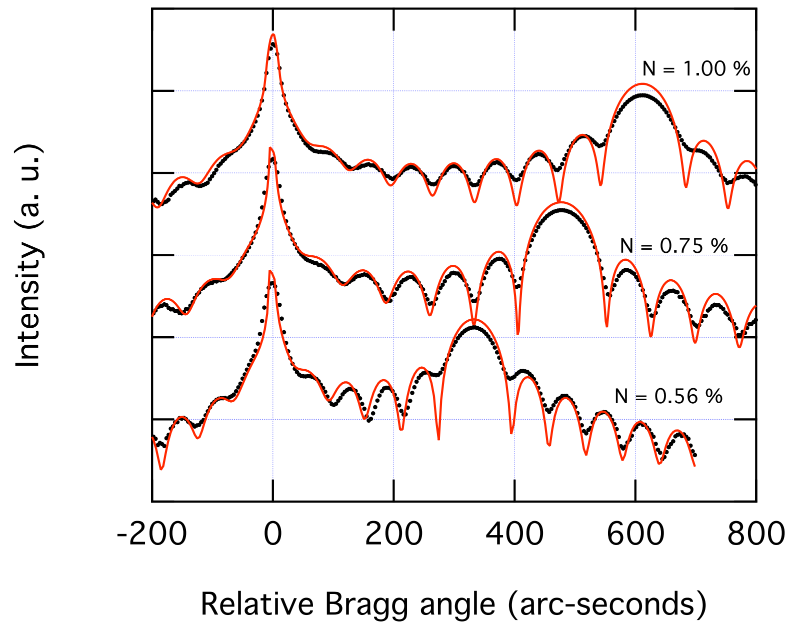

Figure I.1: The 004 rocking curves of three GaNSb layers (black points), the dynamical simulation for each spectrum is shown (red lines) together with the nitrogen incorporation calculated from the simulation.

The XRD rocking curves around the 004 Bragg reflection of three GaNSb/GaSb(001) samples can be seen in figure I.1. The dynamical simulations of the spectra are used

to determine the sample thickness and composition. The nitrogen concentration of each sample is given in the figure. In each spectrum the GaSb(001) substrate peak is centred at zero Bragg angle and the broad peak seen to higher Bragg angles is that of the dilute nitride epilayer. The clearly visible Pendellösung interference fringes allow an accurate determination of the material thickness and composition and are indicative of the high structural quality of the layers.

The degree of nitrogen incorporation was calculated from the experimentally determined lattice constant of the dilute nitride and the lattice constants of the endpoint binary materials GaN and GaSb. The validity of Vegard's law has been shown for the dilute nitride alloy GaNAs from first-principles total-energy calculations where the nitrogen is incorporated substitutionally on the arsenic site [57]. It has also been shown, however, that a small deviation from this linear relationship occurs with increasing nitrogen incorporation (above $\sim$3 per cent nitrogen in GaNAs) and is thought to be due to non-substitutional nitrogen incorporation [58]. In this work, the assumption is made that Vegard's law is valid for the range of nitrogen incorporations considered.

The three rocking curves shown in figure I.1 come from samples with nitrogen incorporations of 0.56, 0.75, and 1.00 per cent, grown at temperatures of 420, 400, and 380 °C respectively. The trend of increasing nitrogen incorporation with decreasing growth temperature, illustrated in figure I.2, is observed in the growth of other dilute nitride alloys [33].

The degree of nitrogen incorporation was found to vary with growth rate, nitrogen plasma power, and growth temperature. The nitrogen incorporation is found to increase with decreasing growth temperature, and with increasing nitrogen plasma power, consistent with other dilute nitride materials [59]. It can be seen in figure I.2, which shows the nitrogen incorporation as a function of growth temperature for a number of GaNSb samples, that the dependence of the incorporation of nitrogen on the plasma power is less pronounced than is seen with growth temperature.

The nitrogen incorporation as a function of growth rate for a number of GaNSb samples is shown in figure I.3, here all samples were grown at 400°C, 400 W plasma power and 2.5×10^{-6} mbar chamber pressure. The growth rate limiting group-III flux of Ga was changed in order to attain different growth rates. In each case the group-V flux of Sb_4

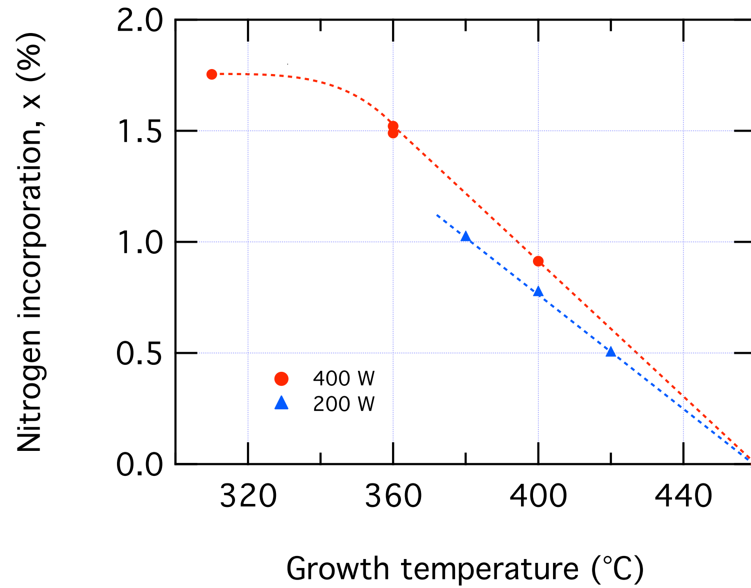

Figure I.2: Nitrogen incorporation as a function of growth temperature for a number of GaNSb samples. The circles (red) and triangles (blue) show samples grown with plasma powers of 400 and 200 Watts, respectively [13].

was changed in order to maintain the optimum V:III ratio of ∼1.5. The behaviour of increasing nitrogen incorporation with increasing growth rate is significantly different from that seen in MBE grown GaInNAs and GaNAs, where the nitrogen incorporation decreases linearly with increasing growth rate [58, 60], consistent with conventional doping of III–V materials [61].

An increase in nitrogen incorporation, together with an improvement in surface morphology, has also been observed in the growth of Ga(In)NAs with the addition of dilute [62], and moderate [17, 63] inclusions of antimony. It is suggested that the large antimony atoms act as a self-surfactant which increases the degree of nitrogen incorporation, similar to that seen in the growth of Ga(In)NAs in the presence of a bismuth flux [64], although in this instance the group-V element is not incorporated into the material.

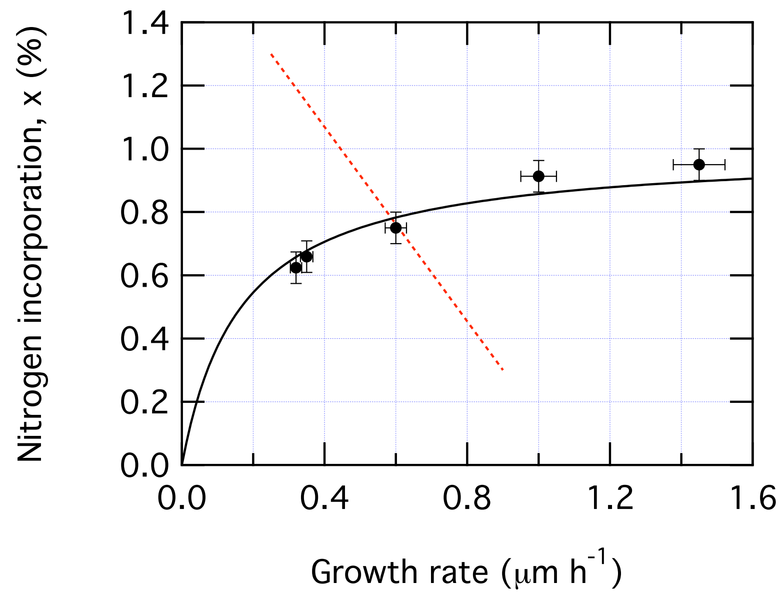

Figure I.3: Nitrogen incorporation as a function of growth rate (black circles) for GaNSb samples grown at 400°C and with fixed nitrogen plasma conditions (400 W, 2.5×10^{-6} mbar chamber pressure), and, for comparison, GaInNAs (dashed line) [60].

Chapter 3

GaNSb optical characterisation

The bandgap reduction due to the incorporation of dilute quanities of nitrogen into gallium antimonide is shown from optical absorption measurements. As well as a reduction in bandgap from that of gallium antimonide, transitions from the valence bands to E_+ are observed and a least squares fitting of the upper branch of the solution of the BAC Hamiltonian is made, giving a coupling parameter for GaNSb of 2.6$\pm$0.1 eV. Finally, a comparison between the BAC model and Lindsay and O'Reilly's 10-band $\mathbf{k}\cdot\mathbf{p}$ model with tight-binding parameters is made, showing good agreement between the two models.

3.1 Introduction

Nitrogen induced bandgap reduction has been observed in many alloys including GaNP [34], GaNAs [5], InNAs [35] and most recently GaNSb [14]. The addition of antimony to the dilute nitride GaNAs has been shown to improve the optical and electronic properties of the material [62] and has been suggested as a possible material for long wavelength optoelectronic devices lattice matched to GaAs [65]. To determine the dependence of the bandgap of such materials as a function of nitrogen incorporation, the band anti-crossing (BAC) model parameters of the constituent endpoint ternaries must be known. Though these have been well investigated in GaNAs there is little data for GaNSb, a fact highlighted in a review on nitrogen containing III–V materials by Vurgaftman and Meyer [2].

In this chapter, infrared absorption measurements of GaNSb samples with nitrogen incorporations between 0.2 and 1.0 per cent are presented and a value for the coupling parameter, $C_{MN}(= V_{MN}\sqrt{x})$, for GaNSb is determined. The dispersion of the non-parabolic conduction bands of the material are also compared to the predictions of the 10-band modified $\mathbf{k} \cdot \mathbf{p}$ Hamiltonian of Lindsay and O'Reilly, using their preliminary values for GaNSb.

3.2 Experimental details

Gallium nitride antimonide samples were grown by RF plasma-assisted molecular beam epitaxy on two different substrates. Samples ∼250 nm thick were grown on GaSb(001) substrates for structural characterisation and thicker samples, ∼2 μm, were grown on semi-insulating GaAs(001) substrates, allowing Hall and transmission geometry optical absorption of the epilayer to be performed. Further information on the growth and structural characterisation of the samples can be found in the introduction to this part of the thesis.

3.3 Absorption simulation

The absorption coefficient, α, is defined as the ratio of the energy removed from an incident beam of electromagnetic radiation per unit time and volume to the incident flux.

$$\alpha = \hbar\omega \times \frac{\text{number of transitions per unit volume and time}}{\text{incident flux}} \tag{3.1}$$

The number of transitions per unit time (W) from an initial state $|i\rangle$ to a final state $|f\rangle$ is given by Fermi's "Golden rule":

$$W = \frac{2\pi}{\hbar}|\langle f|\mathrm{H}_I|i\rangle|^2\delta(E_f - E_i - \hbar\omega) \tag{3.2}$$

where H_I is the interaction Hamiltonian between the incident electromagnetic radiation and the electrons of the target material and the δ-function ensures the conservation of energy for the interaction. If the initial and final states of a transition are two Bloch states, then conservation of quasi-momentum gives:

$$W \propto \frac{2\pi}{\hbar}|\mathbf{P}_{fi}|^2\delta(E_f(\mathbf{k}_f) - E_i(\mathbf{k}_i) - \hbar\omega)\delta_{\mathbf{k}_i+\mathbf{q},\mathbf{k}_f} \tag{3.3}$$

Here, $\mathbf{P}_{fi}$ is the momentum matrix element describing the transition for one primative unit cell and $\mathbf{q}$ is the wavevector of the incident radiation. The photon momentum, $\hbar\mathbf{q}$, is usually much smaller than the momenta of the initial and final electron states and therefore $\delta_{\mathbf{k}_i+\mathbf{q},\mathbf{k}_f} \simeq \delta_{\mathbf{k}_i,\mathbf{k}_f}$. Summing over all the initial and final quasi-momenta, the total transition rate can then be written as:

$$W \propto \frac{2\pi}{\hbar}\sum_{\mathbf{k}}|\mathbf{P}_{fi}|^2\delta(E_f(\mathbf{k}) - E_i(\mathbf{k}) - \hbar\omega) \tag{3.4}$$

where $\mathbf{k} = \mathbf{k}_i = \mathbf{k}_f$. Transitions arising solely from excitations by electromagnetic waves, where the photon momentum is small compared to that of the electron momenta, will be vertical in k-space, and are therefore can only be direct transitions.

Replacing the summation over $\mathbf{k}$ by an integral and assuming that the matrix element is independent of $\mathbf{k}$ (usually given an average value) and finally that the valence band is fully occupied and the conduction band is empty, the transition rate is given by:

$$W \propto \frac{2\pi}{\hbar}|P_{cv}|^2\int\delta(E_f(\mathbf{k}) - E_i(\mathbf{k}) - \hbar\omega)\mathrm{d}^3\mathbf{k} \tag{3.5}$$

where the integral describes the joint density of states between the valence band and the conduction band.

The incident flux of the electromagnetic radiation is given by the product of the energy density and the incident velocity. The cycle averaged energy density is $\frac{1}{2}\epsilon\omega^2 A_0^2$, where ϵ is the permittivity, ω the angular frequency of the wave, and A_0 the vector potential. The incident velocity is given by c/n where c the velocity of light and n is the refractive index. Using equation 3.1, the absorption coefficient can be written:

$$\alpha(E) \propto \sum_{c,v} \frac{|P_{cv}|^2 g_{cv}(E)}{\hbar\omega} \tag{3.6}$$

where $g_{cv}(E)$ is the joint density of states, P_{cv} is the momentum matrix element and $\hbar\omega$ is the energy of the incident radiation. The momentum matrix element describes the transition between a valence band, v, and conduction band, c, i.e. $P_{cv} = \langle c|\hat{\mathbf{p}}|v\rangle$, where $|v\rangle$ represents the valence band states, $|c\rangle$ represents the conduction band states and $\hat{\mathbf{p}}$ is the momentum operator.

The summation in equation 3.6 is over all allowed conduction and valence bands. For dilute nitride alloys of III–V compounds, the conduction band is made up of $|+\rangle$ and $|-\rangle$ states representing the E_+ and E_- energy levels.

The non-parabolic sub-bands produced by the incorporation of nitrogen into the host GaSb can be treated as a simple two state system (section 1.6.2), making the assumption that the nitrogen levels form a narrow band highly localised at the Γ-point. The hybridised band resulting from the interaction between the conduction band states and the nitrogen states, has the form:

$$|\psi_{\mathbf{k}}\rangle = a_{c\mathbf{k}}|c\mathbf{k}\rangle + a_{N\mathbf{k}}|N\mathbf{k}\rangle \tag{3.7}$$

The time-independent Schrödinger equation for this two state system then reduces to the secular equation:

$$\begin{bmatrix} E_{c\mathbf{k}} & V_{\mathbf{k}N} \\ V_{N\mathbf{k}} & E_N \end{bmatrix} \begin{bmatrix} a_{c\mathbf{k}} \\ a_{N\mathbf{k}} \end{bmatrix} = E \begin{bmatrix} a_{c\mathbf{k}} \\ a_{N\mathbf{k}} \end{bmatrix} \tag{3.8}$$

If transitions between valence band states and nitrogen states are neglected, i.e. $\langle N|\hat{\mathbf{p}}|v\rangle = 0$, then the matrix elements for the optical transitions become:

$$\begin{aligned} P_{\mathbf{k}} &= \langle v\mathbf{k}|\hat{\mathbf{p}}|\psi_{\mathbf{k}}\rangle \\ &= a_{c\mathbf{k}}\langle v\mathbf{k}|\hat{\mathbf{p}}|c\mathbf{k}\rangle \end{aligned} \tag{3.9}$$

Solving equation 3.8 gives:

$$E_{\pm} = \frac{1}{2}(E_{c\mathbf{k}} - E_N)^2 \pm \frac{1}{2}\left\{(E_{c\mathbf{k}} - E_N)^2 + |V_{\mathbf{k}N}|^2\right\}^{\frac{1}{2}} \tag{3.10}$$

$$\text{and} \quad a_{c\mathbf{k}}^{\pm} = \frac{V_{\mathbf{k}N}}{\{(E_{\pm} - E_{c\mathbf{k}})^2 + |V_{\mathbf{k}N}|^2\}^{\frac{1}{2}}} \tag{3.11}$$

where $|a_{c\mathbf{k}}|^2 + |a_{N\mathbf{k}}|^2 = 1$ has been used. Hence,

$$|P_{\pm}|^2 = \frac{|V_{\mathbf{k}N}|^2}{(E_{\pm} - E_{c\mathbf{k}})^2 + |V_{\mathbf{k}N}|^2} |P_{cv}|^2 \tag{3.12}$$

and the absorption coefficient, equation 3.13, is reduced by the first factor on the right hand side of equation 3.12:

$$\alpha(E) \propto (|a_{c\mathbf{k}}^{+}|^2 + |a_{c\mathbf{k}}^{-}|^2) \sum_{c,v} \frac{|P_{cv}|^2 g_{cv}(E)}{\hbar\omega} \tag{3.13}$$

3.4 Results and discussion

The infrared absorption spectra of four GaNSb samples with nitrogen incorporations between 0.2 and 0.6 per cent are shown in figure 3.2; the spectra are offset in the y-direction for clarity. The feature seen in the region 0.40–0.45 eV is attributed to optical transitions from the valence band to E_- states and the feature seen in the region 0.8–0.9 eV is attributed to transitions from the valence band to E_+ states. The divergence of these features can be seen with increasing nitrogen concentration consistent with the BAC model.

The infrared absorption spectra were simulated using the method reported by Perlin *et al.* [66], based on the calculation of the joint density of states for each electronic transition within the defined material bandstructure, and utilising the BAC matrix element defined in section 3.3. The bandstructure of GaNSb used for the absorption calculation is shown in figure 3.3. The valence bands were calculated using Pidgeon and Brown's 8-band $\mathbf{k} \cdot \mathbf{p}$ Hamiltonian [32] with an experimentally determined bandgap for GaSb of 0.71 eV (figure 3.1) and further band parameters taken from the literature [1]. The conduction bands were calculated using the BAC equation 3.10, and using the non-parabolic host conduction band obtained from the 8-band $\mathbf{k} \cdot \mathbf{p}$ calculation.

The joint density of states for each transition was calculated from the numerical differentiation of the appropriate bands from the 8-band $\mathbf{k} \cdot \mathbf{p}$ and BAC model bandstructures. The absorption was then determined, using equation 3.13, for each of the transitions from the valence bands to the E_- and E_+ states. A sum of the six absorption contributions gives the total absorption for the material, with the momentum matrix element $|P_{cv}|^2$

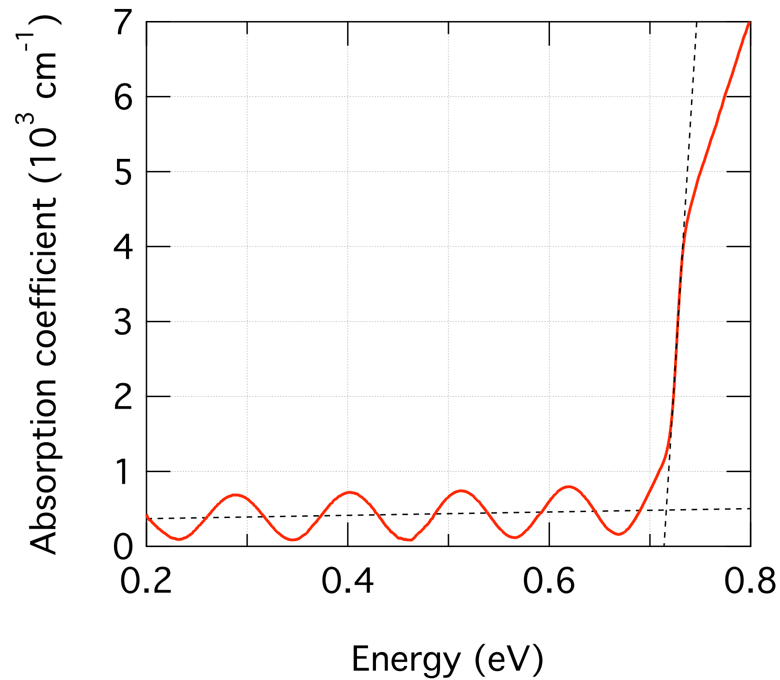

Figure 3.1: Infrared absorption spectrum of GaSb grown epitaxially on a GaAs substrate. The nominal thickness of the layer from growth conditions was 150 nm. The absorption edge was determined to be 0.71 eV.

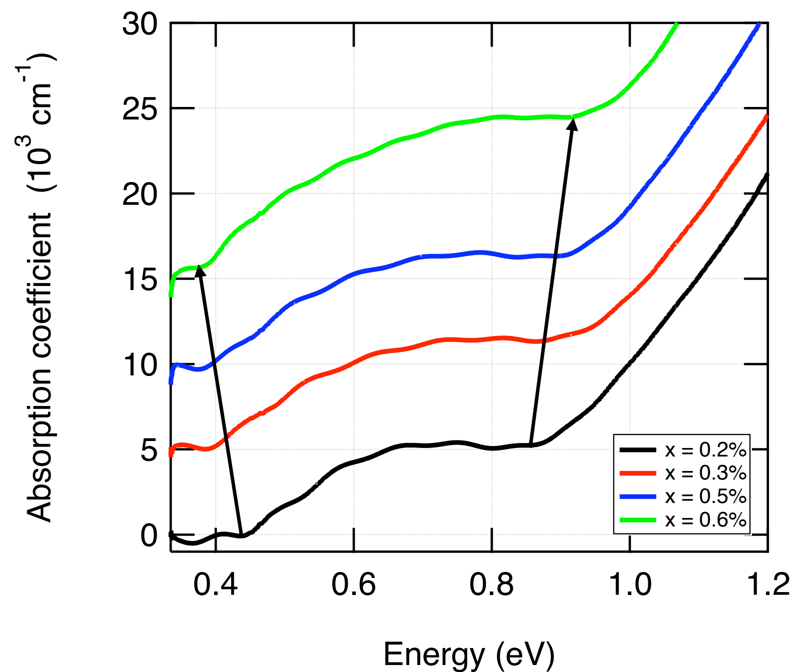

Figure 3.2: Infrared absorption spectra of GaNSb layers with nitrogen incorporations between 0.2 and 0.6 per cent are shown. Each spectrum is offset by 5000 cm^{-1} in the y-direction. The arrows are a guide to the eye to highlight the divergence of the features attributed to transitions from the valence band to E_- and E_+.

used as a free parameter with which to fit the experimental data. The absorption of a GaNSb sample with 0.6 per cent nitrogen (circles) can be seen in figure 3.4 together with the absorption components from the light (dot-dashed) and heavy (dashed) hole valence bands to (a) the E_- and (b) E_+ states. In addition, the total calculated absorption is shown (solid line).

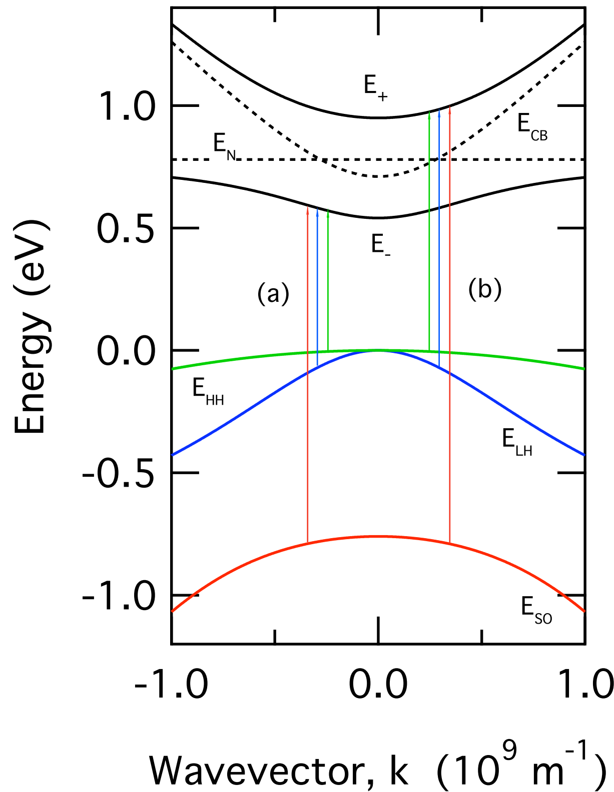

Figure 3.3: The calculated bandstructure of GaNSb used for the absorption simulation. The three valence bands (light hole, heavy hole and spin-orbit split-off bands) were calculated using the 8-band $\mathbf{k} \cdot \mathbf{p}$ Hamiltonian of Pidgeon and Brown, and the conduction bands using the band anticrossing model with $C_{MN} = 2.6$ eV and $E_N = 0.78$ eV. The optical transitions that contribute to the absorption are also shown (coloured arrows).

The pronounced nature of the valence band to E_+ transition seen in the infrared absorption spectrum of GaNSb in figure 3.4 is a consequence of the large spin-orbit splitting of the host material. The transition from the spin-orbit band to E_- occurs close to 1.4 eV, an energy somewhat greater than that of the transitions from the light and heavy hole valence bands to E_+, which occurs at $\sim$1.0 eV. This is not the case for GaNAs where the transitions from the light and heavy hole valence bands to E_+ occurs close to 1.8 eV, and is considerably masked by the spin-orbit to E_- transition beginning around 1.55 eV [66].

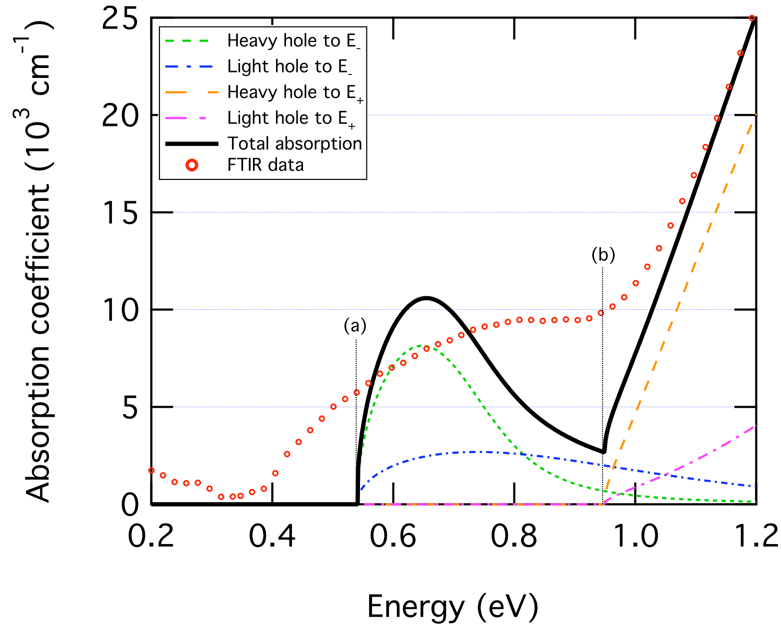

Figure 3.4: The infrared absorption spectrum (circles) of $GaN_xSb_{1-x}/GaAs$ with $x = 0.006$ together with the constituent components (dashed and dot-dashed lines representing heavy and light hole bands to (a) E_- and (b) E_+ bands respectively) and the sum total (solid line) of the absorption simulation.

Room temperature single field Hall analysis of the samples revealed degenerate p-type carrier concentrations in the range 3–6$\times10^{18}$ cm^{-3}. The cause of the high carrier concentrations seen in the samples investigated is thought to be due to the high level of native acceptor defects found in GaSb [67] enhanced by a large dislocation density due to the lattice mismatched growth of the nitride layer on the GaAs substrate and by the incorporation of nitrogen. A bandgap narrowing resulting from the high carrier concentrations was included in the bandstructure with a 35 meV increase in the valence band with respect to the conduction band and nitrogen level [68].

In addition to a small narrowing of the bandgap, localised deformations in potential surrounding the high quantity of native acceptor defects will act to smear both the conduction band (in our case E_-) and valence band edges. The valence band edge is unaffected by this as the perturbed part of the valence band is found above the Fermi level [44, 69]. For the E_- level, however, the formation of tail states into the bandgap results in a non-zero absorption below the expected valence band to E_- transition. As the E_+ level is predominantly nitrogen-like at the Γ-point [39], the position of the valence band to E_+ transition remains unaffected by this and acts as a good reference point with which to determine the

band parameters of the BAC model.

The position of the transitions from the degenerate valence bands to E_- and E_+ were determined from the infrared absorption spectra of samples with nitrogen incorporations between 0.2 and 1.0 per cent. The errors were estimated to be ± 20 meV for valence band to E_+ transitions and ± 0.03% in the nitrogen incorporation. Determination of the accuracy of the valence band to E_- transitions is not possible without further investigation into the effects of the high carrier concentration and has been conservatively estimated at ± 50 meV for illustrative purposes.

The experimentally determined positions of the transitions from the degenerate valence bands to the E_- and E_+ bands are shown in figure 3.5, together with a fitting of the BAC model, and the dispersion of the valence band to the E_- and E_+ transitions predicted by Lindsay and O'Reilly's 10-band modified $\mathbf{k} \cdot \mathbf{p}$ Hamiltonian.

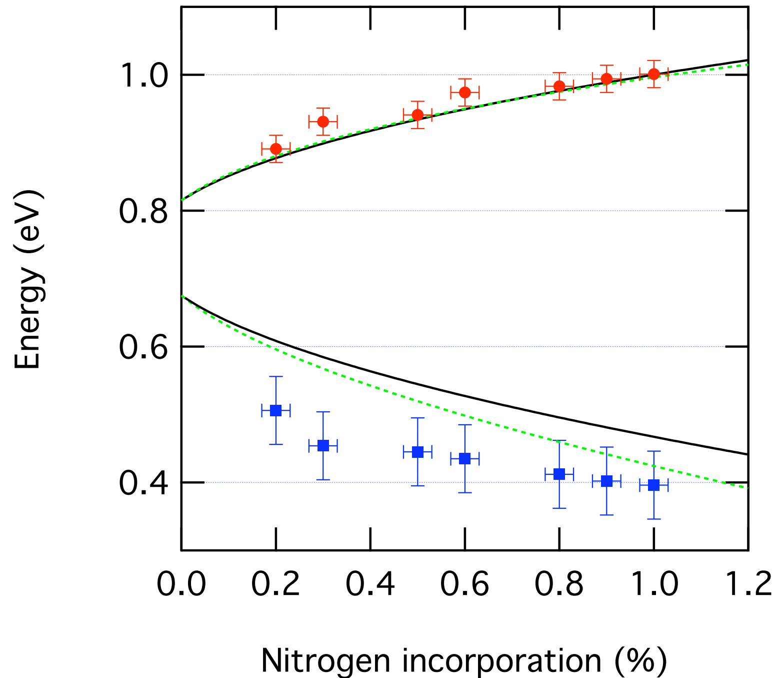

Figure 3.5: The position of the valence band to (i) E_- (filled squares and bars) and (ii) E_+ (filled circles and bars) transitions together with a fitting based on the band anticrossing model (solid lines) with a nitrogen level of 0.78 eV and a C_{MN} value of 2.6 eV and a 10-band $\mathbf{k} \cdot \mathbf{p}$ simulation using parameters taken from tight binding calculations by Lindsay and O'Reilly (dashed lines).

The BAC model dispersion of the E_+ transition was determined from a least squares fitting

of the positive root of equation 1.18 to the E_+ transition data with the coupling constant, C_{MN}, as the fitting parameter. The energy of the nitrogen level used was 0.78 eV above the VBM, as determined by Lindsay and O'Reilly from their preliminary tight-binding calculations of GaNSb [38]. From this fitting, the coupling parameter, C_{MN}, for GaNSb was found to be 2.6±0.1 eV.

The dispersion of the E_+ band given by one of the solutions of the 10-band modified $\mathbf{k}\cdot\mathbf{p}$ Hamiltonian is shown as a comparison to the BAC model. The values of the constants α, β, γ and E_N of the Hamiltonian were 2.34, 2.80, 2.30 and 0.78 eV respectively, as determined from preliminary tight binding calculations of GaNSb by Lindsay and O'Reilly [38].

It can be seen that both models give a good description of the E_+ dispersion with nitrogen incorporation, and that the valence band to E_- transitions occur at lower energies than is predicted from both models. This is consistent with the expected tailing of the conduction band into the bandgap due to the high quantity of ionised impurities in the material. Finally, it can be seen that the E_- level given by the 10-band $\mathbf{k}\cdot\mathbf{p}$ model decreases more rapidly with nitrogen incorporation than for the BAC model. This is due to the γ term in equation 1.19 which acts to describe the effects of N–N pairs and cluster states by reducing the energy of the nitrogen level to reflect the average energy of all of the nitrogen complexes present in the material.

3.5 Conclusions

The incorporation of dilute quantities of nitrogen into gallium antimonide has been shown to reduce the bandgap of the material from that of the binary host consistent with the BAC model. Simulations of infrared absorption spectra, based on a joint density of states method, have indicated a prominent valence band to E_+ feature. The BAC coupling parameter of GaNSb was determined to be 2.6±0.1 eV from a least squares fitting of the valence band to E_+ transition using a nitrogen level of 0.78 eV.

Finally, the positions of the transitions from the valence bands to the E_+ level were shown to be in good agreement with those predicted from Lindsay and O'Reilly's 10-band modified $\mathbf{k}\cdot\mathbf{p}$ Hamiltonian and preliminary tight-binding parameters for GaNSb.

Chapter 4

InNSb optical characterisation

The bandgap reduction in dilute nitride alloys of indium antimonide may be inferred from infrared absorption measurements. Though the measurements show an increase in the energy of the absorption edge of the samples compared to that of pure indium antimonide, the increased carrier concentration resulting from the nitrogen incorporation is shown to cause this increase, masking the reduction in the bandgap of the material. The absorption edge of the samples is calculated using 10-band $\mathbf{k} \cdot \mathbf{p}$ calculations, and the effects of Moss-Burstein band-filling and bandgap renormalisation are included through Fermi-Dirac statistics calculations.

4.1 Introduction

The incorporation of small quantities of nitrogen into indium antimonide, reducing the bandgap of the material below its intrinsic room temperature value of ∼180 meV (≈ 7μm), would enable the exploitation of the atmospheric transmission window between 8 and 14 μm (≈ 155 and 90 meV).

The predicted bandgap as a function of nitrogen incorporation of InNSb is shown in figure 4.1. The bandgap was determined from 10-band $\mathbf{k} \cdot \mathbf{p}$ bandstructure calculations, previously discussed in section 1.6.3, together with preliminary parameters based on tight-binding calculations by Lindsay and O'Reilly [38]. In addition, the calculated transmission of electromagnetic radiation through the earth's atmosphere is shown as a function of wavelength [70]. It can be seen from these calculations that less than 1 per cent nitrogen incorporation into InSb could be used to span the entire atmospheric transmission window between 8 and 14 μm.

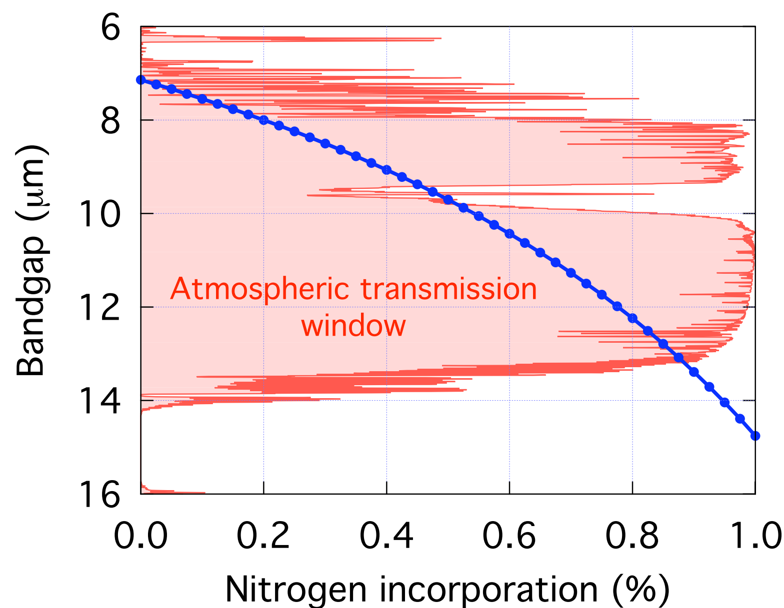

Figure 4.1: The calculated bandgap as a function of nitrogen incorporation of InNSb, shown together with the atmospheric transmission window found between 8 and 14 μm [70], illustrating the suitability of the material for optoelectronic devices operating in this wavelength range.

In this chapter, the reduction in the bandgap of InNSb from that of InSb is inferred

from infrared absorption measurements. The absorption edges of the nitrogen containing samples are, however, shown to *increase* in energy from that of intrinsic InSb. This increase is believed to be due to the increased free-carrier concentration in the nitrogen containing samples, giving rise to the effects of Moss-Burstein band-filling and bandgap renormalisation.

4.2 Experimental details

Indium nitride antimonide samples were grown by RF plasma-assisted molecular beam epitaxy on InSb(001) substrates miscut by 2° towards (111)B for structural characterisation, and on GaAs(001) substrates for optical and electrical characterisation. As with the GaNSb samples, the thickness of the samples for structural characterisation was nominally 200 nm, and those for optical characterisation ∼2 μm. Further information on the growth and structural characterisation of the samples can be found in the introduction to this part of the thesis.

4.3 Theoretical background

The high n-type carrier concentration observed in InNSb samples gives rise to two effects which alter the optical properties observed in the samples. These effects and their treatment in our calculations are outlined below.

4.3.1 Moss-Burstein band filling

The lowest energy optical transition that can take place in a semiconductor is from the highest occupied electron state, to the lowest unoccupied electron state. For a semiconductor that is not degenerately doped, i.e. the Fermi energy is within the bandgap, this transition will be from the VBM to the CBM (neglecting the effects of thermal excitation across the bandgap) as illustrated in 4.2(a). If the semiconductor is degenerately doped however, as is the case in InNSb, then the lowest unoccupied electron state is found close to the Fermi energy, which is situated within the conduction band 4.2(b).

The increase in energy of the absorption cut-off with increasing carrier concentration was first observed in InSb, whose small bandgap and conduction band effective mass lead to a low degeneracy concentration, i.e. $n(E_F = E_g) \approx 3 \times 10^{16}$ cm^{-3} and a Fermi energy that increases rapidly with increasing carrier concentration. This observation was interpreted contemporaneously by T.S. Moss and E. Burstein and as such is often referred to as Moss-Burstein band-filling [71, 72].

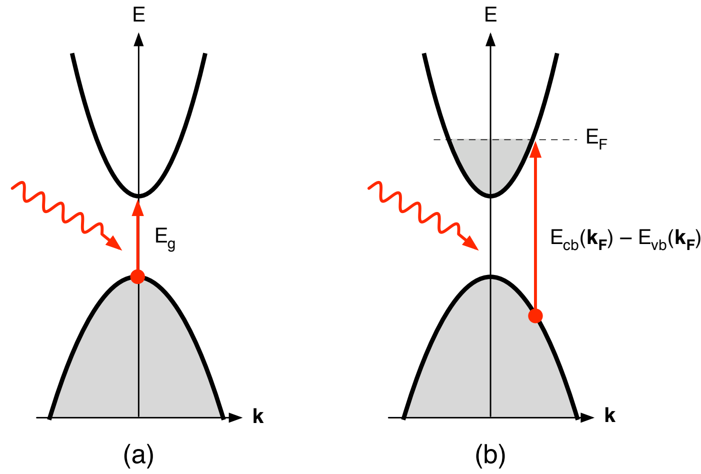

Figure 4.2: A schematic representation of Moss-Burstein band filling, (a) the absorption cut-off in a non-degenerate semiconductor is equal the energy of its bandgap and (b) a degenerate semicondutor's absorption cut-off is equal to a vertical transition from the valence band into the conduction band near the Fermi-level.

In modelling the Moss-Burstein band filling a number of assumptions are made. It is assumed that only direct band-to-band transitions will take place in the absorption process, i.e. phonon-assisted transitions are neglected. It is also assumed that the lowest unoccupied energy level in the material is situated at the Fermi energy, E_F. In reality, at finite temperatures, the lowest unoccupied electron state will be below E_F, due to the thermal excitation of electrons across the Fermi energy [28]. Finally, it is assumed that the valence band is non-dispersive over the wavevector range of interest, an accurate assumption for the heavy hole valence band in all materials considered in this work. The final assumption makes the determination of ΔE_{mb} more convenient, as $E_{vb}(\mathbf{k_F}) = 0$, and is therefore equal to $E_F - E_g$, where the Fermi energy is referenced to the valence band maximum.

The absorption cut-off energy is then determined from calculating the carrier concentration

as a function of Fermi energy using the relation:

$$n(E_F) = \int_{E_g}^{\infty} g(\varepsilon) f(\varepsilon, E_F) \mathrm{d}\varepsilon \tag{4.1}$$

where $g(\varepsilon)$ is the conduction band density of states and $f(\varepsilon, E_F)$ is the Fermi-Dirac probability distribution given by:

$$f(\varepsilon, E_F) = \frac{1}{e^{\varepsilon - E_F/k_B T} + 1} \tag{4.2}$$

The conduction band density of states, $g(\varepsilon)$, is determined from the derivative of the conduction band dispersion which can be calculated by any of the methods outlined in section 1.5.

The calculated absorption cut-off for InSb is shown as a function of carrier concentration in figure 4.3, where the InSb bandstructure was calculated using the Pidgeon and Brown 8-band $\mathbf{k} \cdot \mathbf{p}$ Hamiltonian. Here, the calculated degeneracy concentration of 3×10^{16} cm^{-3} is in good agreement with experiment [71].

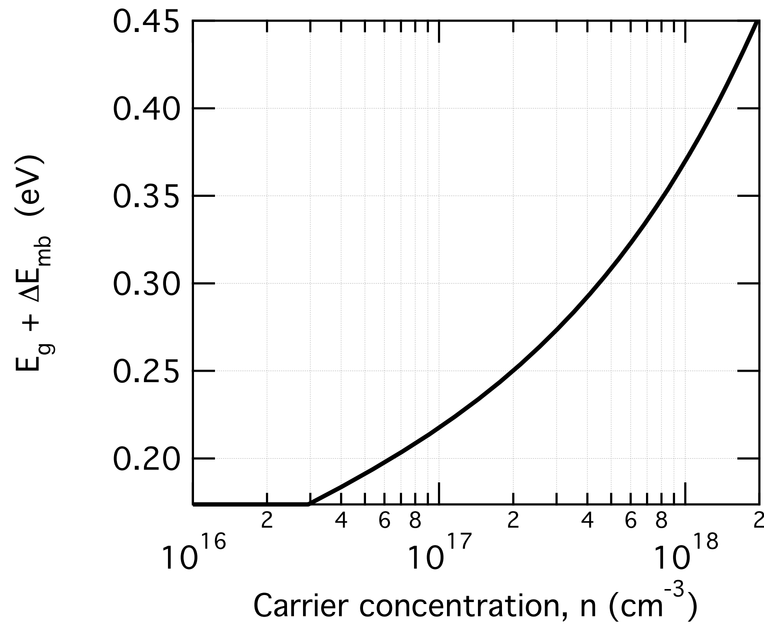

Figure 4.3: The minimum optical transition as a function of carrier concentration for InSb at 300 K, calculated using the Pidgeon and Brown 8-band $\mathbf{k} \cdot \mathbf{p}$ bandstructure and assuming the lowest available conduction band state is situated at the Fermi energy.

4.3.2 Bandgap renormalisation

The second, and less pronounced effect is that of bandgap renormalisation. Here, electron-electron, and electron-impurity interactions act to redistribute the states close to the band extrema, reducing the bandgap of the material, as illustrated schematically in figure 4.4.

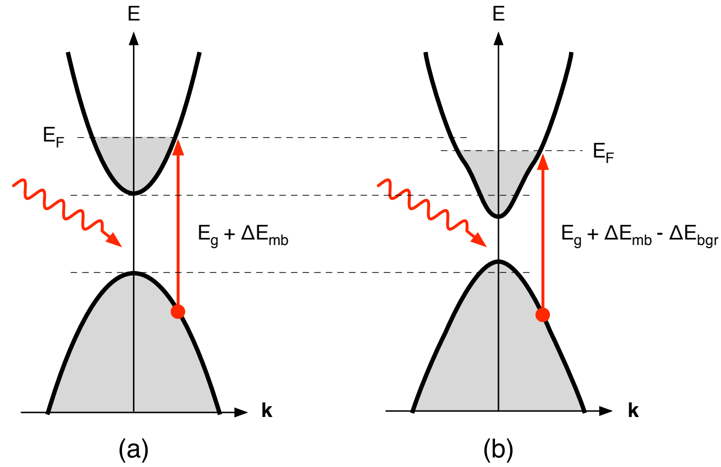

Figure 4.4: A schematic representation of bandgap renormalisation, (a) shows the Moss-Burstein band-filling and (b) shows the redistribution of electron states due to the electron-electron and electron-ion screening of the conduction and valence band.

The degree of bandgap shrinkage resulting from the degeneracy of a material is calculated using the method of Berggren and Sernelius [73]. The reduction in bandgap due to the electron-electron interactions is calculated from:

$$\Delta E_{e-e} = -\frac{2e^2 k_F}{\pi \varepsilon_s} - \frac{e^2 k_{TF}}{2\varepsilon_s}\left[1 - \frac{4}{\pi}\arctan\left(\frac{k_F}{k_{TF}}\right)\right] \tag{4.3}$$

where k_F is the Fermi wavevector and k_{TF} is the Thomas-Fermi screening wavevector, given by $(2/\sqrt{\pi})(k_F/a_B)^{1/2}$. Here, a_B is the Bohr radius in units of Ångströms given by $0.53\varepsilon_s m_0/m^*$.

The contribution to the redistribution of states due to the interaction between electrons and impurity ions is given by:

$$\Delta E_{e-i} = -\frac{4\pi e^2 n}{\varepsilon_s a_B k_{TF}^3} \tag{4.4}$$

In each case, the degree of bandgap shrinkage is dependent on the Fermi wavevector which, in turn is dependent on the carrier concentration of the material.

4.4 Results and discussion

The α^2 absorption spectra as a function of excitation energy are shown for two InNSb samples in figure 4.5. The samples were grown to a thickness of 2 μm on GaAs substrates as described in section 4.2. For comparison, the absorption spectrum of an InSb sample, of thickness 2.2 μm also grown on GaAs, is shown in the figure. The nitrogen incorporations of the two InNSb samples are 0.51 and 0.68 per cent, with carrier concentrations of 2.05×10^{18} and 2.30×10^{18} cm^{-3} respectively, as obtained from single field Hall measurements. The carrier concentration of the InSb sample was $\sim2\times10^{16}$ cm^{-3}.

It can be seen from figure 4.5 that the absorption edge of the InSb sample is close to 180 meV, the energy of the room temperature InSb bandgap, and that the two nitrogen containing samples have higher energy absorption edges of around 310 and 330 meV.

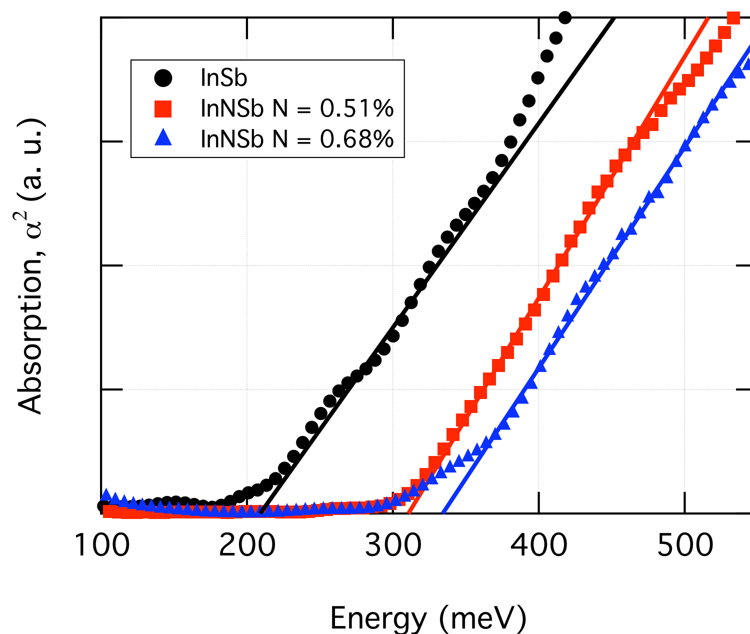

Figure 4.5: The FTIR absorption spectra of an InSb and two InNSb epilayers grown to a thickness of 2 μm on GaAs substrates. The absorption spectrum of the InSb (circles) sample shows the fundamental absorption occurring close to 180 meV – consistent with the bandgap of InSb. The InNSb samples show absorption edges at around 310 meV and 330 meV for the 0.51 and 0.68 per cent nitrogen samples respectively.

As expected, the absorption edges of the InNSb samples are higher than predicted from the bandgap calculations illustrated in figure 4.1, due to the effects of Moss-Burstein band-filling and bandgap renormalisation discussed above.

The results of the calculations of the bandgap reduction due to (i) the nitrogen incorporation, E_g, and (ii) the bandgap renormalisation, ΔE_{bgr}, together with the absorption edge enhancement due to Moss-Burstein band-filling, ΔE_{mb}, are summarised in table 4.1. Also included, is the calculated absorption edge energy, given by $E_\alpha = E_g - \Delta E_{bgr} + \Delta E_{mb}$, and the corresponding experimental values.

Table 4.1: Summary of calculated and experimental results. The nitrogen incorporation is given as a percentage, while the nitrogen-induced reduced bandgap, E_g, the bandgap renormalisation, ΔE_{bgr}, the Moss-Burstein absorption edge enhancement, ΔE_{mb}, and the calculated and experimentally determined values of the absorption edge, E_α, are given in meV.

Nitrogen (%)	E_g (meV)	ΔE_{bgr}	ΔE_{mb}	E_α calc.	E_α expt.
0.51	128	20	222	330	310
0.68	112	20	240	332	330

Good agreement can be seen between the calculated and experimentally determined values of the absorption edge of the two InNSb samples, from this it can be inferred that the bandgap of the material is reduced by the incorporation of nitrogen, however, the effect is concealed by the effects resulting from the increased carrier concentration in the nitrogen containing samples.

4.5 Conclusion

Infrared absorption spectra and Hall analysis of epitaxially grown InNSb indicate a high degree of Moss-Burstein band-filling resulting in an absorption edge higher in energy than that of pure InSb. By quantifying the effects of Moss-Burstein band-filling and bandgap renormalisation it was inferred that a reduction in bandgap due to the incorporation of nitrogen into the samples was consistent with the data. Though a large portion of the 8–14 μm optical transmission window has been shown to be attainable at room temperature with InNSb (0.68 per cent nitrogen corresponds to a wavelength of $\sim$11.1 μm), in order to utilise this fundamentally narrow bandgap material, the free carrier concentration must first be dramatically reduced.

Chapter 5

GaInNSb lattice matching

The ability to tune the bandgap and lattice constant of the dilute nitride alloy $Ga_{1-y}In_yN_xSb_{1-x}$, by varying the degree of indium and nitrogen incorporation during growth, is demonstrated. High-resolution x-ray diffraction rocking curves and reciprocal space maps are used to determine the degree of indium and nitrogen incorporation, and to demonstrate the lattice matching of the quaternary alloy with its host binary, GaSb. Simulations of the lattice constant and bandgap as a function of nitrogen incorporation show good ageement with experimental data for the samples produced.

5.1 Introduction

The incorporation of nitrogen and indium into the III–V binary compound gallium arsenide has been extensively studied and used to tailor the bandgap and lattice constant for devices, allowing them to operate in the technologically important 1.3–1.55 μm (940–800 meV) wavelength range [8, 74–77]. A marked degradation in the optical quality of the material with increasing nitrogen concentration, however, makes it an unsuitable material for longer wavelength applications e.g. molecular detection and exploitation of the atmospheric transmission windows of 3–5 μm (415–250 meV) and 8–14 μm (155–90 meV).

The group III–antimonide alloys of gallium and indium have received much less attention, but show great promise for long-wavelength infrared applications due to their small intrinsic bandgaps which, with the incorporation of nitrogen, can be further reduced [13, 15, 78].

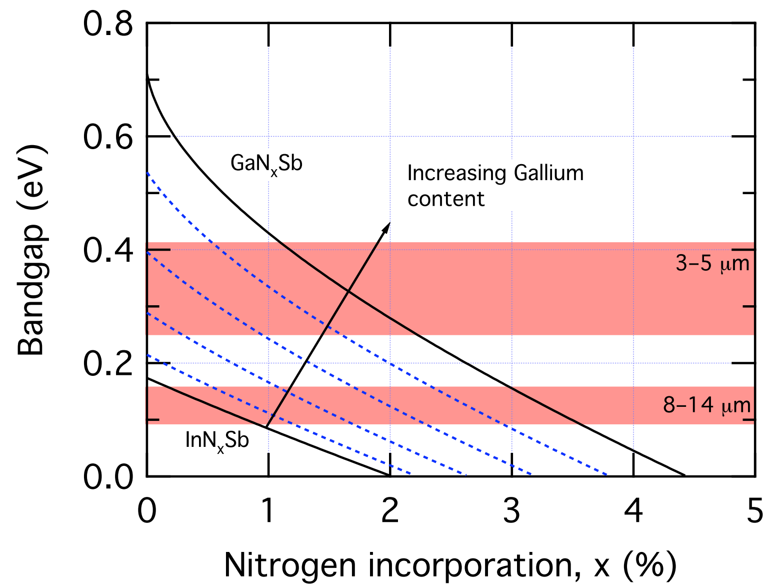

Figure 5.1: The calculated bandgap as a function of nitrogen incorporation for GaInNSb alloys, shown together with the atmospheric transmission windows of 3–5 and 8–14 μm. The dashed lines represent 20 per cent increments in gallium concentration away from InNSb and the solid lines represent the endpoint ternary alloys. The bandgap dispersion was calculated using the 10-band $\mathbf{k} \cdot \mathbf{p}$ Hamiltonian described in section 1.6.3 with parameters from tight-binding calculations [38, 79].

The calculated bandgap variation as a function of nitrogen incorporation for InNSb and GaNSb can be seen in figure 5.1. Here, the solid lines represent the ternary endpoints

of the material and the intermediate dashed lines represent 20 per cent changes in cation concentration. The atmospheric transmission windows of 3–5 and 8–14 μm are also shown, highlighting the applicability of this material system to long wavelength device applications.

As with GaInNAs grown on GaAs, dilute nitride alloys of GaInSb can be lattice matched to GaSb, or, for higher electron confinement, to alloys of GaAlSb, with only moderate inclusions of indium and nitrogen. In addition, growing GaInNSb samples lattice matched to their GaSb substrates allows the properties of the material to be investigated without the complications introduced by strain within the epilayer, e.g. strain induced dislocations.

In this chapter, the structural characterisation of GaInNSb epilayers, lattice matched to GaSb(001) substrates, is presented. An intermediate GaInSb layer is used in conjunction with high resolution x-ray diffraction (XRD) measurements to determine the degree of nitrogen and indium incorporation within the quaternary alloys.

5.2 Experimental details

The GaInNSb samples were grown by RF plasma-assisted molecular beam epitaxy. Each of the samples were grown on GaSb(001) substrates and consist of a GaInSb intermediate layer and a GaInNSb epilayer, both grown at a nominal thickness of 250 nm.

The samples were grown such that the nitrogen incorporation could be accurately determined using high-resolution XRD. The intermediate layer was grown with identical conditions as the nitrogen containing epilayer and, with the assumption that the effect on the Ga:In ratio of the RF plasma source and subsequent incorporation of nitrogen is negligible, both the indium and nitrogen incorporations can be independently determined.

Sample A was grown with an indium cell temperature of $\sim$730°C, while sample B had a higher indium cell temperature of $\sim$760°C, and as such, a higher indium flux. In each case the substrate temperature was fixed at $\sim$360°C. Further details on the general growth techniques used for the dilute nitride alloys in this work can be found in the introduction to this part of the thesis.

5.3 Lattice matching

The lattice constant of GaInNSb can be matched to that of $Ga_{1-z}Al_zSb$, for all z, by varying the degree of nitrogen and indium incorporation. The indium incorporation (y) required to maintain a lattice match to the endpoint alloys of GaAlSb was calculated as a function of nitrogen incorporation (x) using a linear interpolation between the lattice constants of the endpoints of $Ga_{1-y}In_yN_xSb_{1-x}$. The band parameters for GaSb, InSb and AlSb were taken from the review of III–V semiconductors and their alloys by Vurgaftman *et al.* [1] together with an experimentally determined bandgap value for GaSb (determined in chapter 3). The reduction in bandgap from that of the non-nitrogen containing alloy was determined using the 10-band $\mathbf{k} \cdot \mathbf{p}$ method outlined in section 1.6.3, with parameters from tight-binding calculations [38, 79] and from previous experimental work [78].

The blue axis (right) and traces of figure 5.2 show the percentage of indium, as a function of nitrogen incorporation, required to maintain a lattice match with GaSb (solid line) and AlSb (dashed line), the two endpoint binaries of GaAlSb. While the red axis (left) and traces show, for each substrate material, the bandgap as a function of nitrogen incorporation for these lattice matched alloys. As with the blue axis, lattice matching to GaSb is represented by the solid line and to AlSb by the dashed line.

The higher intrinsic lattice constant of AlSb results in the requirement for approximately 10 per cent more indium to achieve a lattice match than is required by GaSb. As a result the bandgap reduction in GaInNSb lattice matched to AlSb is greater than that seen in the GaSb lattice matched simulation.

5.4 Results and discussion

The XRD rocking curve around the 004 reflection of sample A is shown in figure 5.3 (solid line). The nominal thicknesses of the dilute nitride epilayer and the intermediate layer are 250 nm, while the nitrogen incorporation estimated from growth conditions is 1.5 per cent. The nitrogen and indium incorporations were independently determined from the dynamical simulation of the rocking curve (dashed line) and found to be 1.5 and 3.1 per cent respectively. Referring back to figure 5.2, it can be seen that 1.5 per cent nitrogen

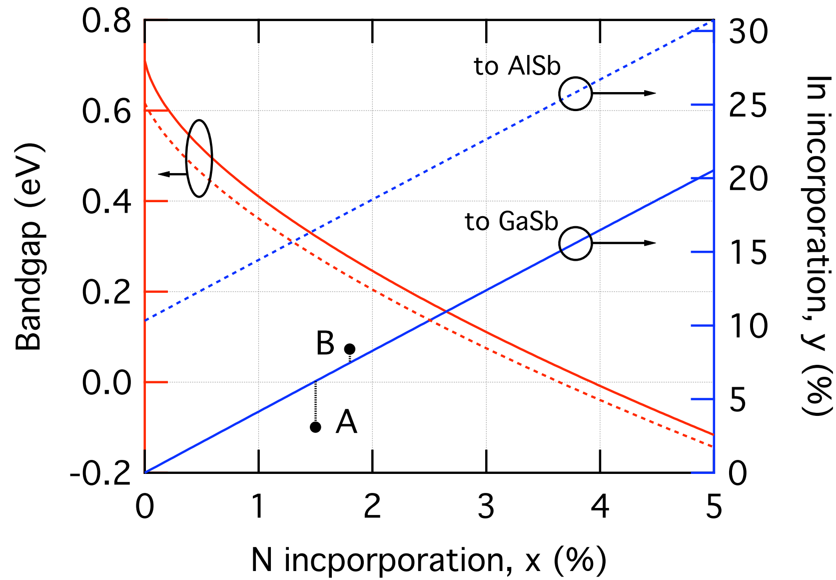

Figure 5.2: *Blue axis (right) and traces*: the calculated indium inclusion required, as a function of nitrogen incorporation, to maintain a lattice match to GaSb (solid line) and AlSb (dashed line). *Red axis (left) and traces*: the calculated bandgap of GaInNSb alloys lattice matched to GaSb (solid curve) and AlSb (dashed curve) as a function of nitrogen incorporation. Points *A* and *B* show the bandgap and lattice constant of the samples discussed in this chapter.

requires ∼6.2 per cent indium to attain a lattice match with GaSb. This prediction is supported by the rocking curve, in which the GaSb substrate and nitride epilayer peaks are seen to be well separated with the epilayer peak at a higher Bragg angle, indicating a smaller lattice constant than that of the substrate.

Sample *B* was grown with a higher indium cell temperature, in order to increase the indium incorporation within the sample and attain a lattice match between the epilayer and substrate. Figure 5.4 shows the rocking curve around the 004 reflection of sample *B* (solid line), together with the dynamical simulation (dashed line). The simulation of the rocking curve gives nitrogen and indium incorporations of 1.8 and 7.9 per cent, respectively.

The increase in nitrogen incorporation from 1.5 to 1.8 per cent seen in sample *B* was unintentional and it is suggested that the large indium atoms act to promote the incorporation of nitrogen in the films. This effect has been seen in a number of materials for example, as was discussed in the introduction, the growth rate of GaNSb is indicative of a self-surfactant effect due to the large antimony atoms enhancing the nitrogen incorporation.

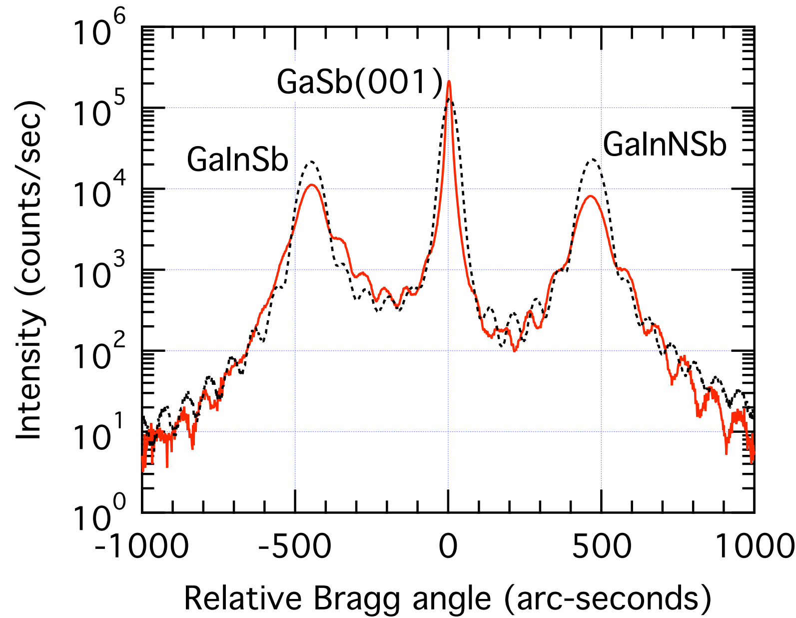

Figure 5.3: The x-ray diffraction rocking curve of the 004 diffraction maximum (solid line) of sample *A*, together with the dynamical simulation (dashed line) determining nitrogen and indium incorporations of 1.5 and 3.1 per cent respectively.

Also, increased nitrogen incorporation has been observed in the growth of Ga(In)NAs in the presence of an overpressure of Bismuth [64].

In both samples the XRD data exhibit clear Pendellösung interference fringes confirming the high structural quality of the layers. In addition, good agreement is observed between the data and the dynamical simulation, suggesting no significant lattice relaxation has occurred in the sample.

The calculated lattice mismatch between the GaSb(001) substrate and the intermediate $Ga_{0.921}In_{0.079}Sb$ layer is $\sim$0.5 per cent. To account for the possible effects of strain, leading to the inaccurate determination of indium and nitrogen content, reciprocal space maps (RSMs) around the symmetric 004 and asymmetric 224 Bragg reflections were performed. Figure 5.5 shows the RSM of the asymmetric reflection of sample *B*. It can be seen that both the intermediate and nitride layers show predominantly coherent growth with the substrate. Analysis of the RSMs revealed that the intermediate GaInSb layer was 12 ± 2 per cent relaxed while the nitride epilayer was pseudomorphically grown. Inclusion of the strain into the simulation led to the revision of the indium incorporation from 7.9 to 8.4 ± 0.2 per cent, while the nitrogen content remained unchanged.

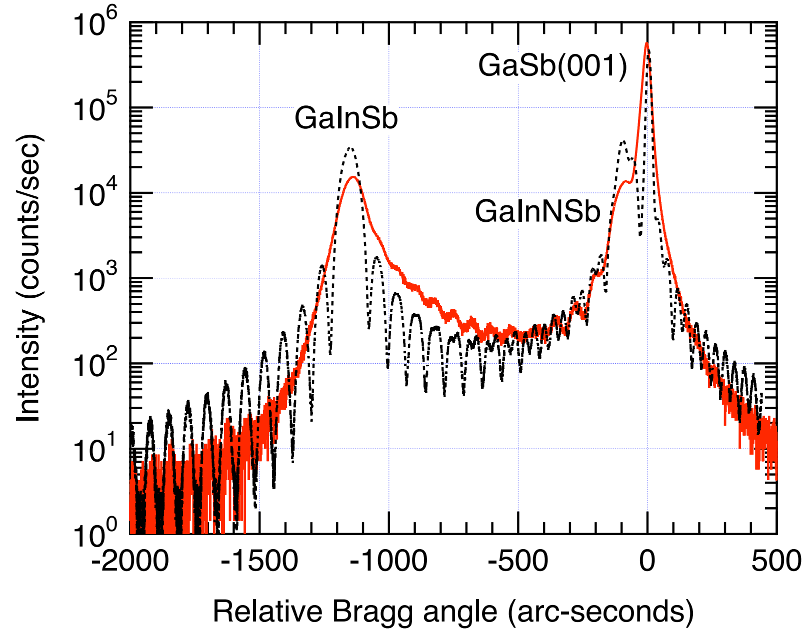

Figure 5.4: The x-ray diffraction rocking curve of the 004 diffraction maximum (solid line) of sample B, together with the dynamical simulation (dashed line) determining nitrogen and indium incorporations of 1.8 and 7.9 per cent respectively. The GaSb substrate peak can be seen centred at 0 arc-sec with the dilute nitride epilayer appearing as a shoulder on this peak indicating a lattice match close to the GaSb substrate.

It can be seen from figure 5.2 that an indium incorporation of 8.4 per cent would require a nitrogen concentration of ~2 per cent to achieve a lattice match with GaSb. This is supported by the XRD measurements which show the dilute nitride epilayer as a shoulder on the low Bragg angle side of the strong GaSb substrate peak, indicative of a fractionally higher lattice constant.

The lattice constant and nitrogen incorporations are summarised in figure 5.2. For a given nitrogen concentration, points lying below (above) the lattice matching line represent a deficiency (abundance) of indium and therefore a lattice constant lower (higher) than that of GaSb.

Atomic force microscopy was used to determine the rms roughness of a nominally lattice matched sample of GaInNSb grown directly on a GaSb(001) substrate with the same growth conditions as sample B. The average rms roughness from a number of 5×5 μm^2 images was found to be ~1.8 nm. Figure 5.6 shows an atomic force microscope (AFM) image of a 5×5 μm^2 section of the sample with a height scale of 10 nm.

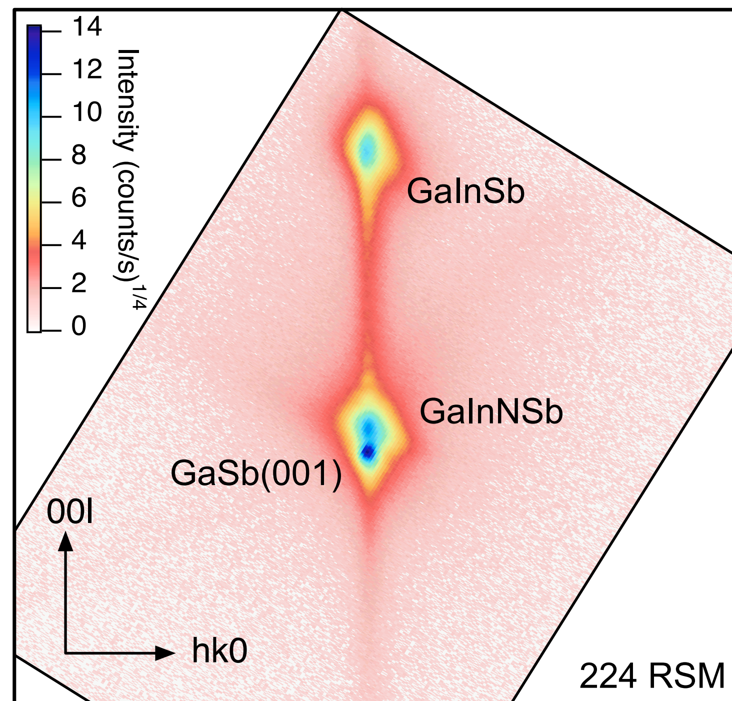

Figure 5.5: The reciprocal space map of the 224 diffraction maxima of sample B. Analysis of the 004 and 224 RSMs indicates strain within the buffer and epilayer to be 12.5 and less than 1 per cent respectively and indicates a revision in indium incorporation from 7.9 to 8.4 per cent.

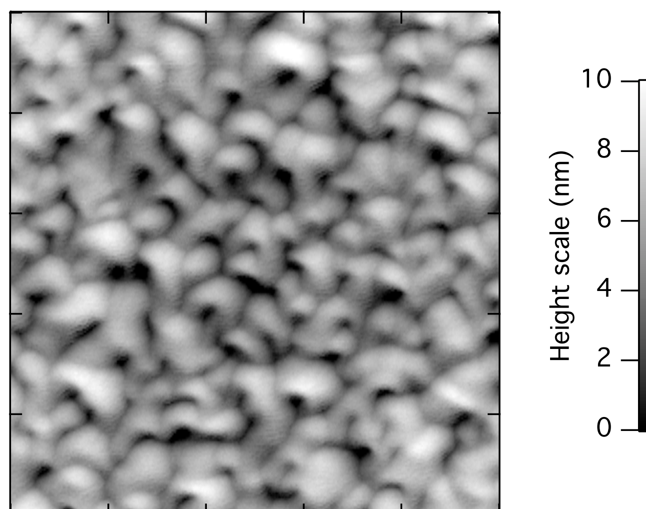

Figure 5.6: A 5×5 μm^2 AFM image of a 250 nm thick GaInNSb layer grown on GaSb(001) with nominal nitrogen and antimony incorporations of 1.8 and 8.4 per cent respectively. The average rms roughness across a number of 5×5 μm^2 images was found to be $\sim$1.8 nm.

5.5 Conclusions

The growth of dilute nitride alloys of GaInSb lattice matched with GaSb has been demonstrated, highlighting the potential for the lattice-matching of this quaternary alloy to both GaSb and virtual substrates of the wide gap semiconductor AlSb. The high quality of the samples is confirmed by the presence of Pendellösung fringes in the high-resolution XRD measurements and by the low rms roughness ($\sim$1.8 nm for 5×5 μm^2) determined by atomic force microscopy. The nitrogen and indium incorporations were determined from high-resolution XRD measurements of samples containing an intermediate GaInSb layer and a lattice match was shown with nitrogen and indium incorporations of 1.8 and 8.4 per cent respectively.

Conclusions and further work: Dilute nitrides

In chapter 3, a value of 2.6 eV was determined for the BAC coupling parameter of the dilute nitride alloy GaNSb. Infrared absorption measurements were used to determine the position of the E_+ conduction band as a function of nitrogen incorporation between 0.2 and 1.0 per cent. A least squares fitting of the position of E_+ as a function of nitrogen incorporation was made assuming a fixed nitrogen state energy of 0.78 eV (as determined from tight-binding calculations). Finally, the evolution of the E_+ level with nitrogen incorporation was shown to agree well with the predictions of Lindsay and O'Reilly's 10-band $\mathbf{k} \cdot \mathbf{p}$ Hamiltonian, with preliminary parameters determined from tight-binding calculations.

Dilute nitride alloys of the narrow gap semiconductor InSb were investigated in chapter 4. The incorporation of nitrogen into the material caused an increase in the fundamental absorption edge, however, by considering the competing effects of Moss-Burstein band filling and bandgap renormalisation it was inferred that a reduction in the bandgap of the material from that of the binary host had occurred.

Finally, in chapter 5 the lattice matching of the quaternary alloy GaInNSb with the host binary, GaSb was defenestrated. The growth of the material with a GaInSb intermediate layer allowed the determination of both the indium and nitrogen incorporations. High-resolution XRD rocking curves indicated the high structural quality of the layers and bandstructure calculations of the material highlight its potential for use in the exploitation of the atmospheric transmission windows of 3–5 and 8–14 μm.

Any future work and application of dilute nitride antimonides is strongly dependent on the reduction of the free carriers in the material. In the case of GaSb, the incorporation of nitrogen dramatically increases the hole concentration giving rise to significant band-tailing of the conduction band. For InSb, the incorporation of nitrogen, rather than

decreasing the energy of the fundamental optical transition, increases it due to the Moss-Burstein effect. The future of dilute nitride antimonides in the production of optoelectronic devices is dependent or reducing this charge excess. This has been achieved in dilute nitride arsenides by careful annealing studies and the use of surfactants.

Once the free electron density within the materials has been reduced, photoluminescence and photomodulated reflectance experiments can be performed to more accurately determine the electronic and optical properties of the materials.

Part II

Cadmium oxide

Introduction

Early reports on the growth of epitaxial cadmium oxide (CdO) by a variety of techniques including activated reactive evaporation [80,81], solution growth [82], spray pyrolysis [83], chemical vapour deposition [84], and dc reactive magnetron sputtering [85], were prompted by the need for highly conductive transparent contacts for the use in solar cells and flat-panel displays. The majority of these materials were of poor crystalline quality, being poly-crystalline or amorphous, and therefore unsuitable for optoelectronic applications.

More recently, a resurgence of interest in group II(B) oxides has been prompted by the technological importance of optoelectronic materials and devices operating at short wavelengths in the blue/ultraviolet region of the electromagnetic spectrum. Significant interest has been shown in zinc oxide (ZnO), with a direct room temperature bandgap of ∼3.4 eV and a large exciton binding energy of ∼60 meV which make it a suitable material for short wavelength diodes and lasers operating at room temperature [24, 86]. The emission wavelength of ZnO devices can be extended by alloying with magnesium oxide ($E_g \simeq 7.7$ eV) and CdO ($E_g \simeq 2.3$ eV), shifting the bandgap to higher and lower values, respectively [26].

For CdO to be a viable material for use in optoelectronic devices, either alone or alloyed with other group II oxides, it is necessary to produce material of high crystalline quality. Such materials have been produced by metal-organic molecular-beam epitaxy [87] on GaAs(001) substrates and by metal-organic vapour-phase epitaxy (MOVPE) on sapphire substrates [88, 89]. Here, the work of Zúñiga-Pérez *et al.* is summarised, outlining the epitaxial growth of the high quality single crystalline CdO(001) layers discussed in the following experimantal chapters. The samples were grown on r-plane sapphire substrates by MOVPE [89].

The CdO layers were grown, at a nominal thickness of 900 nm, at atmospheric pressure in a horizontal vent-run type MOVPE reactor, equipped with two independent gas inlets. The oxygen and cadmium precursors (tertiary butanol and dimethylcadmium) were transported into the reaction chamber by a purified nitrogen carrier gas and entered the reactor through the lower and upper inlet, respectively. The two-inlet configuration gives a greater growth rate uniformity along the reactor, as well as a better control over the par-

tial pressures of the precursors. The tertiary butanol to dimethylcadmium flux ratio was maintained at 10:1 throughout the growth process while the RF heated graphite susceptor provided growth temperatures in the range 308 to 405°C. X-ray diffraction (XRD) measurements were performed using a Philips PANalytical X'Pert PRO Materials Research Diffractometer with a four-crystal Bartels-type Ge(220) monochromator.

Figure II.1 shows a typical XRD scan of the CdO layers grown in work. It can be seen that the scan is dominated by the CdO(00l) reflections, confirming the high degree of crystallinity in the films. Prior to this work [88] only cubic substrates, e.g. Si(111) [85] and GaAs(001) [90], had been used to grow (00l) oriented CdO.

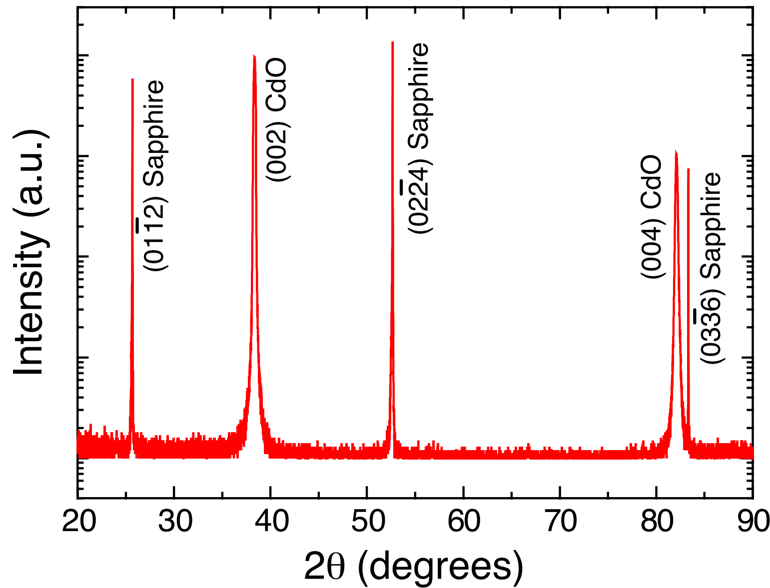

Figure II.1: An XRD scan of CdO grown by MOVPE on sapphire at 308°C. The single crystalline nature of the material is confirmed by the presence of only (00l) CdO peaks.

The crystalline quality of the samples was determined from the full-width at half-maximum (FWHM) of rocking curves around the (002) CdO reflection. This can be seen as a function of growth temperature in figure II.2. It can be seen from the figure that the lowest values of the FWHM occur at ∼385°C. At this temperature, the FWHM of the XRD peak is 0.14°, very close to the best reported value in the literature of 0.13°, from CdO grown by pulsed laser deposition on MgO(111) substrates [91], and significantly better than those grown on GaAs(001) by metal-organic molecular beam epitaxy (∼0.55°) [90].

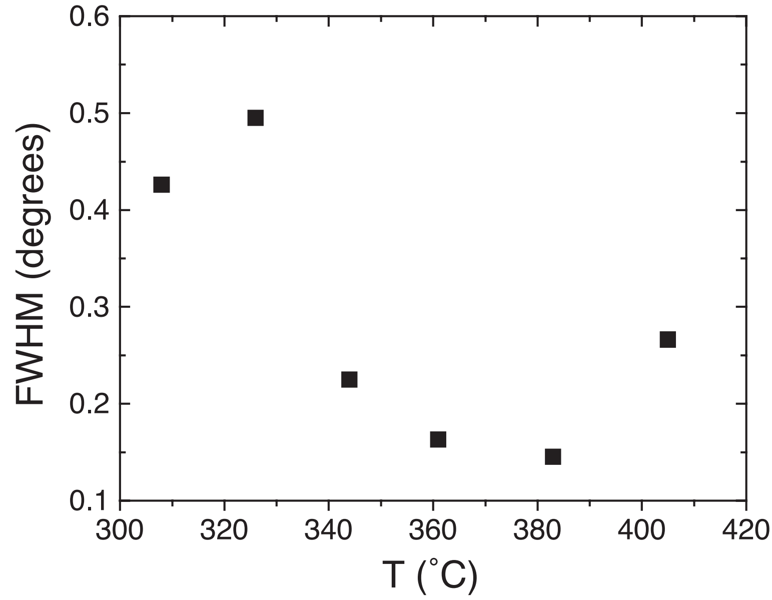

Figure II.2: The full-width at half-maximum values of the (002) rocking curve of CdO shown as a function of temperature. It can be seen that the minimum, and by extension the highest crystalline quality, occurs at a growth temperature of ∼385°C.

The surface morphology was studied using contact mode scanning force microscopy, with a home made microscope setup combined with an SPM100 control unit. V-shaped Si_3N_4 tip-sharpened cantilevers with a tip radius of ∼10 nm and nominal force constants of 0.1 and 0.5 N/m were used.

For the optimum growth temperature samples, the otherwise flat surface exhibits narrow grooves, giving an rms roughness of ∼2 nm, measured from a 4 μm^2 image. With decreasing growth temperature the surface structure degrades, showing a strong mosaic spread resulting in a FWHM value three times that of the optimally grown samples.

Table II.1: Perpendicular ($a_\perp$) and in-plane (a) lattice parameters obtained from (0 0 l) symmetrical reflections and from {2 2 4} asymmetrical reflections on CdO layers grown at 361°C, and the Landolt-Börnstein CdO lattice parameter [92] (a_0).

$a_\perp^{(0\ 0\ l)}$ (Å)	$a_\perp^{(2\ 2\ 4)}$ (Å)	$a^{(2\ 2\ 4)}$ (Å)	a_0 (Å)
4.693 ± 0.003	4.693 ± 0.004	4.701 ± 0.009	4.697

Finally, the lattice parameter in the growth direction was determined from (002) and (004) symmetrical reflections, and from reciprocal space maps on {224} asymmetrical reflections.

The results are summarised in table II.1.

It can be seen that the perpendicular lattice parameters determined from the symmetric and asymmetric reflections are equal, and that they coincide with the obtained in-plane lattice parameter. These results indicate that complete strain relaxation has taken place and that fully relaxed CdO layers have been grown on r-plane sapphire.

Chapter 6

CdO bandgap and effective mass determination

The room temperature bandgap and the band-edge effective mass of single crystal epitaxially grown cadmium oxide are determined from infrared reflectivity, ultraviolet/visible absorption and Hall effect measurements. Infrared reflectivity measurements of the samples are performed to determine the plasma frequency as a function of carrier concentration from which the band-edge effective mass is determined. The fundamental optical transition as a function of carrier concentration is obtained from ultraviolet/visible absorption measurements. As the material is unintentionally degenerately doped, this transition occurs between the valence band and the Fermi level, situated within the conduction band. Simulation of the fundamental optical transition using a non-parabolic conduction band and the newly determined band-edge effective mass enables the determination of the bandgap of the material.

6.1 Introduction

Cadmium oxide, like other ionic semiconductors e.g. ZnO and InN, exhibits an intrinsically high electron density. The origin of this property is the low energy of the conduction band minimum at the Γ-point compared to the rest of the Brillouin zone, resulting in a strong propensity for the creation of donor-type defects, a topic that is discussed further in chapter 7. Typically, the carrier concentrations found in as-grown cadmium oxide are so high that the Fermi level is located within the conduction band.

This high unintentional degenerate doping has two main implications for the determination of the bandgap of the material. First, it causes the absorption edge to be strongly dependent on the carrier concentration of the material with the fundamental optical transition occurring between the valence band and the lowest unoccupied conduction band level, situated close to the Fermi-level within the conduction band [71, 72]. Second, in degenerately doped systems electron-electron and electron-impurity interactions take place between the electrons of the conduction band and the ionised impurities from which the carriers originate, causing a downward shift in the conduction band [73].

The currently accepted value for the room temperature bandgap of CdO is 2.28 eV. This was determined from thermoreflectance measurements performed at 100 K of single crystal CdO grown by a vapour transport technique [93]. Despite these measurements by Koffyberg being performed at 100 K, a number of recent papers have cited the value without qualification of temperature, or claiming a room temperature bandgap in the range 2.2–2.4 eV [27, 94–97]. In summarising his work Koffyberg states that the interpretation of the data is qualitatively correct. However, he concedes the inclusion of the non-parabolicity of the conduction band and the complex shape of the valence band may produce better agreement with the data [93].

The literature values for the cadmium oxide effective mass are wide ranging, typically lying between 0.1 m_0 and 0.3 m_0, however, values as high as 1.19 m_0 have been reported. In both cases the values were determined from the free carrier dispersion [92]. The most commonly used value for the effective mass of CdO is 0.14 m_0 which Koffyberg uses, without justification or citation, in his thermoreflectance paper [93].

6.2 Experimental details

Single crystal CdO samples were grown by MOVPE on r-plane sapphire substrates as described in the introduction to this part of the thesis. The samples were annealed under ultra-high vacuum at a temperature of 400°C for between 2 and 24 hours in order to reduce the carrier concentration of the material. The free electron concentrations were reduced from $\sim 1.8\times10^{20}$ cm^{-3}, for the as grown samples, to as low as 4.4×10^{19} cm^{-3} for the post-growth annealed samples.

Infrared reflectivity measurements were made using a Perkin Elmer Spectrum GX FTIR spectrometer with a 35° specular reflection with respect to the surface normal. Transmission geometry ultraviolet/visible absorption measurements were performed using a Perkin Elmer Lambda 25 system working between 1.24 and 4.00 eV. All measurements from both optical systems were taken at room temperature. Finally, single field Hall effect measurements, also conducted at room temperature, were performed using the standard van der Pauw method. Further details on the experimental techniques can be found in chapter 2.

6.3 Results and discussion

The infrared reflectivity spectra of three CdO samples are shown in figure 6.1. The spectra were simulated using an expression describing the propagation and reflection of electromagnetic radiation from a two-layer stratified medium derived from the Fresnel equations [98]. This expression is dependent on the complex refractive indices ($\tilde{n}$) of the materials which are described in terms of the two-oscillator dielectric model of the complex permittivity ($\tilde{\epsilon}$) where

$$\tilde{\epsilon} = \tilde{n}^2 = \epsilon(\infty) + \frac{[\epsilon(0) - \epsilon(\infty)]\omega_T^2}{\omega_T^2 - \omega - i\omega\gamma} - \frac{\epsilon(\infty)\omega_p^2}{\omega(\omega + i/\tau)} \tag{6.1}$$

Here, ω is the frequency of the incident radiation, $\epsilon(0)$ and $\epsilon(\infty)$ are the static and high-frequency dielectric constants, ω_{TO} and ω_p are the TO-phonon and plasma frequencies, and γ and τ are the phonon damping and free-carrier scattering time.

Simulation of the reflectivity spectra enables the determination of the plasma frequency and the epilayer thickness. The sample thicknesses obtained from fitting the reflectivity

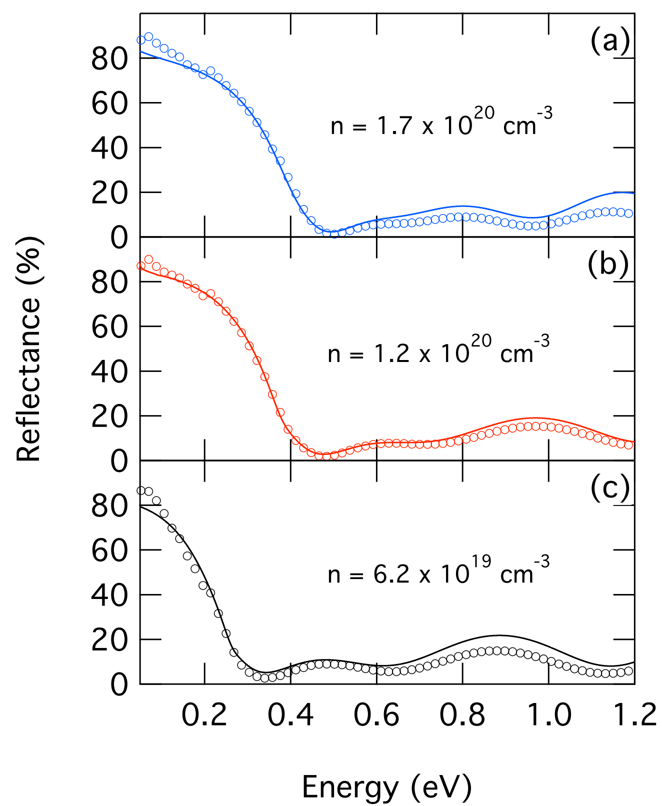

Figure 6.1: Infrared reflectivity spectra of three CdO samples with carrier concentrations of (a) 1.7×10^{20}, (b) 1.2×10^{20}, and (c) 6.2×10^{19} cm^{-3} (open circles). In each case the simulation based on the two-oscillator dielectric function is shown (solid lines).

spectra were in the range 0.48–0.65 μm. The layers have been previously been shown to be fully relaxed from the comparison of the lattice parameters determined from XRD reciprocal space maps and of literature values for bulk grown material [88].

The plasma frequency plotted as a function of carrier concentration for the CdO samples is shown in figure 6.2 together with calculated values for three different band-edge effective masses. Simulation of the plasma frequency as a function of carrier density was calculated using the following relation

$$\omega_p^2 = \frac{ne^2}{m^*_{\rm av}\epsilon(\infty)\epsilon_0} \tag{6.2}$$

where n is the free carrier density, e is the electronic charge, $m^*_{\rm av}$ is the density of states integrated effective mass and ϵ_0 the permittivity of free space.

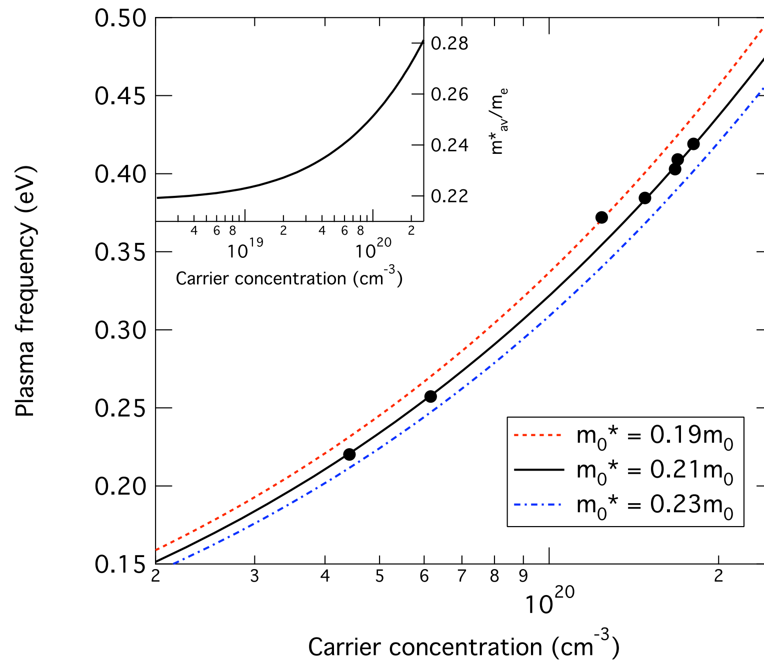

Figure 6.2: The plasma frequency of the CdO samples determined from infrared reflectivity measurements plotted as a function of carrier concentration (filled circles) together with three simulations of the plasma frequency calculated with a bandgap of 2.16 eV and band-edge effective mass values of 0.19 m_0, 0.21 m_0 and 0.23 m_0 (lines). The *inset* shows the density of states integrated effective mass as a function of carrier concentration.

The value of effective mass used in equation 6.2 is dependent on the carrier density as the Fermi level is situated within the conduction band, due to the high electron densities observed in our samples. The effective mass for a given carrier density was calculated by modelling the conduction band dispersion of CdO using a 2-band $\mathbf{k} \cdot \mathbf{p}$ method, and

including the effect of bandgap renormalisation following Berggren and Sernelius [73]. Given this band dispersion, the carrier concentration and density of states integrated effective mass for a given Fermi level (E_F) were determined from

$$n(E_F) = \int g(E) f(E, E_F) \mathrm{d}E \tag{6.3}$$

and

$$m^*_{\mathrm{av}}(E_F) = \frac{1}{n(E_F)} \int m^*(E) g(E) f(E, E_F) \mathrm{d}E \tag{6.4}$$

where $g(E)$ is the density of states, $f(E, E_F)$ the Fermi-Dirac distribution and $m^*(E)$ the energy dependent effective mass, calculated from the derivative of the band dispersion.

The bandstructure was calculated using the band-edge effective mass (m^*_0) and the bandgap (E_g) as input parameters. The calculations shown in figure 6.2 have band-edge effective mass values of 0.19 m_0, 0.21 m_0, and 0.23 m_0 together with a bandgap value of 2.16 eV. The effect of the bandgap value on the plasma frequency simulations was found to be negligible in the range 1.9 to 2.3 eV.

It can be seen from figure 6.2 that an effective mass of $0.21m_0$ fits the experimentally determined plasma frequencies very well. It should be noted, however, that both the simulations of the infrared reflectivity and the calculated plasma frequency rely on the high-frequency dielectric constant of CdO. Using infrared reflectivity, a unique determination of the high-frequecy dielectric constant and the epilayer thickness is not possible, consequently a previously determined value of 5.3 for $\epsilon(\infty)$ was used [92]. A recent paper investigating the effects of the carrier concentration on the dielectric function of various TCOs by spectroscopic ellipsometry suggests that the value of $\epsilon(\infty)$ is linearly reduced with increasing carrier concentration. The reduction in $\epsilon(\infty)$ for ZnO:Ga was found to be $\sim$5 per cent for an increase in carrier concentration from 3.2×10^{19} to 7×10^{20} cm^{-3} [99]. It is therefore assumed that the increase in $\epsilon(\infty)$ for the decrease in carrier concentration observed in our CdO samples is not likely to have a significant effect on the results.

The ultraviolet/visible α^2 spectra of three CdO samples are shown in figure 6.3. The position of the fundamental direct optical transition was obtained from the point of intersection between the linear extrapolations of the background absorption and the fundamental absorption feature seen in the vicinity of the CdO direct bandgap.

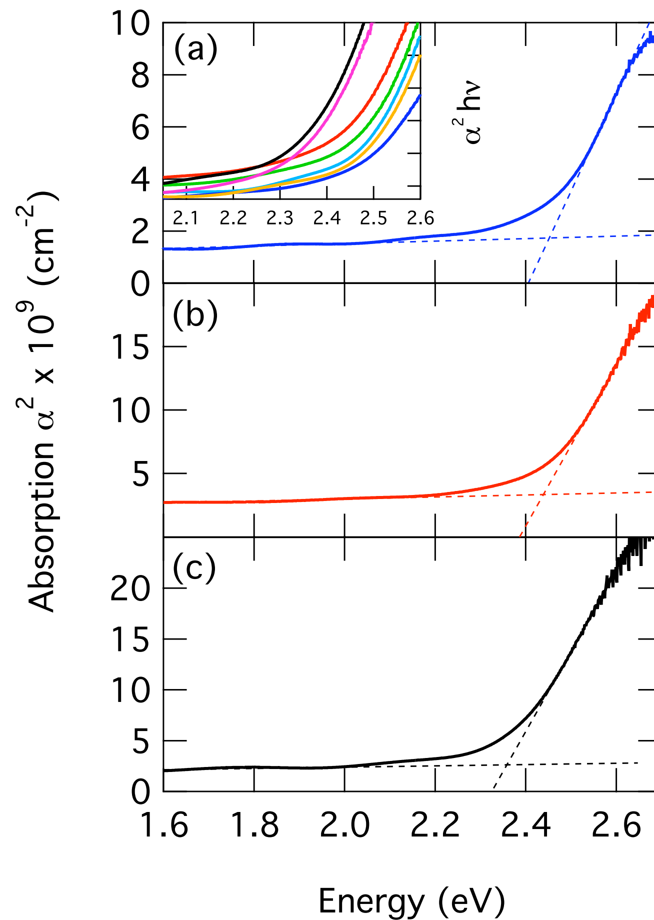

Figure 6.3: The ultraviolet/visible absorption spectra of three CdO samples with carrier concentrations of (a) 1.7×10^{20}, (b) 1.2×10^{20}, and (c) 6.2×10^{19} cm^{-3}. The position of the fundamental optical transition (from valence band to Fermi-level) is seen to increase with carrier concentration. This trend is further highlighted in the *inset* where the $\alpha^2 h\nu$ spectra of all samples considered in this work is shown.

The high unintentional n-type doping observed in cadmium oxide results in a strong dependence of absorption edge with carrier concentration [71, 72], as well as the less pronounced effect of bandgap renormalisation resulting from the electron-electron and electron-defect interactions [73]. As with the calculation of plasma frequency, the Fermi-level as a function of carrier concentration is determined from a non-parabolic 2-band $\mathbf{k} \cdot \mathbf{p}$ conduction band. Making the assumption that direct transitions take place from a single, non-dispersive valence band to the Fermi-level of the non-parabolic conduction band, the position of the fundamental direct absorption feature is obtained. A non-dispersive valence band was used as recent density functional theory calculations suggest the heavy-hole band of rocksalt CdO changes by less than 50 meV within the region of k-space of interest, increasing to maxima at the L-point and between the Γ- and X-points [100].

The calculated absorption edge as a function of carrier concentration is shown in figure 6.4 for bandgap values of 2.14, 2.16 and 2.18 eV and with the previously determined band-edge effective mass value of $0.21m_0$. It can be seen that good agreement between the calculated and experimentally determined values is found within this narrow range of bandgap energies.

The mobility of the carriers determined from Hall effect measurements and from the infrared reflectivity spectra, using the relation $\mu = e\tau/m^*$, where τ is the electron lifetime, are shown as a function of carrier concentration in figure 6.5. It can be seen that the values of mobility determined from optical measurements (optical mobility) are significantly higher than those determined from transport measurements.

Previous work on the conduction mechanism of highly doped zinc oxide [101] have suggested that scattering at the boundaries separating the crystalline grains and in the vicinity of ionised impurities are the primary mechanisms limiting the mobility in the material. The scattering at grain boundaries results from a Coulombic repulsion between the free charge carriers in the material and carriers trapped in defect states originating from incomplete atomic bonding at the grain boundaries [102]. The origin of ionised impurity scattering is the Coulombic interaction between free charge carriers and ionised impurities. While the grain boundary scattering is confined to the regions close to the crystalline grain edges, ionised impurities scattering will occur throughout the crystalline grains.

The electron mobility determined from d.c. Hall effect measurements will be affected by

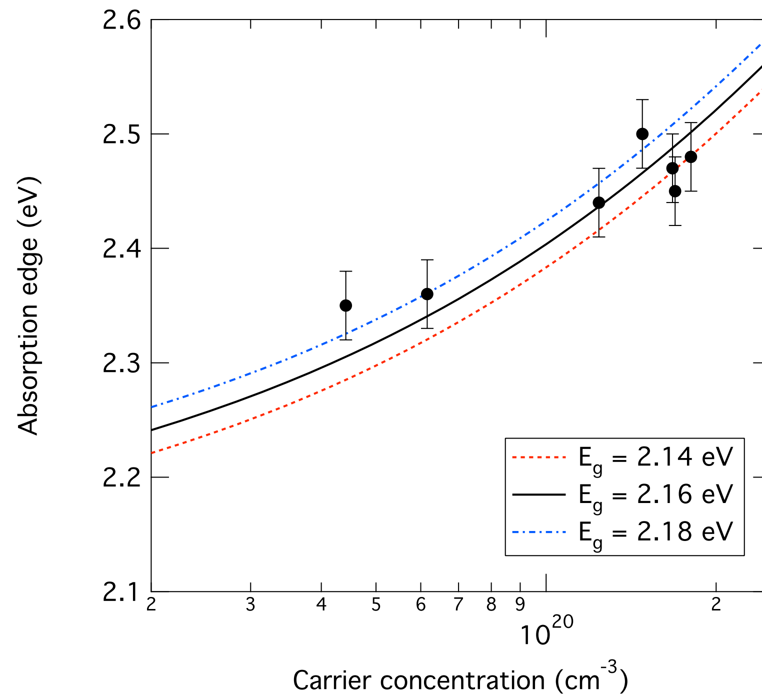

Figure 6.4: The position of the fundamental optical transition plotted as a function of carrier concentration for the CdO samples together with simulations calculated using a non-parabolic 2-band $\mathbf{k} \cdot \mathbf{p}$ conduction band with a band-edge effective mass of 0.21 m_0 and bandgaps of 2.14, 2.16, and 2.18 eV.

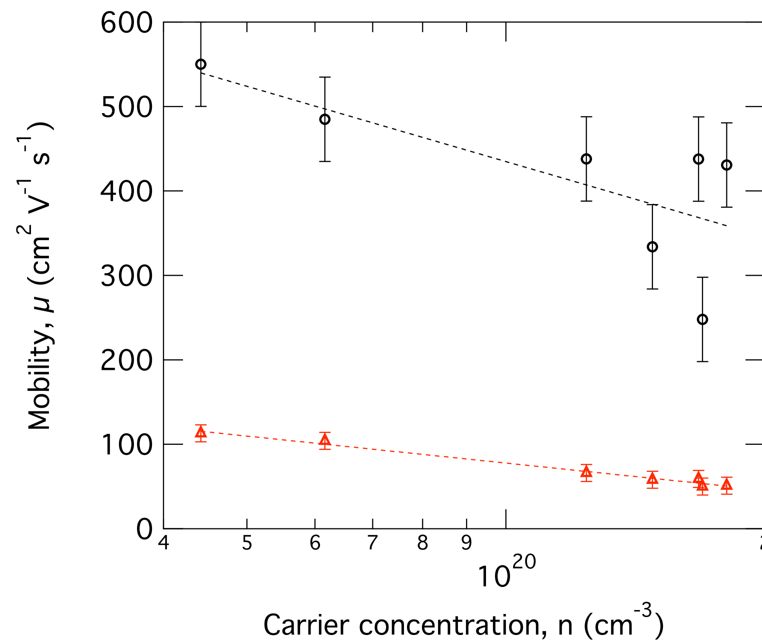

Figure 6.5: The mobility as a function of carrier concentration obtained from carrier lifetimes of the reflectance measurements (circles) and Hall effect measurements (triangles). In each case the mobility is seen to decrease with increasing carrier concentration.

scattering from both grain boundaries and ionised impurities as the measurement is dependent on the transport across the entire sample. The mobility obtained from infrared reflectance measurements, however, will be largely insensitive to grain boundary scattering, as the grain boundaries constitute only a small volume of the material compared to the crystalline grains. This means that the reflectance from crystalline grains will be dominant, and will therefore give a mobility representative of the degree of ionised impurity scattering in the material.

It can be seen in figure 6.5 that the values of mobility obtained from reflectance measurements are significantly higher than those determined from Hall effect measurements. This indicates that the dominant scattering mechanism, in both the as-grown and annealed CdO samples in this study, is that of the grain boundaries. Previous studies of gallium doped zinc oxide have shown grain boundary scattering [103] and, for highly doped material, ionised impurity scattering [104] being the dominant scattering mechanisms. In the latter case, the mobility determined from optical measurements gave values very similar to those determined by Hall effect measurements.

The rate of decrease with carrier concentration observed in the optical mobility is greater than that seen in the Hall mobility. This again highlights the fact that the optical mobility is representative of ionised impurity scattering. The free carriers in the material come from ionised point defects produced during growth, therefore, a higher carrier concentration is indicative of a higher concentration of ionised impurities. The mobility determined from the Hall effect measurements shows a less pronounced decrease with carrier concentration as the mobility here is dominated by scattering at crystalline grain boundaries.

The values of mobility determined by Hall effect measurements for CdO in this work are similar to those of found in commercially used TCOs such as tin doped indium oxide (ITO), while the values obtained from optical measurements are significantly higher. Typical values of mobility for ITO are of the order of 100 $\text{cm}^2\ \text{V}^{-1}\ \text{s}^{-1}$ for carrier concentrations of $\sim 10^{21}\ \text{cm}^{-3}$ [105, 106]. With the optimisation of growth conditions to increase the electron mobility and suitable doping to increase the carrier concentration CdO would make a promising material for commercial applications requiring very highly conducting transparent materials.

6.4 Conclusion

Infrared reflectivity and ultraviolet/visible absorption spectroscopies have been used, together with Hall effect measurements, to determine the bandgap and band-edge effective mass of single-crystal epitaxial cadmium oxide grown by MOVPE on r-plane sapphire substrates. The band-edge effective mass and bandgap values were found to be $0.21m_0$ and 2.16 $\pm$0.02 eV, respectively. The bandgap value obtained was lower than the value frequently cited as the room-temperature bandgap determined by Koffyberg from thermoreflectance measurements performed at 100 K. Finally, a comparison between the mobilities of the material determined by Hall effect and optical measurements was made indicating that the dominant scattering mechanism in the samples is due to the grain boundaries. In addition, the intrinsically high mobility of single crystal cadmium oxide was shown from measurements of the optical mobility, which are largely insensitive to scattering at the grain boundaries.

Chapter 7

Fermi-level stabilisation of cadmium oxide

High energy $^{4}He^{+}$ ion irradiation of epitaxially grown cadmium oxide films has been used to stabilise the Fermi energy close to the charge neutrality level. The position of the charge neutrality level is determined from Hall effect measurements and from density of states calculations of the cadmium oxide conduction band. The charge neutrality level is also independently determined from the comparison of ultraviolet/visible absorption measurements with density functional theory calculations. Finally, the high unintentional n-type conductivity of cadmium oxide is explained, within the framework of the amphoteric defect model, to be a result of the position of the charge neutrality level.

7.1 Introduction

The high unintentional doping seen in epitaxial cadmium oxide, may be described in terms of Walukiewicz's amphoteric defect model (ADM) [107]. This model has been used to explain a number of phenomena pertaining to the doping of semiconductor compounds, including doping limits in wide bandgap semiconductors [108], and the propensity for certain materials to exhibit unintentional intrinsic doping [109].

The main concept of the ADM is that point defects produced during growth can lead to the formation of defect states with donor- (D^+) or acceptor-like (D^-) character depending on their position with respect to the Fermi level. A schematic representation of the distribution of potential defect states is shown in figure 7.1. The average position of the potential defect states is referred to as the charge neutrality level (CNL). If the Fermi level is located below the CNL then it is energetically favourable for a defect to produce a donor-like state. Whereas when the Fermi level is found above the CNL it is more likely that an acceptor-like state will be produced. In each case, the most probable defect state produced will act to move the Fermi level towards the CNL.

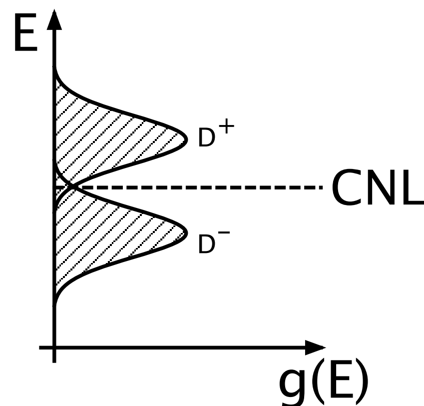

Figure 7.1: Schematic representation of the energy distribution of potential defect states. The charge neutrality level marks the average position of the donor-like (D^+) and acceptor-like (D^-) states.

High energy particle irradiation can be used to induce point defects in a material in order to stabilise the Fermi level at the CNL. In this chapter, the irradiation and stabilisation of the Fermi level in epitaxial cadmium oxide is reported and the high unintentional doping is discussed in terms of the position of the charge neutrality level and the ADM.

7.2 Experimental details

The single crystalline cadmium oxide samples used in this chapter were grown by metal-organic vapour-phase epitaxy; further details on their growth and structural characterisation can be found in the introduction to this part of the thesis. The samples were irradiated at the Surrey Ion Beam Centre with 1 MeV He^+ ions in order to increase their carrier concentrations by introducing point defects into the material.

The irradiation dose was determined from the displacement damage dose methodology for modelling extraterrestrial solar cell degradation [110]. The range of displacement damage doses chosen was guided by the work of Li *et al.* in their work investigating the Fermi-level stabilisation energy of group III nitrides [111]. Five displacement damage doses in the range 7.5×10^{13} to 5×10^{16} MeV g^{-1} were chosen for the particle irradiation. From this the He^+ fluences were calculated from the following relation:

$$D_d = \text{NIEL} \times \text{fluence} \tag{7.1}$$

where D_d is the displacement damage dose and NIEL is the non-ionising energy loss. The non-ionising energy loss of a system can be calculated using the stopping and range of ions in matter (SRIM) program [112]. The data from the SRIM calculation is used to determine the total energy loss as a function of depth due to ionisation and vacancy production. The method used to calculate the NIEL is detailed in reference 110.

Figure 7.2 shows the non-ionising energy loss of He^+ ions in cadmium oxide. It can be seen that this energy loss increases with increasing depth in the material, so an average value of 1.17 MeV cm^2 g^{-1} was used for the calculation of the He^+ fluences. The range of He^+ fluences used to irradiate the samples was in the range 6.4×10^{13} to 4.3×10^{16} cm^{-2}.

The carrier concentrations of the samples were determined from Hall effect and infrared reflectivity measurements. The sheet density of the samples was determined from Hall effect measurements, while their thicknesses were obtained from the simulation of the infrared reflectivity spectra. Further details of the Hall effect measurements and the infrared reflectivity simulation can be found in chapters 2 and 6.

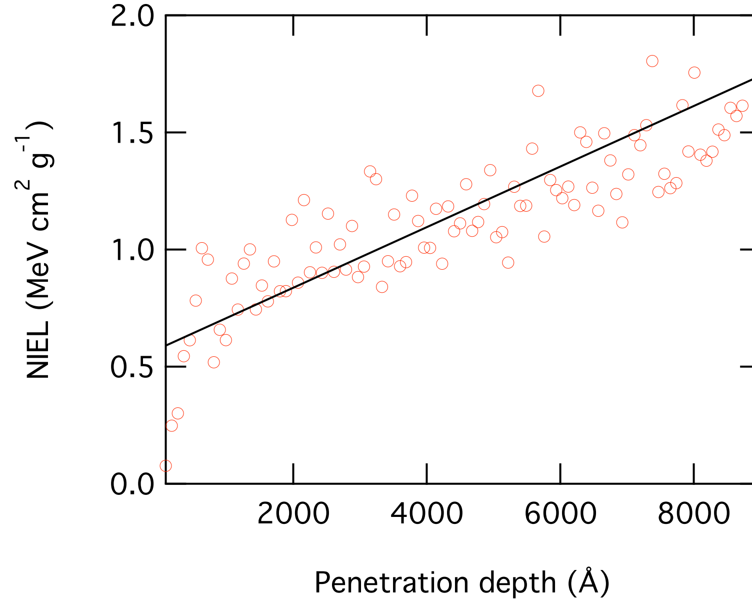

Figure 7.2: The non-ionising energy loss (NIEL) of 1 MeV $^4He^+$ ions in cadmium oxide, calculated using the ionisation energy loss and vacancy production rate due to ions and recoils determined from SRIM [110].

7.3 Results and discussion

The carrier density as a function of displacement damage dose (D_d) is shown in figure 7.3 for the irradiated samples (open circles). The carrier concentration of the material prior to particle irradiation was $\sim 1.8\times10^{20}$ cm^{-3} therefore, for the two least irradiated samples, the carrier concentration is seen to decrease before increasing back to the value of the unirradiated material. The carrier concentration of the two most heavily irradiated samples is greater than that of the material prior to irradiation. The rate of increase of carrier concentration between these two points is indicative of a plateau in the carrier concentration at $\sim 2.2\times10^{20}$ cm^{-3}.

The carrier concentration as a function of Fermi level was calculated from the 2-band $\mathbf{k}\cdot\mathbf{p}$ conduction band, as calculated in the previous chapter. The results of this are shown in figure 7.4, where the Fermi level for each sample (with respect to the valence band at the Γ-point) is given as a function of displacement damage dose. The samples prior to irradiation have a Fermi level ∼2.52 eV above the Γ-point valence band, initially with irradiation this decreases to ∼2.50 eV before increasing and beginning to stabilise at ∼2.56 eV. This value corresponds to 0.36 eV above the Γ-point conduction band minimum, as calculated from

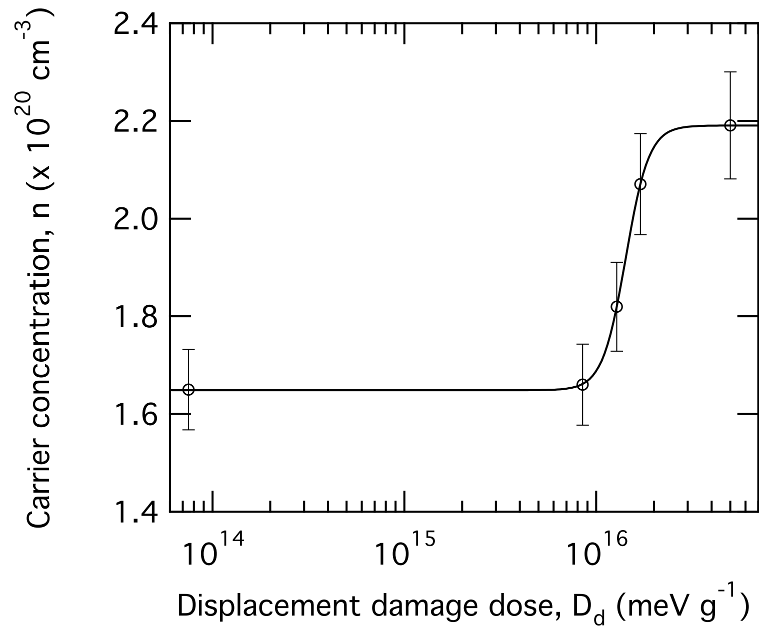

Figure 7.3: The carrier concentration, determined from Hall effect measurements using thicknesses from infrared reflectivity analysis, plotted as a function of displacement damage dose for the five cadmium oxide samples (open circles), the curved line is present as a guide for the eye, it can be seen that the carrier concentration begins to stabilise at the highest displacement damage dose.

the previous chapter.

The ultraviolet/visible transmission geometry absorption spectra of the five irradiated samples is shown in figure 7.5. It can be seen that very little change is observed in the position of the fundamental absorption feature, attributed to direct transitions from the valence band to the conduction band near the Γ-point. It is unsurprising that little change is observed in the optical absorption spectra of these samples as figure 7.4 shows the total change in Fermi energy to be $\sim$55 meV, while the error in the measurement of the optical transition is around $\pm$ 30 meV.

The inset of figure 7.5 shows the α^2 optical absorption of the most heavily irradiated cadmium oxide sample. The energy of the direct valence band to conduction band absorption is estimated from the point of intersection of the linear fits of the fundamental absorption feature and the low energy absorption, which may be attributed to indirect transitions from the higher-lying valence band at K- and L-points. This value was determined to be 2.52 ± 0.03 eV.

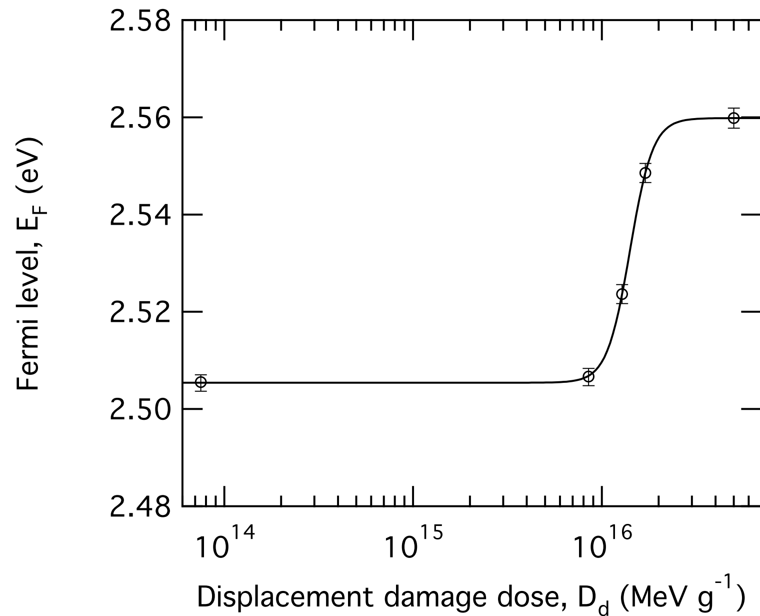

Figure 7.4: The Fermi level plotted as a function of displacement damage dose for the five cadmium oxide samples (circles). The Fermi level was calculated from carrier statistics calculations using the band parameters determined in chapter 6 and the carrier concentration from Hall effect measurements.

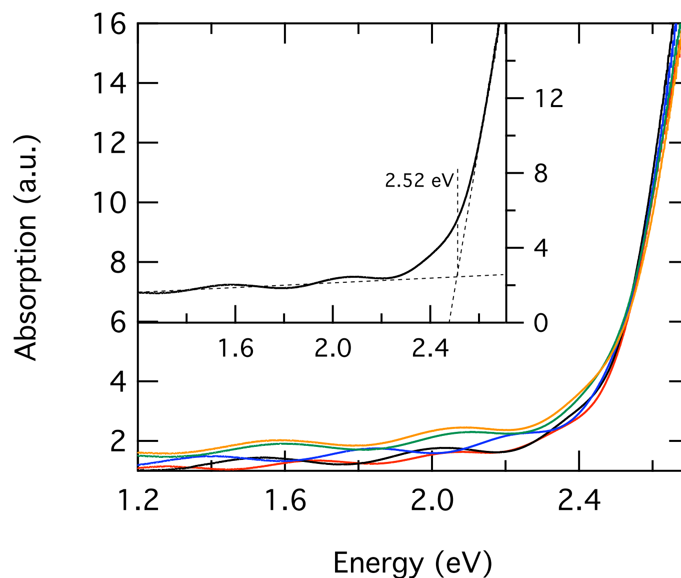

Figure 7.5: The UV/visible absorption spectra for the five cadmium oxide samples. It can be seen that there is very little change in the position of the fundamental absorption feature with increasing displacement damage dose. *Inset:* The UV/visible absorption of the most heavily irradiated sample, the position of the fundamental absorption feature has been estimated as 2.52 eV from the point of intersection of the linear extrapolations of the absorption edge and the low energy background.

Figure 7.6 shows the theoretically calculated bandstructure of rocksalt cadmium oxide between the Γ and K high symmetry points. The calculations, performed within the hybrid density functional theory framework, use a perturbative treatment of GW corrections computed with the HSE03 hybrid functional. Further details of the calculations for the production of the bandstructure can be found elsewhere [113–115]. The bandstructure in the Γ-K direction was chosen as this is where the valence band shows the most pronounced upward shift and therefore will result in the smallest direct transition from the valence band to Fermi level. From these calculations, the Fermi level in the most heavily irradiated sample is found to be 2.57 ± 0.03 eV, a value which agrees, within error, with the value determined from the carrier concentrations of the samples.

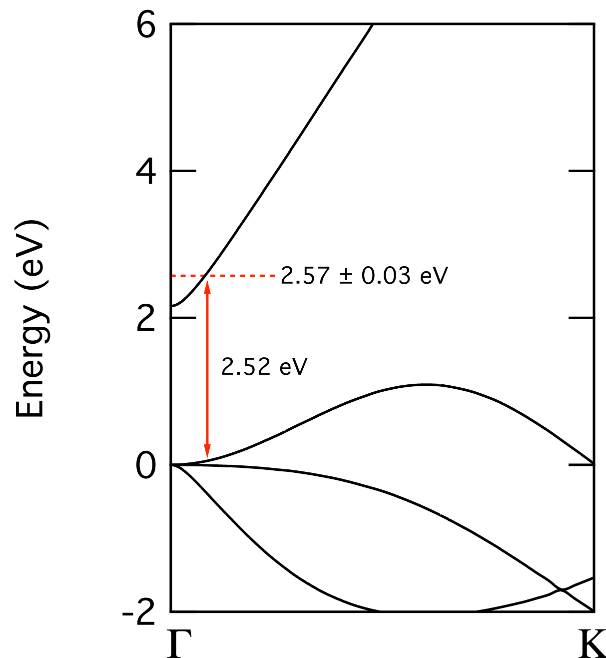

Figure 7.6: The DFT bandstructure of the conduction band and three highest valence bands of cadmium oxide between the Γ- and K-points, the direction in which the upward curvature of the valence band is greatest. The position of an optical transition of magnitude 2.52 eV is shown, suggesting a stabilised Fermi energy of 2.57 eV.

The stabilisation of the Fermi level within the conduction band of cadmium oxide as a result of He^{+} ion irradiation is not unique in semiconducting materials, this has also been observed in indium arsenide [116] and indium nitride [111].

As described in section 7.1, the irradiation of the cadmium oxide samples induces electrically active native defects, or defect complexes, within the material. The electronic nature of these defects is dependent on their position with repect to the Fermi energy. For defect levels located above the Fermi energy it is energetically favourable for the defect to be donor-like, an example of which in cadmium oxide would be an oxygen vacancy. On the other hand, if the defect level is located below the Fermi energy, it is energetically favourable for an acceptor-like defect to be formed, in the case of cadmium oxide this could be a cadmium vacancy. Therefore, by irradiating the CdO samples with high energy particles, the Fermi level is stabilised at the CNL, the average position of potential defect states.

This can also be seen from density functional theory calculations of defect formation energies. Figure 7.7 shows the formation energies of common defects in InN as a function of Fermi energy [117]. It can be seen that for Fermi energies below the CNL, donor-like nitrogen vacancies are more energetically favourable, whereas for Fermi energies above the CNL acceptor-like indium vacancies are more favourable.

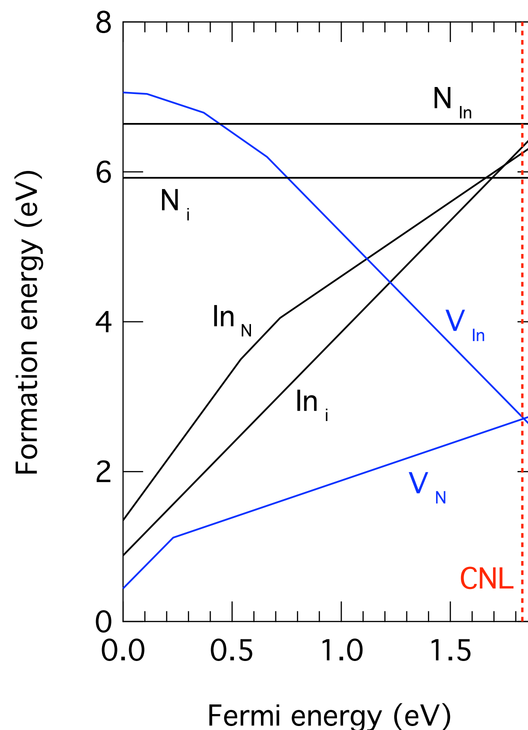

Figure 7.7: Defect formation energies of InN as a function of Fermi energy from density functional theory calculations within the local density approximation [117].

The position of the CNL is dictated by the spatially localised nature of the irradiation induced defects. As the type of defects produced by particle irradiation are typically highly localised in real space, the wavefunctions of the electronic defects produced must involve Bloch functions from several bands and over a large region of k-space [36]. Therefore, the levels will be deep (have a high ionisation energy, as either acceptors or donors) with respect to the valence and conduction bands across the entire Brillouin zone. It has been shown that, as a first approximation, the position of the CNL can be found close to the midpoint of the average bandgap across the entire Brillouin zone [118].

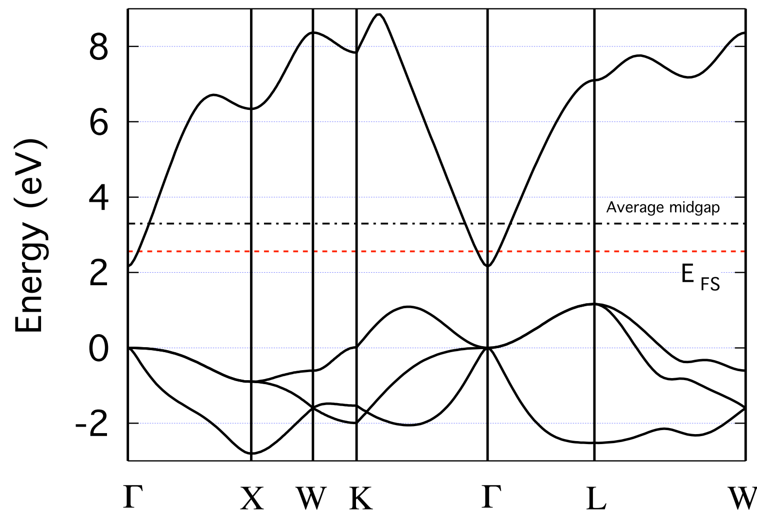

Figure 7.8: The DFT calculated bandstructure of cadmium oxide over a number of high symmetry points. The red dashed line shows the position of the CNL as determined in this work, while the black dot-dashed line shows the average midgap energy of the k-space region shown.

Figure 7.8 shows the DFT bandstructure of cadmium oxide over a greater range of high symmetry points than in figure 7.6. Here, it can be seen that the conduction band minimum at the Γ-point is significantly lower than any other point in the bandstructure. The experimentally determined value of the CNL is shown as a dashed line and is seen at 2.56 eV, 0.4 eV above the Γ-point conduction band minimum. In addition, the average bandgap across the k-space region displayed is shown as a dot-dashed line at 3.3 eV, 1.41 eV above the Γ-point conduction band minimum.

The difference between the experimentally determined value of the CNL and the average

midgap energy may be due to a number of reasons. Firstly, the figure is a two-dimensional representation of allowed energy states between a small proportion of high symmetry points in the material. In reality, the allowed energy states exist as a three-dimensional continuum of states, therefore the average midgap energy should be calculated as the midpoint of the bandgap at all positions in k-space in the entire Brillouin zone. Secondly, the DFT calculations used to determine the bandstructure are susceptible to an underestimation in energy of the shallow-core d-levels in semiconductor materials [100]. This has also been shown for CdO by x-ray photoemission spectroscopy experiments by our group. The valence band maximum to Cd $4d$ separation for the CdO samples considered in this work was found to be $\sim$9.13 eV compared to $\sim$7 eV from DFT calculations [119]. The effect of the underestimation of the Cd $4d$ levels is to overestimate the repulsion between these states and the O $2p$ (valence band) states resulting in an overestimation of the energy of the valence band states (other than at the Γ-point where this is forbidden due to symmetry considerations). The overestimation of the energy of the valence band states leads an overestimation of the average midgap energy in the region of k-space shown in figure 7.8.

7.4 Conclusions

The irradiation of single-crystalline epitaxially grown cadmium oxide has been shown to increase the sample carrier concentration with increasing irradiation dose. The position of the Fermi level was calculated from the carrier concentration determined by Hall effect and infrared reflectivity measurements, and from the calculation of the density of states of the conduction band using the material parameters determined in chapter 6. The Fermi level has been found to stabilise within the conduction band at a position 2.56 eV above the Γ-point valence band maximum. The low conduction band minimum at the Γ-point of cadmium oxide is suggested as the reason for the stabilisation of the Fermi level within the conduction band. The position of the defects energy levels introduced by the particle irradiation lie close to the centre of the bandgap across the entire Brillouin zone, due to their spatially localised nature. This average defect level is found above the Fermi level of as-grown cadmium oxide and therefore the production of donor-like defects is energetically favourable when the material is irradiated.

Conclusions and further work: Cadmium oxide

In chapter 6, the bandgap and band-edge effective mass of epitaxially grown, single crystalline CdO were determined from infrared reflectivity, Hall effect and ultraviolet/visible absorption measurements. The determination of the values was dependent on bandstructure and Fermi-Dirac statistics calculations, incorporating the effects of conduction band non-parabolicity and bandgap renormalisation. The difference between the values determined in this work (2.16 eV and 0.21 m_0) and the ubiquitous 100 K values determined and used by Koffyberg (2.28 eV and 0.14 m_0) was not insignificant.

A comparison between the mobilities of the CdO samples, obtained from Hall effect measurements and from infrared reflectance measurements, showed the dominant scattering mechanism to be due to the grain boundaries within the material. To fully exploit the inherent conductivity of CdO, therefore, it would be necessary to increase the average crystalline grain size. This may be possible by high-temperature annealing, or by further optimising the growth conditions. In either case, this will lead to a reduction in free carriers within the material, making it necessary for extrinsic doping to maintain high conductivity and transparency.

In chapter 7, the stabilisation of the Fermi level at the CNL, 0.4 eV above the Γ-point CBM, was achieved by 1 MeV $^4He^+$ ion irradiation. The location of the CNL within the conduction band of CdO explains the propensity for unintentional n-type doping of the material, as it is energetically favourable to produce defects during growth (or in this case irradiation) such that the Fermi level lies close to the CNL.

In addition, knowledge of the position of the CNL can be used to determine the surface space charge characteristics of a material, as the Fermi level is pinned close to the CNL at surfaces. When the Fermi level is above the CNL, in the bulk (i.e. far away from the surface), the band bend upwards at the surface giving rise to an electron depletion layer.

Whereas, when the Fermi level is found below the CNL, in the bulk, the bands bend down causing an electron accumulation layer, as is observed in InAs, and InN [120, 121].

Figure 7.9 shows the calculated downward bending of the conduction band of CdO, with respect to the Fermi level. The band-bending was calculated by solving Poisson's equation within a modified Thomas-Fermi approximation, for CdO with a bulk carrier concentration of 4×10^{19} cm^{-3}. By solving the Schrödinger equation of the potential well produced by the bending of the band, it is predicted that a single quantised electron energy level, shown in the figure, will be found at the surface of CdO with this carrier concentration [122, 123].

The presence of quantised states at the surface of CdO can be verified by scanning tunneling spectroscopy, or angle resolved photoemission measurements. Both of which have been used to confirm the presence of quantised electron states at the surface of In(Ga)N [124, 125].

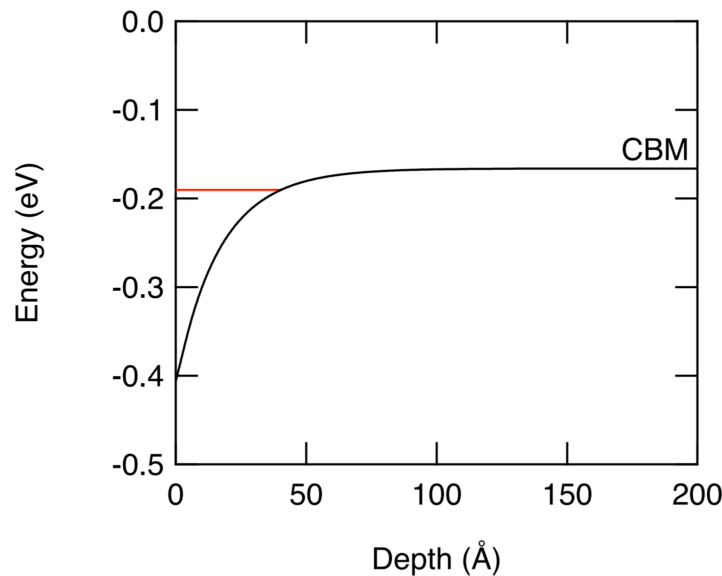

Figure 7.9: Downward band bending at the surface of cadmium oxide with a carrier concentration of 4×10^{19} cm^{-3}. The conduction band is plotted, as a function of depth, with respect to the Fermi level which is pinned at a material surface close to the charge neutrality level. The band bending was calculated by solving Poisson's equation within a modified Thomas-Fermi approximation, and the energy of the quantised subband by numerically solving the Schrödinger equation for the potential well [123].

References

[1] I. Vurgaftman, J. R. Meyer, and L. R. Ram-Mohan, J. Appl. Phys. **89**, 5815 (2001).

[2] I. Vurgaftman and J. R. Meyer, J. Appl. Phys. **94**, 3675 (2003).

[3] G. B. Stringfellow, J. Electrochem. Soc. **119**, 1780 (1972).

[4] G. B. Stringfellow and G. Hom, J. Electrochem. Soc. **124**, 1806 (1977).

[5] M. Weyers, M. Sato, and H. Ando, Jpn. J. Appl. Phys. **31**, L853 (1992).

[6] A. R. Denton and N. W. Ashcroft, Phys. Rev. A **43**, 3161 (1991).

[7] M. Kondow, K. Uomi, K. Hosomi, and T. Mozume, Jpn. J. Appl. Phys. **33**, L1056 (1994).

[8] M. Kondow, K. Uomi, A. Niwa, T. Kitatani, S. Watahiki, and Y. Yazawa, Jpn. J. Appl. Phys. **35**, 1273 (1996).

[9] M. Kondow, T. Kitatani, K. Nakahara, and T. Tanaka, Jpn. J. Appl. Phys. **38**, L1355 (1999).

[10] D. J. Friedman, J. F. Geisz, S. R. Kurtz, and J. M. Olson, J. Cryst. Growth **195**, 409 (1998).

[11] W. G. Bi and C. W. Tu, Appl. Phys. Lett. **69**, 3710 (1996).

[12] W. G. Bi and C. W. Tu, J. Appl. Phys. **80**, 1934 (1996).

[13] L. Buckle, B. R. Bennett, S. Jollands, T. D. Veal, N. R. Wilson, B. N. Murdin, C. F. McConville, and T. Ashley, J. Cryst. Growth **278**, 188 (2005).

[14] T. D. Veal, L. F. J. Piper, S. Jollands, B. R. Bennett, P. H. Jefferson, P. A. Thomas, C. F. McConville, B. N. Murdin, L. Buckle, G. W. Smith, and T. Ashley, Appl. Phys. Lett. **87**, 132101 (2005).

[15] W. Li, J. B. Héroux, and W. I. Wang, J. Appl. Phys. **94**, 4248 (2003).

[16] W. Ha, V. Gambin, M. Wistey, S. Bank, H. Yuen, S. Kim, and J. S. Harris, Electronics Letters **38**, 277 (2002).

[17] J. C. Harmand, G. Ungaro, L. Largeau, and G. L. Roux, Appl. Phys. Lett. **77**, 2482 (2000).

[18] G. Thomas, Nature **389**, 907 (1997).

[19] I. Hamberg and C. G. Granqvist, J. Appl. Phys. **60**, R123 (1986).

[20] C. G. Granqvist and A. Hultåker, Thin Solid Films **411**, 1 (2002).

[21] J. Pla, M. Tamasi, R. Rizzoli, M. Losurdo, E. Centurioni, C. Summonte, and F. Rubinelli, Thin Solid Films **425**, 185 (2003).

[22] V. Bhosle, J. T. Prater, F. Yang, D. Burk, S. R. Forrest, and J. Narayan, J. Appl. Phys. **102**, 023501 (2007).

[23] H. Kim, C. M. Gilmore, A. Pique, J. S. Horwitz, H. Mattoussi, H. Murata, Z. H. Kafafi, and D. B. Chrisey, J. Appl. Phys. **86**, 6451 (1999).

[24] A. Tsukazaki, A. Ohtomo, T. Onuma, M. Ohtani, T. Makino, M. Sumiya, K. Ohtani, S. F. Chichibu, S. Fuke, Y. Segawa, H. Ohno, H. Koinuma, and M. Kawasaki, Nature Materials **4**, 42 (2005).

[25] P. Fons, K. Iwata, S. Niki, A. Yamada, K. Matsubara, and M. Watanabe, J. Cryst. Growth **209**, 532 (2000).

[26] T. Makino, Y. Segawa, M. Kawasaki, A. Ohtomo, R. Shiroki, K. Tamura, T. Yasuda, and H. Koinuma, Appl. Phys. Lett. **78**, 1237 (2001).

[27] T. Gruber, C. Kirchner, R. Kling, F. Reuss, A. Waag, F. Bertram, D. Forster, J. Christen, and M. Schreck, Appl. Phys. Lett. **83**, 3290 (2003).

[28] N. W. Ashcroft and N. D. Mermin, *Solid State Physics*, Saunders College, 1976.

[29] M. L. Cohen and T. K. Bergstresser, Phys. Rev. **141**, 789 (1966).

[30] E. O. Kane, *Physics of III-V Compounds*, volume 1 of *Semiconductors and Semimetals*, chapter 3, Academic Press, 1966.

[31] E. O. Kane, J. Phys. Chem. Solids. **1**, 249 (1957).

[32] C. R. Pidgeon and R. N. Brown, Phys. Rev. **146**, 575 (1966).

[33] M. Henini, editor, *Dilute Nitride Semiconductors*, Elsevier, 2005.

[34] J. N. Baillargeon, P. J. Pearah, K. Y. Cheng, G. E. Hofler, and K. C. Hsieh, J. Vac. Sci. Technol. B **10**, 829 (1992).

[35] T. D. Veal, L. F. J. Piper, P. H. Jefferson, I. Mahboob, C. F. McConville, M. Merrick, T. J. C. Hosea, B. N. Murdin, and M. Hopkinson, Appl. Phys. Lett. **87**, 182114 (2005).

[36] P. Y. Yu and M. Cardona, *Fundamentals of Semiconductors*, Springer-Verlag, 2001.

[37] H. P. Hjalmarson, P. Vogl, D. J. Wolford, and J. D. Dow, Phys. Rev. Lett. **44**, 810 (1980).

[38] A. Lindsay and E. P. O'Reilly, (*Private communication*).

[39] W. Shan, W. Walukiewicz, J. W. Ager III, E. E. Haller, J. F. Geisz, D. J. Friedman, J. M. Olson, and S. R. Kurtz, Phys. Rev. Lett. **82**, 1221 (1999).

[40] E. P. O'Reilly, A. Lindsay, S. Tomić, and M. Kamal-Saadi, Semicond. Sci. Technol. **17**, 870 (2002).

[41] C. Skierbiszewski, P. Perlin, P. Wisniewski, W. Knap, T. Suski, W. Walukiewicz, W. Shan, K. M. Yu, J. W. Ager III, E. E. Haller, J. F. Geisz, and J. M. Olson, Appl. Phys. Lett. **76**, 2409 (2000).

[42] P. R. C. Kent, L. Bellaiche, and A. Zunger, Semicond. Sci. Technol. **17**, 851 (2002).

[43] L.-W. Wang, L. Bellaiche, S.-H. Wei, and A. Zunger, Phys. Rev. Lett. **80**, 4725 (1998).

[44] J. I. Pankove, *Optical Processes in Semiconductors*, Dover Publications, Inc., 1971.

[45] E. J. Johnson, *Optical properties of III-V Compounds*, volume 3 of *Semiconductors and Semimetals*, chapter 6, Academic Press, 1967.

[46] N. Kato and A. R. Lang, Acta Cryst. **12**, 787 (1959).

[47] A. Authier, *Dynamical Theory of X-Ray Diffraction*, volume 11 of *IUCr Crystallographic Symposia*, chapter 4, Oxford University Press, 2001.

[48] L. J. van der Pauw, Philips Technical Review **20**, 220 (1958).

[49] L. J. van der Pauw, Philips Res. Repts. **13**, 1 (1958).

[50] I.-h. Ho and G. B. Stringfellow, J. Cryst. Growth **178**, 1 (1997).

[51] S. R. Kurtz, J. F. Klem, A. A. Allerman, R. M. Sieg, C. H. Seager, and E. D. Jones, Appl. Phys. Lett. **80**, 1379 (2002).

[52] M. Bissiri, V. Gaspari, A. Polimeni, G. B. H. von Hogersthal, M. Capizzi, A. Frova, M. Fischer, M. Reinhardt, and A. Forchel, Appl. Phys. Lett. **79**, 2585 (2001).

[53] S. G. Spruytte, C. W. Coldren, J. S. Harris, W. Wampler, P. Krispin, K. Ploog, and M. C. Larson, J. Appl. Phys. **89**, 4401 (2001).

[54] H. B. Yuen, S. R. Bank, H. Bae, M. A. Wistey, and J. S. Harris, Appl. Phys. Lett. **88**, 221913 (2006).

[55] B. Kunert, D. Trusheim, V. Voßebürger, K. Volz, and W. Stolz, phys. stat. sol. (a) **205**, 114 (2008).

[56] A. S. Bracker, M. J. Yang, B. R. Bennett, J. C. Culbertson, and W. J. Moore, J. Cryst. Growth **220**, 384 (2000).

[57] J. Neugebauer and C. G. Van de Walle, Phys. Rev. B **51**, 10568 (1995).

[58] S. G. Spruytte, M. C. Larson, W. Wampler, C. W. Coldren, H. E. Petersen, and J. S. Harris, J. Cryst. Growth **227-228**, 506 (2001).

[59] I. A. Buyanova and W. M. Chen, editors, *Physics and applications of Dilute Nitrides*, volume 21 of *Optoelectronic properties of semiconductors and superlattices*, Taylor and Francis, 2004.

[60] T. Kitatani, M. Kondow, K. Nakahara, M. C. Larson, Y. Yazawa, M. Okai, and K. Uomi, J. Cryst. Growth **201/202**, 351 (1999).

[61] C. E. C. Wood, D. Desimone, K. Singer, and G. W. Wicks, J. Appl. Phys. **53**, 4230 (1982).

[62] H. B. Yuen, S. R. Bank, M. A. Wistey, J. S. Harris, M.-J. Seong, S. Yoon, R. Kudrawiec, and J. Misiewicz, J. Appl. Phys. **97**, 113510 (2005).

[63] H. B. Yuen, S. R. Bank, M. A. Wistey, J. S. Harris, and A. Moto, J. Appl. Phys. **96**, 6375 (2004).

[64] S. Tixier, M. Adamcyk, E. C. Young, J. H. Schmid, and T. Tiedje, J. Cryst. Growth **251**, 449 (2003).

[65] J.-C. Harmand, A. Caliman, E. V. K. Rao, L. Largeau, J. Ramos, R. Teissier, L. Travers, G. Ungaro, B. Theys, and I. F. L. Dias, Semicond. Sci. Technol. **17**, 778 (2002).

[66] P. Perlin, P. Wisniewski, C. Skierbiszewski, Y. Suski, E. Kaminska, S. G. Subramanya, E. R. Weber, D. E. Mars, and W. Walukiewicz, Appl. Phys. Lett. **76**, 1279 (2000).

[67] P. S. Dutta, H. L. Bhat, and V. Kumar, J. Appl. Phys. **81**, 5821 (1997).

[68] S. C. Jain, J. M. McGregor, and D. J. Roulston, J. Appl. Phys. **68**, 3747 (1990).

[69] J. I. Pankove, Phys. Rev. **140**, A2059 (1965).

[70] S. D. Lord, A new software tool for computing earth's atmospheric transmission of near- and far-infrared radiation, Technical report, NASA Technical Memorandum 103957, 1992.

[71] T. S. Moss, Proc. Phys. Soc. B **67**, 775 (1954).

[72] E. Burstein, Phys. Rev. **93**, 632 (1954).

[73] K. F. Berggren and B. E. Sernelius, Phys. Rev. B **24**, 1971 (1981).

[74] S. Sato, Y. Osawa, T. Saitoh, and I. Fujimura, Electronics Letters **33**, 1386 (1997).

[75] H. P. Xin and C. W. Tu, Appl. Phys. Lett. **72**, 2442 (1998).

[76] S. Sato and S. Satoh, Electronics Letters **35**, 1251 (1999).

[77] M. Sopanen, H. Xin, and C. Tu, Appl. Phys. Lett. **76**, 994 (2000).

[78] P. H. Jefferson, T. D. Veal, L. F. J. Piper, B. R. Bennett, C. F. McConville, B. N. Murdin, L. Buckle, G. W. Smith, and T. Ashley, Appl. Phys. Lett. **89**, 111921 (2006).

[79] A. Lindsay and E. P. O'Reilly, Solid State Communications **118**, 313 (2001).

[80] G. Phatak and R. Lal, Thin Solid Films **245**, 17 (1994).

[81] K. T. Ramakrishna Reddy, C. Sravani, and R. W. Miles, J. Cryst. Growth **184-185**, 1031 (1998).

[82] A. J. Varkey and A. F. Fort, Thin Solid Films **239**, 211 (1994).

[83] K. Gurumurugan, D. Mangalaraj, and S. K. Narayandass, Thin Solid Films **251**, 7 (1994).

[84] T. J. Coutts, D. L. Young, X. Li, W. P. Mulligan, and X. Wu, J. Vac. Sci. Technol. A **18**, 2646 (2000).

[85] D. Ma, Z. Ye, L. Wang, J. Huang, and B. Zhao, Mater. Lett. **58**, 128 (2004).

[86] P. Zu, Z. K. Tang, G. K. L. Wong, M. Kawasaki, A. Ohtomo, H. Koinuma, and Y. Segawa, Solid State Communications **103**, 459 (1997).

[87] A. B. M. A. Ashrafi, H. Kumano, I. Suemune, Y. W. Ok, and T. Y. Seong, Appl. Phys. Lett. **79**, 470 (2001).

[88] J. Zúñiga-Pérez, C. Munuera, C. Ocal, and V. Muñoz-Sanjosé, J. Cryst. Growth **271**, 223 (2004).

[89] J. Zúñiga-Pérez, C. Martínez-Tomás, and V. Muñoz-Sanjosé, phys. stat. sol. (c) **2**, 1233 (2005).

[90] A. B. M. A. Ashrafi, H. Kumano, I. Suemune, Y. W. Ok, and T. Y. Seong, J. Cryst. Growth **237-239**, 518 (2002).

[91] M. Yan, M. Lane, C. R. Kannewurf, and R. P. H. Chang, Appl. Phys. Lett. **78**, 2342 (2001).

[92] H. Finkenrath, Cadmium oxide (CdO), in *Physics of II-VI and I-VII Compounds, Semi-Magnetic Semiconductors*, edited by O. Madelung, M. Schulz, and H. Weiss, volume 17B of *Landolt-Börnstein: Numerical Data and Functional Relationships in Science and Technology. Group III: Crystal and Solid State Physics*, Springer, 1982.

[93] F. P. Koffyberg, Phys. Rev. B **13**, 4470 (1976).

[94] X. Li, A. Mason, T. A. Gessert, and T. J. Coutts, Electrochemical and Solid-State Letters **4**, C66 (2001).

[95] E. Menéndez-Proupin, G. Gutiérrez, E. Palmero, and J. L. Peña, Phys. Rev. B **70**, 035112 (2004).

[96] S. F. J. Cox, J. S. Lord, S. P. Cottrell, J. M. Gil, H. V. Alberto, A. Keren, D. Prabhakaran, R. Scheuermann, and A. Stoykov, J. Phys.: Condens. Matter **18**, 1061 (2006).

[97] S. Sadofev, S. Blumstengel, J. Cui, J. Puls, S. Rogaschewski, P. Schäfer, and F. Henneberger, Appl. Phys. Lett. **89**, 201907 (2006).

[98] C. Pickering, J. Phys. C: Solid St. Phys. **13**, 2959 (1980).

[99] H. Fujiwara and M. Kondo, Phys. Rev. B **71**, 075109 (2005).

[100] A. Schleife, F. Fuchs, J. Furthmüller, and F. Bechstedt, Phys. Rev. B **73**, 245212 (2006).

[101] T. Minami, H. Sato, K. Ohashi, T. Tomofuji, and S. Takata, J. Cryst. Growth **117**, 370 (1992).

[102] J. Y. W. Seto, J. Appl. Phys. **46**, 5247 (1975).

[103] J. J. Robbins, J. Harvey, J. Leaf, C. Fry, and C. A. Wolden, Thin Solid Films **473**, 35 (2005).

[104] S. Brehme, F. Fenske, W. Fuhs, E. Nebauer, M. Poschenrieder, B. Selle, and I. Sieber, Thin Solid Films **342**, 167 (1999).

[105] P. P. Edwards, A. Porch, M. O. Jones, D. V. Morgan, and R. M. Perks, Dalton Trans. **19**, 2995 (2004).

[106] T. Minami, Semicond. Sci. Technol. **20**, S35 (2005).

[107] W. Walukiewicz, Appl. Phys. Lett. **54**, 2094 (1989).

[108] W. Walukiewicz, Physica B **302-303**, 123 (2001).

[109] L. F. J. Piper, T. D. Veal, C. F. McConville, H. Lu, and W. J. Schaff, Appl. Phys. Lett. **88**, 252109 (2006).

[110] S. Messenger, E. Burke, G. Summers, M. Xapsos, R. Walters, E. Jackson, and B. Weaver, IEEE Trans. Nucl. Sci. **46**, 1595 (1999).

[111] S. X. Li, K. M. Yu, J. Wu, R. E. Jones, W. Walukiewicz, J. W. Ager III, W. Shan, E. E. Haller, H. Lu, and W. J. Schaff, Phys. Rev. B **71**, 161201(R) (2005).

[112] J. F. Ziegler, J. P. Biersack, and M. D. Ziegler, *The Stopping and Range of Ions in Matter*, volume 1, Pergamon, 1985.

[113] L. F. J. Piper, A. DeMasi, K. E. Smith, A. Schleife, F. Fuchs, F. Bechstedt, J. Zúñiga-Pérez, and V. Muñoz-Sanjosé, Phys. Rev. B **77**, 125204 (2008).

[114] J. Heyd, G. E. Scuseria, and M. Ernzerhof, J. Chem. Phys. **118**, 8207 (2003).

[115] F. Fuchs, J. Furthmuller, F. Bechstedt, M. Shishkin, and G. Kresse, Phys. Rev. B **76**, 115109 (2007).

[116] V. N. Brudnyĭ, N. G. Kolin, and A. I. Potapov, Semiconductors **37**, 408 (2003).

[117] C. Stampfl, C. G. Van de Walle, D. Vogel, P. Krüger, and J. Pollmann, Phys. Rev. B **61**, R7846 (2000).

[118] W. Mönch, J. Appl. Phys. **80**, 5076 (1996).

[119] P. D. C. King, T. D. Veal, A. Schleife, J. Zúñiga-Pérez, B. Martel, P. H. Jefferson, F. Fuchs, V. Muñoz-Sanjosé, F. Bechstedt, and C. F. McConville, Phys. Rev. B (*in press*, 2009).

[120] M. Noguchi, K. Hirakawa, and T. Ikoma, Phys. Rev. Lett. **66**, 2243 (1991).

[121] I. Mahboob, T. D. Veal, C. F. McConville, H. Lu, and W. J. Schaff, Phys. Rev. Lett. **92**, 036804 (2004).

[122] P. D. C. King, T. D. Veal, and C. F. McConville, Phys. Rev. B **77**, 125305 (2008).

[123] P. D. C. King, (*private communication*, 2008).

[124] T. D. Veal, L. F. J. Piper, M. R. Phillips, M. H. Zareie, H. Lu, W. J. Schaff, and C. F. McConville, phys. stat. sol. (a) **203**, 85 (2006).

[125] L. Colakerol, T. D. Veal, H.-K. Jeong, L. Plucinski, A. DeMasi, T. Learmonth, P.-A. Glans, S. Wang, Y. Zhang, L. F. J. Piper, P. H. Jefferson, A. Fedorov, T.-C. Chen, T. D. Moustakas, C. F. McConville, and K. E. Smith, Phys. Rev. Lett. **97**, 237601 (2006).